Master thesis and internship[BR]- Master's thesis : Implementation of a monolithic convex limiting approach for the stabilization of high speed turbulent simulations using a Discontinuous Galerkin method[BR]- Integration internship

Auteur : Reuter, Antoine
Promoteur(s) : Hillewaert, Koen
Faculté : Faculté des Sciences appliquées
Diplôme : Master en ingénieur civil en aérospatiale, à finalité spécialisée en "aerospace engineering"
Année académique : 2024-2025
URI/URL : http://hdl.handle.net/2268.2/24768

University of Liège - Faculty of Applied Sciences

Implementation of a Monolithic Convex Limiting approach for the stabilization of high speed turbulent simulations using a Discontinuous Galerkin method

---

Graduation Studies conducted for obtaining the Master's degree in
Aerospace Engineering

Supervisor:

Pr. Koen Hilleweart (Uliege)

Amaury Bilocq (Uliege)

Author:

Antoine Reuter

Jury members :
**Pr. Koen Hillaweart (Uliege), Pr. Vincent Terrapon (Uliege),
Amaury Bilocq (Uliege), David Henneaux (Cenaero), Pierre Schrooyen (VKI)**

Academic year 2024-2025

Abstract

This work presents the implementation and evaluation of a positivity-preserving hybrid method that combines the entropy-stable Discontinuous Galerkin spectral element method (ESDGSEM) with first-order finite volume (FV) schemes for simulating compressible flows. Maintaining stability in the presence of strong discontinuities and under-resolved regions is a major challenge for high-order methods like ESDGSEM. The Monolithic Convex Limiting (MCL) method has been implemented in ForDGe, providing a subcell-wise limiting technique with two variations: local bounds, which prevent the creation of new extrema, and global bounds, which avoid density and pressure crossing zero. Several existing positivity-preserving approaches, such as APriori, APosteriori, and APosteriori Subcell, have already been implemented. Each method computes a blending coefficient either element-wise or subcell-wise to describe the proportion of ESDGSEM and FV.

An analysis of the methods' performance, in terms of stability, accuracy, and computational cost, is presented across a series of benchmark test cases, including the Kelvin-Helmholtz instability, strong vortex-shock interaction, Daru-Tenaud shock tube, and three-dimensional Taylor-Green vortex. Results show that APriori and MCL provide robust and stable simulations, although with increased dissipation. In contrast, APosteriori and APosteriori Subcell better preserve fine-scale features, remaining close to the ESDGSEM solution, although occasional stability issues are observed with APosteriori. Notably, the computational cost is significantly impacted by whether the blending coefficient is computed element-wise or subcell-wise, with the subcell-wise approach resulting in the highest processing expense. Overall, the choice of method involves balancing computational efficiency, robustness, and accuracy, depending on the specific demands of the simulation.

Keywords: Compressible effects, Shock capturing methods, entropy-stable Discontinuous Galerkin spectral element method, Monolithic Convex Limiting, APriori, APosteriori, APosteriori Subcell

Acknowledgment

Contents

Chapter 1

Introduction

1.1 Context

High-speed flows are a key area of study in compressible fluid dynamics. Transonic, supersonic, and hypersonic regimes are characterised by Mach numbers near, above, and well above 1, respectively, and involve complex physical phenomena including shock waves, boundary layer interactions, turbulence, and, particularly in hypersonic flows, strong temperature gradients, real gas effects, and chemical reactions. In the transonic regime, both subsonic and supersonic regions coexist, leading to the formation of local shock waves and flow separation, which further complicate the flow structure. These phenomena are tightly coupled and non linear [55], making them difficult to model and predict. Their interactions result in highly complex flow fields, observed around engineering systems such as high-speed turbines and re-entry vehicles, where flow separation, heat transfer, and shock-boundary interactions are all interconnected.

In this context, the SPLEEN project [3, 53, 33] investigates the behaviour of next-generation high-speed low pressure turbines (LPT). These systems operate under conditions where turbulence, compressibility, and secondary flows are dominant, leading to the formation of intricate turbulent structures and the potential formation of shock waves within the blade cascades. Precise simulation of these flows is essential for improving turbine performance and ensuring mechanical integrity under extreme aerodynamic loading.

Similarly, spacecraft re-entering Earth's atmosphere are subject to an extremely harsh environment [10, 20, 48, 47, 49]. At such high speeds, the vehicle encounters aerothermodynamic phenomena, including the formation of strong shock waves and very steep temperature gradients. These effects result from the high Mach number and compression of the air in front of the vehicle. The shock-boundary interaction and thermal gradients lead to strongly coupled physics. Accurately capturing these complex flow conditions is crucial for predicting thermal protection system, surface heating, and overall vehicle stability, allowing to design re-entry vehicles.

The Discontinuous Galerkin (DG) method has emerged as a powerful numerical approach to simulate complex flows, particularly due to its high-order accuracy, geometric flexibility, and local conservation properties [11, 23, 27]. These characteristics make DG especially suitable for capturing complex and discontinuous flow features, such as those encountered in high-speed aerodynamics.

However, despite its advantages, the DG method can struggle in the presence of strong discontinuities such as shock waves, where fluid properties change abruptly and large amounts of energy concentrate in small regions. These conditions can lead to spurious oscillations or undershoots, compromising the stability and physical accuracy of the solution. This challenge is amplified in high-speed compressible flows, where phenomena such as shock waves, turbulence, and boundary layer instabilities dominate. In such regimes, traditional numerical methods often suffer from stability issues or generate non-physical results like negative pressure or density.

To address these difficulties, shock capturing methods are crucial. A particularly effective strategy is the hybridisation of DG with finite volume (FV) methods. This approach applies the accuracy of DG in smooth regions and the monotonicity and robustness of FV schemes near discontinuities [26, 32, 34, 36, 44]. By blending these two techniques, positivity preserving methods maintain high-order resolution while effectively suppressing non-physical oscillations, ensuring both numerical stability and reliable simulation of high-speed compressible flows.

1.2 Turbulence

Unlike laminar flows, where fluid moves in smooth and orderly layers, turbulent flows are chaotic, unsteady, and difficult to predict [14, 39]. This complexity arises from the non linear behaviour of the Navier-Stokes equations, as previously described. Nonlinearity rapidly amplifies small perturbations, leading to highly irregular and complex flow patterns. As a result, turbulence is characterised by random fluctuations in velocity, pressure, and vorticity.

These complex flow patterns are made up of a wide range of interacting scales. Large-scale structures, such as major eddies and coherent vortices generated by the mean flow, are responsible for the production of turbulent kinetic energy. The small-scale, also called the Kolmogorov scale, is responsible for the dissipation of the energy because of the dominant viscous effect that transforms the kinetic energy into heat. The energy transfer between the different scales is called the turbulent energy cascade.

In order to capture all the details of the turbulence, the spatial discretization of numerical simulations need to be sufficiently fine to resolve the smallest scales, down to the Kolmogorov scale. However, this requirement makes the simulations extremely costly. Different approaches have been developed to balance cost and accuracy.

Direct Numerical Simulation (DNS) provides the most detailed and accurate solution by resolving all the different turbulent scales. This level of fidelity requires an extremely fine spatial and temporal resolution, especially at high Reynolds numbers, leading to very high computational costs. As a result, DNS is typically restricted to simple geometries and low Reynolds number flows in academic research rather than practical engineering applications.

To reduce computational demands, Large-Eddy Simulation (LES) offers a compromise by explicitly resolving the large-scale turbulent structures while modelling the smaller one, sub-grid scale. This approach simplifies the problem and relaxes the resolution requirements, thus reduces computational costs compared to DNS. However, since small-scale motions are not resolved, the accuracy of LES is lower, especially near walls or in highly anisotropic turbulence.

1.3   Shock and discontinuity

Shocks are abrupt changes, also described as discontinuities, that occur in a flow field when the flow speed exceeds the local speed of sound, indicating that the Mach number is greater than one [12, 1]. These sudden changes manifest themselves as steep gradients in the flow such as pressure, density, or temperature. In the idealised case, viscous effects and heat conduction are neglected, and these discontinuities become infinitesimally thin surfaces. The Rankine-Hugoniot equations can describe the behaviour of such flows, which represent the application of the fundamental conservation law : mass, momentum, and energy across the shock.

$$\rho_1 v_1 = \rho_2 v_2 \qquad\qquad \text{mass conservation}$$

$$\rho_1 v_1^2 + p_1 = \rho_2 v_2^2 + p_2 \qquad\qquad \text{momentum conservation}$$

$$h_1 + \frac{1}{2}v_1^2 = h_2 + \frac{1}{2}v_2^2 \qquad\qquad \text{energy conservation}$$

These equations provide a framework for understanding how fluid properties change from upstream to downstream of the shock in a simplified theoretical context. However, in reality, no fluid is truly inviscid. Real flows possess viscosity and are subject to thermal diffusion, which means that the sharp transition predicted by the inviscid theory is actually spread over a finite distance. This finite thickness arises from the action of viscous forces, which are working to smooth out velocity gradients, and thermal effects, which diffuse temperature differences through conduction. As a result, the idealised discontinuity becomes a narrow but continuous region in which the flow variables undergo rapid, yet gradual, transitions. Although the shock layer is extremely thin, the rapid and significant variations in the flow properties within it require the use of the full set of compressible Navier-Stokes equations, including viscous and thermal diffusion terms, to accurately capture the physical behaviour of the flow. In addition to the internal structures, shock waves can take different forms depending on the flow configuration and the angle at which they interact with objects or flow features. A normal shock stands perpendicular to the flow direction and causes a sudden deceleration from supersonic to subsonic without deflecting the flow. In contrast, an oblique shock forms an angle with the flow, usually occurring at wedges or corners. It deflects the flow while compressing it, allowing supersonic speeds to persist downstream under certain conditions. In more complex scenarios,

particularly near surfaces, a lambda-shaped shock can develop. This structure forms when an oblique shock alone is not sufficient to decelerate the flow to subsonic conditions. As a result, a stronger normal shock develops near the wall flanked by two weaker oblique shocks that form this characteristic lambda pattern.

Another important type of discontinuity in compressible flows is contact discontinuity. This is a surface across which the temperature and density change abruptly while the velocity and pressure remain continuous. In other words, although the fluid properties on either side may differ in terms of density or temperature, there is no mass flux across the interface, and both sides remain in pressure equilibrium. Unlike shock waves, contact discontinuities do not involve entropy generation or any irreversible process. They act as passive interfaces between two fluid regions that share a normal velocity and pressure. It behaves like a sliding boundary between different fluid states moving together. They commonly appear in problems that involve mixing layers, combustion fronts, or the evolution of shock tube problems.

1.4 Discontinuous Galerkin and finite volume method

As mentioned above, DG is a variant of the Finite Element Method (FEM) who gained increasing popularity in recent years due to its high-order accuracy, geometric flexibility, and the ability to handle discontinuities in the solution [11, 23]. Making it particularly suited for capturing non linear flow regimes. Thanks to it's compatibility with high-order polynomial approximations, DGM gives an accurate result with a rather coarse mesh, leading to a fast and more efficient convergence.

However, DG can still have trouble overcoming strong gradients, regions where energy accumulates due to the presence of shocks. To address this, the robustness of the method has been further enhanced through the use of entropy variables in the construction of entropy-stable fluxes, ensuring consistency with the second law of thermodynamics. This has led to the development of the entropy stable Discontinuous Galerkin Spectral Element Method (ESDGSEM) [4, 6, 15, 24, 30]. These developments improve the control of the energy transfer within the solution, enhancing the stability of the simulation.

Despite these improvements, negative pressure and density can still arise near these discontinuities due to spurious oscillations, which compromise the stability of the simulation. To address this, a hybrid approach that combines DG with finite volume (FV) methods is often used, [18, 31, 32, 43, 44]. FV schemes enforce monotonicity and enhance robustness by damping unphysical oscillations, thanks to their conservation properties and shock-capturing capabilities. Although FV lacks high order accuracy, its should be used as less as possible, preserving the accuracy of DG in smooth regions while ensuring stability in regions of sharp gradients.

1.5 Outline and contributions

The purpose of the work is to implement a positivity-preserving method known as Monolithic Convex Limiting (MCL) [18, 31, 44]. MCL is a subcell-wise limiting technique that performs stabilisation based only on the currently known solution, in contrast to other methods that require a precomputed next-time step solution. This feature makes it compatible with explicit solvers, which are widely used in industrial applications due to their simplicity and computational efficiency. Its subcell manner allows for a specific application of the blending coefficient.

The chapter 2 describes the numerical aspects of DG and ESDGSEM, which solve the compressible Navier-Stokes equations. Several positivity-preserving techniques that combine ESDGSEM with FV, who have already been implemented, such as APriori, APosteriori, and APosteriori Subcell limiting methods, are also described in this chapter. These approaches demonstrate accurate results while maintaining the stability of simulations involving shocks and turbulence characteristics. In this context, MCL is implemented to compare its subcell-wise limiting process with the other existing approaches. The different steps to compute the blending coefficient are provided following the other methods.

The introduction of limiting techniques can affect the balance between numerical and physical dissipation. Excessive limiting can suppress important small-scale features, while insufficient limiting can result in numerical instabilities. This is especially critical in under-resolved turbulent regimes, where the interplay between numerical and viscous dissipation is significant. A comprehensive comparison of the different limiting strategies is presented in chapter 3, including both qualitative and quantitative analyses across a variety of test cases. The performance of each method is evaluated in terms of accuracy, stability, and physical consistency, particularly in the presence of compressible effects. The assessment covers a range of benchmark; the Kelvin-Helmholtz instability, the strong vortex-shock interaction, the Daru-Tenaud shock tube, and the Taylor-Green vortex, involving complex interactions among turbulence, shocks, and boundary layers.

To conclude, chapter 4 provides a summary of the main findings and contributions of this work. Highlights the effectiveness of the different limiting strategies in capturing complex flow phenomena, such as shocks and turbulence, while maintaining numerical stability and physical accuracy. Additionally, the chapter discusses the limitations encountered during the study and proposes several future perspectives to further improve the simulation of high-speed compressible flows. These perspectives include the development of more advanced limiting techniques, the integration of adaptive mesh refinement to better resolve critical regions, and the extension of the current methods to more complex geometries and multi-physics problems. The chapter concludes by outlining potential research directions that could enhance the robustness and predictive capabilities of numerical solvers for challenging flow regimes.

1.6 ForDGe

ForDGe is a Cartesian-immersed DGM solver for complex geometry, currently in development at the University of Liege. It uses a high-order DGM that allows one to accurately capture the turbulent features. One of the aims of ForDGe is to *"enable highly accurate scale-resolving simulations (DNS, LES) of shock-dominated transonic turbulent flows by reducing the interaction of the shock capturing strategy with the turbulent flow features"*[35]. All simulations performed in this report have been processed using ForDGe.

1.7 Utilisation of IA

With regard to the use of artificial intelligence (AI), its application in this work has been limited to improving the clarity and readability of the written content. AI tools were only used to assist in editing and refining the text and were not involved in the development, implementation, or analysis of the numerical methods or simulations.

Chapter 2

Numerical Methods

2.1 Compressible Navier-Stokes equation

Accurate resolution of flow discontinuities, including shocks and turbulent structures, requires solving the fundamental equations governing fluid motion. For viscous and compressible fluids, these are the Navier-Stokes equations, which describe the evolution of mass, momentum, and energy. In their conservative form, the equations can be written as follows.

$$\frac{\partial}{\partial t} \underbrace{\begin{pmatrix} \rho \\ \rho\mathbf{v} \\ \rho E \end{pmatrix}}_{\substack{\text{Conservative} \\ \text{variables}}} + \nabla \cdot \underbrace{\begin{pmatrix} \rho\mathbf{v} \\ \rho\mathbf{v} \cdot \mathbf{v} + p\mathbf{I} \\ \rho\mathbf{v} \cdot H \end{pmatrix}}_{\substack{\text{Convective} \\ \text{flux}}} = \nabla \cdot \underbrace{\begin{pmatrix} 0 \\ \boldsymbol{\sigma} \\ \boldsymbol{\sigma} \cdot \mathbf{v} + \mathbf{Q} \end{pmatrix}}_{\substack{\text{Diffusive} \\ \text{flux}}} \tag{2.1}$$

Conservative variables include density ρ, momentum vector $\rho\mathbf{v}$, and total energy ρE. The velocity vector is denoted by $\mathbf{v}$ and E represents the specific total energy, which contains both internal and kinetic components.

Convective fluxes describe the advection of conservative variables, governed by the fluid velocity field. These fluxes incorporate the total enthalpy H, defined as:

$$H = h + k = e + \frac{p}{\rho} + \frac{1}{2}\mathbf{v} \cdot \mathbf{v} \tag{2.2}$$

where e is the internal energy and $h = e + \frac{p}{\rho}$ is the specific enthalpy. The pressure p is related to the internal energy and temperature through the ideal gas law.

$$p = (\gamma - 1)\rho e = (\gamma - 1)\left(\rho E - \rho\frac{\|\mathbf{v}\|^2}{2}\right) = \rho R T \tag{2.3}$$

Both internal energy and enthalpy can be expressed in terms of temperature. The internal energy is related to the temperature by $e = c_v T$, and the enthalpy is given by $h = c_v T + \frac{p}{\rho} = c_p T$, where c_v and c_p are the specific heat capacities at constant volume and pressure, respectively. The ratio $\gamma = c_p/c_v$ is the specific heat ratio, and R is the ideal gas constant.

In addition to convective transport, the Navier-Stokes equations account for diffusive fluxes, which arise from microscopic effects such as viscosity and thermal conduction. These terms tend to smooth variations in the flow field and drive the system toward thermodynamic equilibrium. The diffusive momentum flux is represented by the shear stress tensor $\boldsymbol{\sigma}$, given by

$$\boldsymbol{\sigma} = \mu\left(\nabla\mathbf{v} + \nabla\mathbf{v}^T - \frac{2}{3}(\nabla \cdot \mathbf{v})\mathbf{I}\right) \tag{2.4}$$

where μ is the dynamic viscosity and the term $\nabla\mathbf{v}+\nabla\mathbf{v}^T$ corresponds to the strain rate tensor. The divergence of the velocity field, $\nabla\cdot\mathbf{v}$, is linked to compressibility. When the divergence of the velocity field is zero, the flow is considered incompressible. However, in the current context, compressible flows are the field of interest, which implies $\nabla\cdot\mathbf{v}\neq 0$.

The energy diffusive flux includes the heat flux vector $\mathbf{Q}$, which is modelled by Fourier's law as

$$\mathbf{Q}=-\kappa\nabla T \tag{2.5}$$

with κ denoting the thermal conductivity and ∇T the temperature gradient.

In some of the numerical test cases discussed in chapter 3, the fluid is assumed to be inviscid and adiabatic. In this limit, viscous and thermal diffusion effects are neglected by setting $\boldsymbol{\sigma}=0$ and $\mathbf{Q}=0$. The resulting system reduces to the compressible Euler equations, expressed as

$$\frac{\partial}{\partial t}\begin{pmatrix}\rho\\\rho\mathbf{v}\\\rho E\end{pmatrix}+\nabla\cdot\begin{pmatrix}\rho\mathbf{v}\\\rho\mathbf{v}\cdot\mathbf{v}+p\mathbf{I}\\\rho\mathbf{v}\cdot H\end{pmatrix}=0 \tag{2.6}$$

2.2 Measured quantities

After solving the governing equations, and obtaining the evolutions of conservative variables all over the domain. From the computed fields, various quantities can be extracted, such as kinetic energy, viscous dissipation, pressure work, etc., taking the integrals over the entire domain. These integral quantities allow a quantitative comparison with results obtained from other numerical methods. Moreover, qualitative comparisons can be made using numerical Schlieren techniques, which enhance the visibility of fine-scale features and gradients, allowing for a clearer assessment of flow structures and discontinuities.

2.2.1 Kinetic energy

The kinetic energy, $k=\frac{1}{2}\mathbf{v}\cdot\mathbf{v}$, is one of the main quantities that should be correctly captured during simulations. To obtain the equation that describes its evolution, as detailed in [39], the dot product of the momentum conservation equation and the velocity $\mathbf{v}$ give the following equation

$$\frac{\partial\rho k}{\partial t}=\underbrace{p\nabla\cdot\mathbf{v}}_{\substack{\text{Pressure}\\\text{work}}}-\underbrace{\boldsymbol{\sigma}:\nabla\mathbf{v}}_{\substack{\text{Viscous}\\\text{dissipation}}}+\underbrace{\nabla\cdot(\rho k\mathbf{v}-p\mathbf{v}+\boldsymbol{\sigma}\cdot\mathbf{v})}_{\substack{\text{Transport}\\\text{terms}}} \tag{2.7}$$

The pressure work, $p\nabla\cdot\mathbf{v}$, describes the energy exchange resulting from pressure forces acting on fluid elements, capturing how pressure gradients contribute to the acceleration or deceleration of the flow.

The viscous dissipation, $-\boldsymbol{\sigma} : \nabla\mathbf{v}$, quantifies the irreversible conversion of kinetic energy into internal energy, acting as a sink of kinetic energy. By injecting Eq. 2.4 into viscous dissipation, as made by Sarkar [46], one can divide it into two quantities

$$\boldsymbol{\sigma} : \nabla\mathbf{v} = \underbrace{\mu(\omega \cdot \omega)}_{\substack{\text{Solenoidal} \\ \text{dissipation}}} + \underbrace{\frac{4}{3}\mu(\nabla \cdot \mathbf{v})^2}_{\substack{\text{Dilatationial} \\ \text{dissipation}}} \tag{2.8}$$

where $\omega = \nabla \times \mathbf{v}$ is the vorticity. The first term, denoted solenoidal dissipation, ϵ_S, characterises the rate at which kinetic energy is dissipated by small-scale rotational motions or vortical structures. This component is dominant in incompressible flows and is related to enstrophy, $\xi = \frac{1}{2}\omega \cdot \omega$ who measures the intensity of rotational motion. The second component corresponds to the dilatational dissipation, ϵ_D, which is related to the compressibility of the flow, represented by the divergence of velocity, $\nabla \cdot \mathbf{v}$. Measures the kinetic energy lost as a result of expansion and compression of the flow. These expansion and compression effects are especially pronounced in high-speed flows involving shock waves, where compressibility plays a dominant role.

Finally, the transport terms, $\nabla \cdot (\rho k\mathbf{v} - p\mathbf{v} + \boldsymbol{\sigma} \cdot \mathbf{v})$, account for the redistribution of kinetic energy through the domain without contributing to the production or dissipation. These terms represent energy fluxes through advection, pressure work, or viscous stresses. If taking the integral form of the kinetic energy equation is taken over the entire domains, the transport terms vanish in the case of periodic boundary conditions. The periodicity ensures that the flux entering one side of the domain is perfectly balanced by the flux exiting the opposite side. As a result, the net contribution becomes zero. This setup is used in multiple test cases presented in the following, usually used to simulate repeating flows without adding artificial boundaries. Using the integral form over a domain with periodic boundary conditions, the kinetic energy can be rewritten as

$$\frac{\partial}{\partial t}\int_\Omega \rho k \; dV = \int_\Omega p\nabla \cdot \mathbf{v} \; dV - \int_\Omega 2\mu\xi \; dV - \int_\Omega \frac{4}{3}\mu(\nabla \cdot \mathbf{v})^2 \; dV \tag{2.9}$$

2.2.2 Numerical Schlieren

The Schlieren is an optical visualisation method that is used to highlight fine details and small variations of density in a flow field. It is particularly effective in revealing sharp gradients, such as shock waves or other discontinuities. This method provides a qualitative view of flow structures by accentuating regions with strong density gradients. In order to reproduce this effect in numerical simulations, a numerical Schlieren (Sch), defined by Quirk and Karni [40], can be constructed using the following formula

$$Sch = \frac{\ln(1 + \|\nabla\rho\|)}{\ln(10)} \tag{2.10}$$

2.3 Discontinuous Galerkin for compressible flows

The Discontinuous Galerkin (DG) method is a class of the Finite Element Method that combines features of both finite volume and finite element, making it particularly well-suited for solving hyperbolic conservation laws, such as the Euler and Navier-Stokes equations. Unlike classical finite element methods, which enforce continuity of the solution across element boundaries, DG allows the solution to be discontinuous between elements. This property gives DG great flexibility in handling complex geometries, adaptivity, and hp-refinement, while maintaining high-order accuracy.

The computational domain Ω is divided into a mesh of non-overlapping elements K, with $\Omega = \bigcup K$. Within each element, the solution is approximated by a polynomial expansion defined on a reference element $\hat{K}$, typically chosen as a tensor-product domain such as the unit square or cube for quadrilateral and hexahedral meshes, respectively. The polynomial approximation space $\mathcal{Q}^o(\hat{K})$ consists of all polynomials with a maximum degree o in each spatial coordinate direction

$$\mathcal{Q}^o(\hat{K}) = \left\{ \xi_1^{i_1} \dots \xi_d^{i_d}, \ \xi \in \hat{K}, \ 0 \leq i_k \leq o, \ k = 1, \dots, d \right\} \tag{2.11}$$

This tensor-product structure enables efficient numerical quadrature and the construction of hierarchical basis functions [27].

To impose boundary and interface conditions in DG, the notion of trace spaces is essential. The trace space $\mathcal{V}^o(\hat{K})$ on each reference element face $\hat{f}$ is defined as the restriction of the volume polynomial space $\mathcal{V}^o(\hat{K})$ to the face $\hat{f} \subset \partial\hat{K}$

$$\mathcal{V}^o(\hat{f}) = \left\{ u|_{\hat{f}}, \ u \in \mathcal{V}^o(\hat{K}), \ \hat{f} \in \partial\hat{K} \right\} \tag{2.12}$$

These trace spaces facilitate the definition of numerical fluxes at element interfaces, which resolve discontinuities in the solution, and enforce weak continuity conditions.

Within each element, the approximation of the solution $\mathbf{u}^h(\mathbf{x}, t)$ is expanded in terms of a finite set of shape functions $\phi_i(\mathbf{x})_{i=1}^{N_o}$ spanning the polynomial space $\mathcal{V}^o(\hat{K})$, where N_o is the number of basis functions determined by the degree of polynomial and the spatial dimension

$$\mathbf{u}^h(x, t) = \sum_{i=1}^{N_o} \phi_i(x)\mathbf{u}_i(t) \tag{2.13}$$

Here, $\mathbf{u}_i(t)$ are the time-dependent degrees of freedom corresponding to the solution coefficients in each element.

One of the defining features of DG methods is their handling of element interfaces. Unlike standard continuous Galerkin FEM, which enforces continuity strongly by matching degrees of freedom at shared nodes, DG methods treat interfaces weakly by introducing numerical flux functions. These fluxes approximate the physical flux and incorporate information from both

sides of the interface, allowing for stable and consistent communication across discontinuities. This feature aligns DG closely with finite volume methods, but retains the high-order accuracy and geometric flexibility characteristic of spectral or high-order finite element methods.
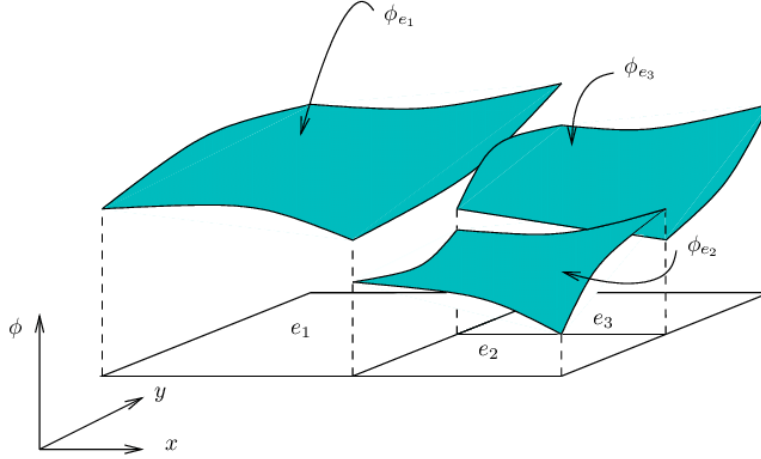
Figure 2.1: Non-conforming discontinuous finite element interpolation.
The illustration is taken from [23]

The weak form of the governing equations, such as the compressible Navier-Stokes equations Eq. 2.1, is obtained by summing the contribution of all integrations over each element K

$$\sum_K \int_K v \frac{\partial \mathbf{u}^h}{\partial t} \, dV + \sum_K \int_K v \left(\nabla \cdot F^c(\mathbf{u}^h) \right) \, dV = \sum_K \int_K v \left(\nabla \cdot F^d(\mathbf{u}^h, \nabla \mathbf{u}^h) \right) \, dV \qquad (2.14)$$

where F^c and F^d denote the convective and diffusive fluxes, respectively.

Applying integration by parts to the convective terms and summing over all the faces contributions interpreted as the boundary integrals gives the following result

$$\sum_K \int_K v \left(\nabla \cdot F^c(\mathbf{u}^h) \right) dV = -\sum_K \int_K \nabla v \cdot F^c(\mathbf{u}^h) \, dV + \sum_f \int_f [v] \, f^*(\mathbf{u}^{h+}, \mathbf{u}^{h-}, n) \, dS \qquad (2.15)$$

where $[v] = v^+ - v^-$ is the jump operator of v across the face f, associated with $n^+ = n$ and $n^- = -n$, and f^* corresponds to the numerical flux.

For diffusive fluxes, the Incomplete Interior Penalty Method (IIPM) is used, [22], which leads to the following decomposition

$$\begin{aligned}
\sum_K \int_K v \left(\nabla \cdot F^d(\mathbf{u}^h, \nabla \mathbf{u}^h) \right) dV = \sum_K \int_K \nabla v \cdot F^d(\mathbf{u}^h, \nabla \mathbf{u}^h) \, dV \\
- \sum_f \int_f [v] \left\{ F^d(\mathbf{u}^h, \nabla \mathbf{u}^h) \right\} dS \\
+ \sum_f \sigma_f \int_f [v][\mathbf{u}^h] \, dS
\end{aligned} \qquad (2.16)$$

where the average operator is defined as $\{a\} = \frac{a^+ + a^-}{2}$. The penalty parameter σ_f is selected to ensure the coercivity of the bilinear form and is computed using

$$\sigma_f > \max \left(n_f \rho_D (o+1)^2 \frac{A(f)}{8V(K)} \right) \tag{2.17}$$

with n_f being the number of faces of element K, $\rho_D = 2\mu + \frac{\kappa}{c_v}$ is the diffusive spectral radius, $A(f)$ the face area, and $V(K)$ the volume of the element.

The integration of each element is performed using quadrature points, which are distinguished into volume and surface quadrature points. Each of these points can be mapped to the reference coordinates on the reference element using interpolation matrices

$$(\mathbf{V}_v)_{ij} = \phi_i(\xi_v) \qquad\qquad (\mathbf{V}_f)_{ij} = \phi_i(\xi_f) \tag{2.18}$$

where ξ_v and ξ_f denote the volume and surface reference coordinates, respectively. The mapping between the physical element and the reference one is characterised by the Jacobian, defined as

$$J = \frac{\partial \mathbf{x}}{\partial \xi} \tag{2.19}$$

The mass matrix is defined as the inner product of shape functions over the reference element.

$$\mathbf{M} = \int_{\hat{K}} \phi_i(\xi)\phi_j(\xi)\, d\xi \tag{2.20}$$

The weight matrix is a diagonal matrix containing the quadrature weights. It is defined separately for volume and surface quadrature

$$\mathbf{W} = \mathrm{diag}(w_0, \ldots, w_o) \tag{2.21}$$

The differentiation matrix with respect to the k-th coordinate maps the coefficients of an interpolated function to the coefficients of its derivative

$$\mathbf{D}^k = \frac{\partial \phi_i}{\partial \xi_k} \tag{2.22}$$

The boundary integration matrix on a face in the k-th direction is defined as

$$\mathbf{B}^k = \mathbf{W}_f \, \mathrm{diag}(\mathbf{n}_k) \tag{2.23}$$

here, $\mathbf{n}_k = \{n_1 J_f, \ldots, n_d J_f\}$ is the scaled normal vector outward on the element $\hat{K}$ where J_f is the determinant of the Jacobian corresponding to the mapping from a face of $\partial \hat{K}$ to a reference face.

Recombining Eq. 2.15 and Eq. 2.16 into Eq. 2.14 and using the matrices notation just described, the following formulation is found

$$
\mathbf{M}\frac{\partial \mathbf{u}^h}{\partial t} - \sum_{k=1}^{d} \mathbf{W}_v(\mathbf{D}^k)^T \left(F^c(\mathbf{u}^h) + F^d(\mathbf{u}^h, \nabla \mathbf{u}^h) \right)
$$
$$
+ \sum_{k=1}^{d} \mathbf{V}_f^T \mathbf{B}^k \left(f^*(\mathbf{u}^{h+}, \mathbf{u}^{h-}, n) + \left\{ F^d(\mathbf{u}^h, \nabla \mathbf{u}^h) \right\} - \sigma_f[\mathbf{u}^h] \right) = 0 \qquad (2.24)
$$

Entropy stable Discontinuous Galerkin Spectral Element Method

As described in Sec. 1.4, the entropy stable discontinuous Galerkin spectral element method (ESDGSEM) is a variant of the discontinuous Galerkin method that enhances the stability of the discontinuous Galerkin spectral element method, described by Kopriva [29], through the utilisation of entropy variables and entropy-stable fluxes, which enforces the second law of thermodynamics.

The entropy variables [5, 7, 52, 19] are a set of thermodynamically motivated variables used to reformulate the Navier-Stokes equations, enforcing the second law of thermodynamics. These variables, $\mathbf{w}(\mathbf{u})$, are obtained by taking the gradient of the mathematical entropy function relative to the conservative variables

$$
\mathbf{w}(\mathbf{u}) = \frac{\partial U}{\partial \mathbf{u}} \qquad (2.25)
$$

where $U(\mathbf{u})$ is a convex entropy function. This convexity ensures that the mapping between conservative variables $\mathbf{u}$ and entropy variables $\mathbf{w}$ is one-to-one, with a symmetric positive-definite Jacobian [19, 52]

$$
\mathbf{H}(\mathbf{u}) = \frac{\partial \mathbf{w}}{\partial \mathbf{u}} \qquad (2.26)
$$

For the compressible Navier-Stokes equations with non-zero heat flux, as described by Hughes [25], the only physically consistent entropy function, up to a constant multiple, is given by

$$
U(\mathbf{u}) = -\rho s \qquad (2.27)
$$

the physical entropy is denoted by $s = \log\left(\frac{p/p_{ref}}{(\rho/\rho_{ref})^\gamma}\right)$.

Hughes [25] reformulate the diffusive fluxes in terms of entropy variables to ensure the second law of thermodynamics. Following Hughes, the diffusive fluxes can be expressed as

$$
F^d(\mathbf{u}, \nabla \mathbf{u}) = \mathbf{K}(\mathbf{u})\nabla \mathbf{w} \qquad (2.28)
$$

where $\mathbf{K}(\mathbf{u})$ is a semidefinite positive symmetric matrix. This symmetrising property is crucial, it linearises the viscous terms in $\nabla \mathbf{w}$, making the entropy production rate

$$
(\nabla \mathbf{w})^T \mathbf{K}(\mathbf{u})\nabla \mathbf{w} \geq 0 \qquad (2.29)
$$

ensuring compatibility with the second law of thermodynamics.

Furthermore, by contracting the Navier-Stokes equations with $\mathbf{w}^T$, the convective fluxes can be expressed as

$$\mathbf{w}^T \nabla \cdot F^c(\mathbf{u}) = \nabla \cdot F^S(\mathbf{u}) \tag{2.30}$$

where $F^S(\mathbf{u})$ is the entropy flux. The Navier-Stokes equations can then be rewritten as

$$\frac{\partial}{\partial t}U + \nabla \cdot (F^S - \mathbf{w}^T \mathbf{K} \nabla \mathbf{w}) = -(\nabla \mathbf{w})^T \mathbf{K}(\mathbf{u}) \nabla \mathbf{w} \leq 0 \tag{2.31}$$

This formulation corresponds to the local entropy inequality. Using periodic boundary conditions, the global entropy inequality can be obtained by integrating over the entire domain

$$\frac{\mathrm{d}}{\mathrm{d}t} \int_\Omega U(\mathbf{u}) \mathrm{d}V \leq 0, \tag{2.32}$$

ensuring that the mathematical entropy cannot increase in time, bounding the energy of the system.

The projection of conservative variables to entropy variables is defined as

$$\mathbf{w}(\mathbf{u}) = \begin{pmatrix} \omega_1 \\ \omega_{1+i} \\ \omega_{d+2} \end{pmatrix} = \begin{pmatrix} \frac{\rho e(\gamma+1-s)-\rho E}{\rho e} \\ \frac{\rho v_i}{\rho e} \\ -\frac{\rho}{\rho E} \end{pmatrix} \tag{2.33}$$

Conversely, conservative variables can be recovered from the entropy variables as follows

$$\mathbf{u}(\mathbf{w}) = \begin{pmatrix} \rho \\ \rho v_i \\ \rho E \end{pmatrix} = \begin{pmatrix} -\rho e \omega_{d+2} \\ \rho e \omega_{1+i} \\ \rho e \left(1 - \frac{\sum \omega_{1+j}^2}{2\omega_{d+2}}\right) \end{pmatrix} \tag{2.34}$$

Furthermore, ESDGSEM uses the Gauss-Lobatto Legendre (GLL) quadrature interpolation points. Using this quadrature rule, illustrated in Fig. 2.2, the interpolation and quadrature points coincide and include both end points of the interval. This alignment significantly simplifies the structure of several matrices previously defined, the interpolation matrix becomes identity matrix, and as a result, the mass matrix equals the weight matrix, $\mathbf{M} = \mathbf{W}$.

At element interfaces, the inviscid flux is replaced by an entropy-conserving two-point flux such as the Chandrashekar flux [8], which exactly preserves the discrete entropy conservation property between neighbouring states. For stability, entropy dissipation is added by blending this flux with a matrix dissipation term based on the jump in entropy variables and eigenvalues of the flux Jacobian, ensuring entropy stability.

Lastly, the differentiation matrix satisfies the summation-by-parts (SBP) properties, [41], which are crucial to ensure stability and conservation in high-order numerical schemes. The

SBP property mimics integration by parts at the discrete level, allowing boundary contributions to be handled correctly and preventing the growth of non-physical oscillations.
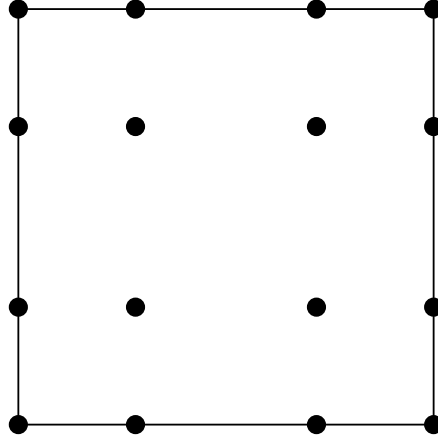

Figure 2.2: Gauss-Lobatto quadrature points for 3rd order polynomial.

The generalised SBP operator, defined as $\mathbf{Q}^k = \mathbf{W}\mathbf{D}^k$, [6], combines the weight matrix $\mathbf{W}$ and the differentiation matrix $\mathbf{D}^k$ for the k-th coordinate direction. This operator is essential for constructing flux differencing formulations, which are used to discretise non linear fluxes in a way that preserves entropy stability and mimics the continuous entropy inequality. The flux differencing approach replaces the standard derivative of fluxes with a difference of two-point numerical fluxes, ensuring that the discrete scheme inherits the entropy stability properties of the continuous equations.

By incorporating these simplifications into Eq. 2.24, the ESDGSEM formulation is

$$\mathbf{M}\frac{\partial \mathbf{u}^h}{\partial t} + \sum_{k=1}^{d}\left(\left(\mathbf{Q}^k - (\mathbf{Q}^k)^T\right)\circ \mathbf{F}_S^k\right) - \sum_{k=1}^{d}\mathbf{W}_v(\mathbf{D}^k)^T\left(F^d(\mathbf{u}^h, \nabla\mathbf{u}^h)\right)$$
$$+ \sum_{k=1}^{d}\mathbf{B}^k\left(f_S^*(\mathbf{u}^{h+}, \mathbf{u}^{h-}, n) + \left\{F^d(\mathbf{u}^h, \nabla\mathbf{u}^h)\right\} - \sigma_f[\mathbf{u}^h]\right) = 0 \quad (2.35)$$
$$(\mathbf{F}_S^k)_{ij} = \mathbf{f}_S^k(\mathbf{u}_i^h, \mathbf{u}_j^h)$$

where $A \circ B$ corresponds to the Hadamard product.

However, the ESDGSEM formulation is not sufficient to ensure the stability of the solution in all cases, as previously mentioned. In contrast, the Finite Volume Method (FVM) is a robust method that can handle discontinuities and shocks, making it suitable for compressible flows.

2.4 Finite volume

The Finite Volume Method discretises the computational domain into a finite number of control volumes (cells), over which the integral form of the conservation laws is enforced. For each

control volume, the change in the conserved quantity is balanced by the net flux through its boundaries. This approach ensures local and global conservation properties, making FVM especially suitable for solving hyperbolic conservation laws and handling discontinuities such as shocks.

By discretising the convective form of the compressible Navier-Stokes equations Eq. 2.1 using the finite volume method, one can find the following equation

$$V_K \frac{\partial \overline{\mathbf{u}^h}}{\partial t} = - \sum_{f \in \partial K} \int_f f^*(\mathbf{u}^{h+}, \mathbf{u}^{h-}, n) \, dS \tag{2.36}$$

where $\overline{\mathbf{u}^h}$ is the average cell value of the solution, V_K is the volume of the cell K, and f^* is the numerical flux function. The numerical flux can be chosen as the Chandrashekar flux.

FVM is robust and maintains monotonicity, making it effective for capturing shocks and discontinuities. However, standard FVM schemes are typically low-order, which leads to less accurate results.

Hennemann demonstrates [21], that a low-order FV scheme can be obtained by taking the GLL quadrature points as the mean values of the subcells. Therefore, a hybrid scheme can be constructed with the GLL quadrature points as subcell averages within each element, allowing the construction of a first-order finite volume scheme integrated in the discontinuous Galerkin framework. This approach enables a combination between high-order DG accuracy and the robustness of FV in regions that require enhanced stability.

Fig. 2.3 illustrates the GLL quadrature points used in the finite volume method, which are also employed in the discontinuous Galerkin method. The dashed line represents the interface of FVM, where the numerical flux is computed. The points are the quadrature points used as the average cell value in the finite volume method and as the interpolation points in the entropy stable discontinuous Galerkin spectral elemets methods, see Sec. 2.3.
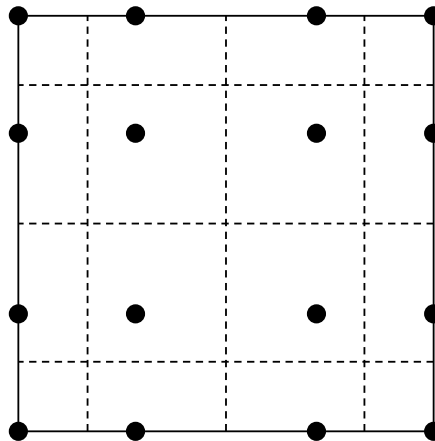

Figure 2.3: 3rd interpolation order elements with GLL quadrature points. The dashed line represent the interface of FV.

2.5 Positivity preserving

The positivity preserving method consists of using a combination of ESDGSEM and FVM to ensure the stability of the solution and avoid computing negative pressure and density. The temporal evolution, detonated by $\dot{u} = \frac{\partial u}{\partial t}$, is given by

$$\dot{\mathbf{u}}_i = (1 - \alpha)\dot{\mathbf{u}}_i^{\text{DG}} + \alpha\dot{\mathbf{u}}_i^{\text{FV}} \tag{2.37}$$

the index i corresponds to the interpolation points i within the element.

A blending factor, α, is calculated that indicates the proportion of ESDGSEM, with the notation DG, or FV that is used to compute the next solution. $\alpha \in [0, 1]$ where $\alpha = 0$ means complete DG and $\alpha = 1$ yields a fully FV-based solution.

Let rewrite the evolution of the solution for DG, and FV for simplicity

$$m_i\dot{\mathbf{u}}_i^{\text{DG}} = \mathbf{r}_i^{\text{DG}} \qquad\qquad m_i\dot{\mathbf{u}}_i^{\text{FV}} = \mathbf{r}_i^{\text{FV}} \tag{2.38}$$

where $\mathbf{r}_i^{\text{DG}}$ and $\mathbf{r}_i^{\text{FV}}$ correspond to residues of high order and low order, respectively.

To compute the next iteration, ForDGe computes a correcting residue to limit the high-order residual with the following equation

$$m_i\dot{\mathbf{u}}_i = \mathbf{r}_i^{\text{DG}} - \mathbf{r}_i^{\text{corr}} = \mathbf{r}_i^{\text{DG}} - \alpha(\mathbf{r}_i^{\text{DG}} - \mathbf{r}_i^{\text{FV}}) = \mathbf{r}_i^{\text{DG}} - \alpha\Delta\mathbf{r}_i \tag{2.39}$$

where $\Delta\mathbf{r}_i$ is the anti-diffusive residuals.

The calculation of the blending coefficient can be distinguished into two approaches: element-wise methods and subcell-wise methods. However, this coefficient is not computed for all elements in the domain. Instead, a sensor is used to identify troubled elements where stabilisation is necessary.

2.5.1 Sensor

In order to minimise the use of these methods, which have an important impact on the accuracy of the solution, different sensors have been developed. Troubled cells are detected following different criteria, such as the Lower Bound criteria or the Regularity criteria.

2.5.1.1 Lower Bound criteria

The Lower Bound criteria flag each cell where the density or pressure is below a specific threshold. This threshold is determined at the beginning of the simulation, making it sometimes difficult to choose. If this value is too high, the accuracy of the solution will be affected, and if this value is too small, the simulation could be unstable. However, the following conditions seem to be a good choice for any simulation

$$\rho^{\text{threshold}} = \frac{\rho^{\text{at rest}}}{2} \qquad\qquad p^{\text{threshold}} = \frac{p^{\text{at rest}}}{2} \tag{2.40}$$

2.5.1.2 Regularity criteria

This sensor utilises the regularity criterion introduced by Persson and Peraire [38]. The core idea is to assess the smoothness of the solution within each element by comparing the energy contained in the highest-degree polynomial mode with the solution energy. The regularity indicator is defined as

$$\mathcal{E} = \frac{(\rho - \hat{\rho}, \rho - \hat{\rho})_K}{(\rho, \rho)_K} \tag{2.41}$$

where $(\cdot, \cdot)_K$ denotes the L_2 norm inside the element K. ρ and $\hat{\rho}$ describe the solutions obtained using polynomial orders o and $o-1$, respectively. $(\rho - \hat{\rho}, \rho - \hat{\rho})_K$ describe the energy contained in the higher order mode, and $(\rho, \rho)_K$ represents the energy of the solution within the element K. A significant difference of energy between these two indicates the presence of sharp gradients or discontinuities, such as shocks. A threshold value $\mathcal{T}$, which depends on the polynomial order, is used to determine the presence of the shock inside the element. Following the discussion of Person and Peraire [38], Hennemann [21] describes the following ansatz

$$\mathcal{T} = a \; 10^{-b(o+1)^{0.25}} \tag{2.42}$$

where a and b are used as $\frac{1}{2}$ and 1.8, respectively, following the description of Hennemann.

The sensor is computed on each element with the coefficient α, based on the regularity indicator $\mathcal{E}$ and the threshold $\mathcal{T}$, as follows

$$\alpha = \frac{1}{1 + \exp\left(\frac{-\tilde{s}}{\mathcal{T}}(\mathcal{E} - \mathcal{T})\right)} \tag{2.43}$$

where $\tilde{s} = 9.21024$ is chosen so that the minimum value is $\alpha_{min} = 0.0001$. Finally, the value of the blending coefficient is given using this minimum value

$$\alpha = \begin{cases} 0 & \text{if } \alpha < \alpha_{\min} \\ \alpha & \text{if } \alpha_{\min} \leq \alpha \leq 1 - \alpha_{\min} \\ 1 & \text{if } 1 - \alpha_{\min} < \alpha \end{cases} \tag{2.44}$$

If $\alpha \neq 0.0$, the element is flagged as troubled, and the computation of the blending coefficient is done only for these elements.

2.5.2 Element-wise methods

Element-wise methods, such as APriori and APosteriori, apply a single blending coefficient per troubled element. APriori determines the coefficient based on the previous solution, while APosteriori uses a precomputed next time-step solution for its calculation.

2.5.2.1 APriori

APriori, described by Hennemann in [21], uses a regularity criterion, described in Sec. 2.5.1.2, to apply the limiting factor to each troubled element. A unique blending coefficient is applied for each element, based on the local solution of the previous time step.

This blending coefficient $\alpha \in [0, 1]$ is computed with Eq. 2.43 using the regularity indicator and a certain threshold, defined in Eq. 2.41 and Eq. 2.42, respectively. The computation of the blending coefficient is provided in Sec. 2.5.1.2.

In order to improve the accuracy of the method, the blending coefficient can be diffused by looking at the neighbouring elements. The final blending coefficient is computed as

$$\alpha = \max_{K' \in N(K)} \left\{ \alpha, 0.5\alpha^{K'} \right\} \tag{2.45}$$

where $N(K)$ corresponds to the direct neighbours of the element K.

2.5.2.2 APosteriori

The APosteriori method, described by Lin [32], uses the Lower Bound criteria, defined in Sec. 2.5.1.1, to find the troubled cells where the limiting factor should be applied. Here, the coefficient is computed at each interpolation and the maximum value is employed to the element. This method uses a precomputed next time-step solution to ensure that

$$\mathbf{u}_i^{n+1} \in \mathcal{A}(\rho_i^{\min}, \rho e_i^{\min}) = \left\{ \mathbf{u}_i \mid \rho_i \geq \rho_i^{\min} > 0, \ \rho e_i \geq \rho e_i^{\min} > 0 \right\} \tag{2.46}$$

Changing Eq. 2.39 to use the low-order solution as made in [32], the next time-step solution is computed as

$$\mathbf{u}_i^{n+1} = \mathbf{u}_i^{\mathrm{FV},n+1} + \frac{\Delta t}{m_i}(1 - \alpha_i)\Delta \mathbf{r}_i \tag{2.47}$$

The limiting factor $1 - \alpha_i$, taken as $\hat{\alpha}_i$ for readability, is defined as the minimum value for which the next time-step solution remains in the admissible set $\mathcal{A}(\rho_i^{\min}, \rho e_i^{\min})$. This factor is computed by solving the following inequations

$$\rho_i^{\min} \leq \rho_i^{\mathrm{FV}} + \hat{\alpha}_i \frac{\Delta t}{m_i}\Delta r_i^{\rho} \qquad\qquad \rho e_i^{\min} \leq \rho e_i^{\mathrm{FV}} + \hat{\alpha}_i \frac{\Delta t}{m_i}\Delta r_i^{\rho e} \tag{2.48}$$

where ρ_i^{FV} and ρe_i^{FV} are the low-order solution at the next time-step, while $\frac{\Delta t}{m_i} \Delta r_i^\rho$ and $\frac{\Delta t}{m_i} \Delta r_i^{\rho e}$ are the weighted anti-diffusive residuals times the time step. The blending factor for density and internal energy can be find as

$$
\begin{aligned}
\hat{\alpha}_i^\rho &= \begin{cases} 1 & \text{if } \rho_i^{\text{FV}} + \frac{\Delta t}{m_i} \Delta r_i^\rho \geq 0 \\ \max\left(\frac{m_i}{\Delta t} \frac{-\rho_i^{\text{FV}} + \rho_i^{\min}}{\Delta r_i^\rho}, 0 \right) & \text{otherwise} \end{cases} \\
\hat{\alpha}_i^{\rho e} &= \begin{cases} 1 & \text{if } \{\alpha \geq 0 \mid a\alpha^2 + b\alpha + c = 0\} = \emptyset \\ \{\alpha \geq 0 \mid a\alpha^2 + b\alpha + c = 0\} & \text{otherwise} \end{cases}
\end{aligned}
\tag{2.49}
$$

with a, b and c a combination of the low order solution, anti-diffusive residuals, and the minimum values for density and internal energy described in [32].

After computing both limiters, the final limiter is computed as the minimum value of these two

$$
1 - \alpha_i = \hat{\alpha}_i = \min\left(\hat{\alpha}_i^\rho, \hat{\alpha}_i^{\rho e} \right)
\tag{2.50}
$$

The minimum values for density and internal energy are given by the finite volume solution and a relaxation factor, ζ, which take a default value of 0.5 in ForDGe,

$$
\rho_i^{\min} = \zeta \rho_i^{\text{FV}}, \quad \rho e_i^{\min} = \zeta \rho e_i^{\text{FV}}
\tag{2.51}
$$

2.5.3 Subcell-wise methods

In contrast to element-wise methods, the subcell-wise approaches, APosteriori Subcell and MCL, compute a blending coefficient at each interpolation point inside the troubled elements. These methods enable a more selective and precise limiting process, resulting in a higher computational cost.

In order to compute this coefficient, the APosteriori Subcell and MCL methods use the anti-diffusive residuals in a directionally split manner, described in [16, 37, 42]. Each interpolation point is treated as a subcell with interfaces, and the anti-diffusive residuals are computed for each interface based on the fluxes crossing it. To construct these interface residuals, the contributions from all points with lower coordinates, aligned with the interface normal, are summed. The Fig. 2.4 illustrates the points considered for each interface.
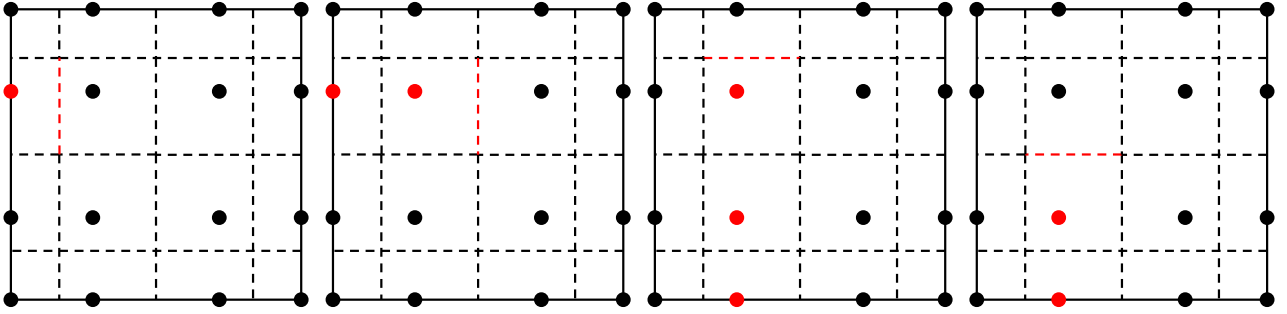
Figure 2.4: Contribution of the interface residuals on a 3rd order in a element with Gauss-Lobatto quadrature. The points are the quadrature points and the dashed line represent the interface of FV. Each red points contributes to the red subcell interface.

After computing the residuals at each interface, the split-form anti-diffusive residual is constructed for each point based on directional contributions

$$\Delta \mathbf{r}_i = \sum_{d=1}^{\dim} \Delta \mathbf{r}_i^{d,+} - \Delta \mathbf{r}_i^{d,-} = \sum_{j \in N^*(i)} \Delta \mathbf{r}_{ij} \tag{2.52}$$

where $N^*(i)$ denotes the set of neighbours of point i, and $\Delta \mathbf{r}_{ij}$ represents the residual contribution exchanged between point i and its neighbour j. The superscripts $d, +$ and $d, -$ refer to residuals constructed from points with strictly lower coordinates than point ii along dimension d, and from the same set including point i itself, respectively.
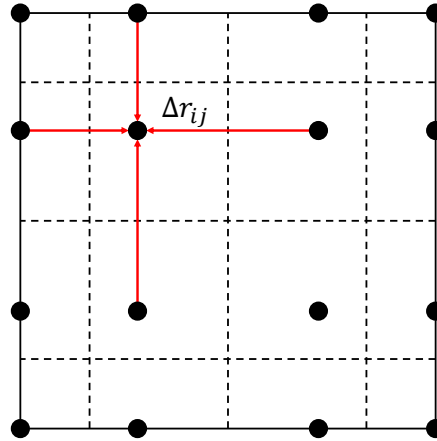
Figure 2.5: Visualization of the residual by part on a 3rd order in a element with Gauss-Lobatto quadrature. The points are the quadrature points and the dashed line represent the interface of FV.

Furthermore, for subcell methods, a bound is imposed at each interpolation point, taking into account the values of its neighbouring points. Guermond and Popov [17] introduced a two-point function, known as the bar state, which is used to define the minimum and maximum

bounds of each point. It is defined as follows

$$\overline{u}_{ij} = \frac{u_i + u_j}{2} + \frac{1}{2\lambda_{ij}^{\max}}(F(u_i) - F(u_j)) \tag{2.53}$$

where $\lambda_{ij}^{\max}$ denotes the convective spectral radius between points i and j. Due to the properties of LLF, the bar state is symmetric, i.e., $\overline{u}_{ij} = \overline{u}_{ji}$, and, as shown by Guermond and Popov [17], this formulation ensures the preservation of all convex invariants for hyperbolic initial value problems.

2.5.3.1 APosteriori Subcell

The APosteriori Subcell method, developed by Rueda-Ramirez in [43], uses the Lower Bound criteria, defined in Sec. 2.5.1.1, similarly to APosteriori. It also uses a predicted solution at the next time step to calculate the coefficient. By expanding Eq. 2.39 using the split anti-diffusive residuals and decomposing the time evolution, the limiting factor is found using the following equation

$$\mathbf{u}_i^{n+1} = \mathbf{u}_i^{\mathrm{DG},n} - \frac{\Delta t}{m_i} \sum_{j \in N^*(i)} \alpha_{ij} \Delta \mathbf{r}_{ij} \tag{2.54}$$

With the Zalesak-type limiter [57], the blending coefficient for density at each interpolation point is computed as

$$P^- = \frac{\Delta t}{m_i} \sum_{j \in N^*(i)} \min(0, \Delta r_{ij}^\rho) \qquad\qquad P^+ = \frac{\Delta t}{m_i} \sum_{j \in N^*(i)} \max(0, \Delta r_{ij}^\rho)$$

$$\alpha_i^- = 1 - \min\left(1, \frac{\rho_i^{\min} - \rho_i^{\mathrm{FV}}}{P^-}\right) \qquad\qquad \alpha_i^+ = 1 - \min\left(1, \frac{\rho_i^{\max} - \rho_i^{\mathrm{FV}}}{P^+}\right)$$

$$\alpha_i = \max(\alpha_i^-, \alpha_i^+)$$

where the bounds $\rho_i^{\min}$ and $\rho_i^{\max}$ are computed with the minimum and maximum of density bar state amoung the neighbouring interpolation points and itself, denoted by the notation $N(i)$, as follows

$$\rho_i^{\min} = \min_{j \in N(i)} \overline{\rho}_{ij} \qquad\qquad \rho_i^{\max} = \max_{j \in N(i)} \overline{\rho}_{ij} \tag{2.55}$$

note that $\overline{\rho}_{ii} = \rho_i$ using the definition in Eq. 2.53.

To prevent the pressure from becoming negative, an alternative method is used, since it is not linearly related to the conservative variables. Rueda-Ramirez [43] proposed to compute this limiter using a Newtown-bisection loop. Instead of using pressure, the specific entropy $\rho e^{\gamma - 1}$, which implies positivity of the pressure, is used to compute the blending coefficient at each interpolation point. The coefficient is obtained by solving $2d$ non linear problems, one for each direction of the interface, using the previous coefficient to initialise the following equation

$$\tilde{\mathbf{u}}_i^{n+1} = \mathbf{u}_i^{\mathrm{DG},n+1} - \Gamma \alpha_i \frac{\Delta t}{m_i} \Delta \mathbf{r}_{ij} \quad \forall j \in N^*(i) \tag{2.56}$$

where $\Gamma = 2d$ guarantees the respect of the bound and $\tilde{u}_i^{n+1}$ is the state vector where the constraint on the specific entropy is enforced.

After computing this coefficient at each interpolation point, the blending factor at each interface is computed as

$$\alpha_{ij} = \max(\alpha_i, \alpha_j) \tag{2.57}$$

2.5.3.2 Monolithic convex limiting

MCL, proposed by Hajduk and Kuzmin in [18, 31] and further extended by Rueda-Ramirez in [44], uses the Regularity criteria, in Sec. 2.5.1.2, such as APriori to find troubled elements.

Compared to the different methods, it directly computes the corrected anti-diffusive residuals, $\alpha_{ij}\Delta\mathbf{r}_{ij}$, using two successive limiters, one for the density and one for the pressure. First, a density limiter is applied to ensure that the density remains positive, and the density corrected anti-diffusive residuals is further used to compute a pressure limiter. The hybrid solution is then computed as

$$m_i \dot{\mathbf{u}}_i = \mathbf{r}_i^{\mathrm{DG}} - \sum_{j \in N^*(i)} (1 - \alpha_{ij})\Delta\mathbf{r}_{ij} \tag{2.58}$$

Note that the definition of the blending factor in [44] is the inverse of the previous convention. Let $\hat{\alpha} = 1 - \alpha$ denote the blending factor as used by Rueda-Ramirez, where $\hat{\alpha} = 0$ corresponds to a fully FV solution and $\hat{\alpha} = 1$ yields the DG solution. This formulation is advantageous because the product of two values in $[0, 1]$ remains within the same interval and tends to decrease, which is exploited when multiplying the density and pressure blending factors to compute the anti-diffusive residuals. This approach ensures that the resulting value of α is closer to FV in troubled regions, ensuring to maintain positivity where it is needed.

The different limiters use a limited version of the bar state to compute the blending coefficient, the definition of the limited bar state is

$$\overline{\mathbf{u}}_{ij}^{\mathrm{Lim}} = \overline{\mathbf{u}}_{ij} + \frac{\hat{\alpha}_{ij}\Delta\mathbf{r}_{ij}}{\lambda_{ij}^{\max}} \tag{2.59}$$

Density limiter

In order to keep $\overline{\rho}_{ij}^{\mathrm{Lim}}$ and $\overline{\rho}_{ji}^{\mathrm{Lim}}$ within $[\rho_i^{\min}, \rho_i^{\max}]$, one can impose the following inequalities

$$\rho_i^{\min} \leq \overline{\rho}_{ij} + \frac{\hat{\alpha}_{ij}^\rho \Delta r_{ij}^\rho}{\lambda_{ij}^{\max}} \leq \rho_i^{\max} \qquad\qquad \rho_j^{\min} \leq \overline{\rho}_{ij} - \frac{\hat{\alpha}_{ij}^\rho \Delta r_{ij}^\rho}{\lambda_{ij}^{\max}} \leq \rho_j^{\max} \tag{2.60}$$

Using $\overline{\rho}_{ij} = \overline{\rho}_{ji}$ and $\Delta r_{ij}^\rho = -\Delta r_{ji}^\rho$.

Developing those inequalities, one can find an upper and lower bound for $\hat{\alpha}_{ij}\Delta r_{ij}^\rho$

$$\rho_i^{\min} - \overline{\rho}_{ij} \leq \frac{\hat{\alpha}_{ij}^\rho \Delta r_{ij}^\rho}{\lambda_{ij}^{\max}} \leq \rho_i^{\max} - \overline{\rho}_{ij} \qquad\qquad \overline{\rho}_{ij} - \rho_j^{\max} \leq \frac{\hat{\alpha}_{ij}^\rho \Delta r_{ij}^\rho}{\lambda_{ij}^{\max}} \leq \overline{\rho}_{ij} - \rho_j^{\min} \tag{2.61}$$

Therefore, to guarantee the condition on both $\overline{\rho}_{ij}^{\text{Lim}}$ and $\overline{\rho}_{ji}^{\text{Lim}}$, the upper and lower bounds are defined as

$$\begin{aligned}
\Delta r_{ij}^{\rho;-} &= \lambda_{ij}^{\max} \max\{\rho_i^{\min} - \overline{\rho}_{ij}, \overline{\rho}_{ij} - \rho_j^{\max}\} \\
\Delta r_{ij}^{\rho;+} &= \lambda_{ij}^{\max} \min\{\rho_i^{\max} - \overline{\rho}_{ij}, \overline{\rho}_{ij} - \rho_j^{\min}\}
\end{aligned} \tag{2.62}$$

Finally, one can compute the anti-diffusive residuals with

$$\hat{\alpha}_{ij}^{\rho} \Delta r_{ij}^{\rho} = \begin{cases} \max\{\Delta r_{ij}^{\rho}, \Delta r_{ij}^{\rho;-}\} & \text{if } \Delta r_{ij}^{\rho} \leq 0, \\ \min\{\Delta r_{ij}^{\rho}, \Delta r_{ij}^{\rho;+}\} & \text{otherwise} \end{cases} \tag{2.63}$$

In order to maintain consistency, the same limiting factor is applied to all other conservative variables (momentum and energy).

$$\hat{\alpha}_{ij}^{\rho} = \begin{cases} 1 & \text{if } \Delta r_{ij}^{\rho} \approx 0 \\ \dfrac{\alpha_{ij} \Delta r_{ij}^{\rho} + \epsilon \ \text{sign}(\Delta r_{ij}^{\rho})}{\Delta r_{ij}^{\rho} + \epsilon \ \text{sign}(\Delta r_{ij}^{\rho})} & \text{otherwise} \end{cases} \tag{2.64}$$

where ϵ is a small number. Therefore, the anti-diffusive fluxes after the density limiter are

$$\hat{\alpha}_{ij}^{\rho} \Delta \mathbf{r}_{ij} = \begin{pmatrix} \hat{\alpha}_{ij}^{\rho} \Delta r_{ij}^{\rho} \\ \hat{\alpha}_{ij}^{\rho} \Delta r_{ij}^{\rho \mathbf{v}} \\ \hat{\alpha}_{ij}^{\rho} \Delta r_{ij}^{\rho E} \end{pmatrix} \tag{2.65}$$

In the following, the density-limited anti-diffusive residuals will be denoted as $\Delta \tilde{\mathbf{r}}_{ij} = \hat{\alpha}_{ij}^{\rho} \Delta \mathbf{r}_{ij}$ to highlight the application of the density limiter.

Pressure limiter

Following the density limiter, the pressure limiter computes a limiting factor $\hat{\alpha}_{ij}^{p}$ to maintain a positive pressure. Using a calorically perfect gas assumption, the pressure can be given with

$$p = (\gamma - 1)\rho e = (\gamma - 1)\left(\rho E - \rho \frac{\|\mathbf{v}\|^2}{2}\right) \tag{2.66}$$

Positivity is guaranteed with the limited bar state of the pressure density, ρp

$$\overline{\rho}_{ij}^{\text{Lim}} \overline{\rho E}_{ij}^{\text{Lim}} - \frac{\|\overline{\rho \mathbf{v}}_{ij}^{\text{Lim}}\|^2}{2} \geq 0 \tag{2.67}$$

where the limited bar state is defined as

$$\overline{\mathbf{u}}_{ij}^{\text{Lim}} = \overline{\mathbf{u}}_{ij} + \frac{\hat{\alpha}_{ij}^{p} \Delta \tilde{\mathbf{r}}_{ij}}{\lambda_{ij}^{\max}} \qquad\qquad \overline{\mathbf{u}}_{ji}^{\text{Lim}} = \overline{\mathbf{u}}_{ij} - \frac{\hat{\alpha}_{ij}^{p} \Delta \tilde{\mathbf{r}}_{ij}}{\lambda_{ij}^{\max}} \tag{2.68}$$

injecting Eq. 2.68 into Eq. 2.67, dropping index for readability and introducing scaled bar states $\overline{\mathbf{w}}_{ij} = \lambda_{ij}^{\max} \overline{\mathbf{u}}_{ij}$, the inequality becomes

$$(\overline{w}^{\rho} + \hat{\alpha}^{p} \Delta \tilde{r}^{\rho})(\overline{w}^{\rho E} + \hat{\alpha}^{p} \Delta \tilde{r}^{\rho E}) - \frac{\|(\overline{w}^{\rho} + \hat{\alpha}^{p} \Delta \tilde{r}^{\rho})\|^2}{2} \geq 0 \tag{2.69}$$

$$\left(\underbrace{\frac{||\Delta\tilde{r}^{\rho\mathbf{v}}||^2}{2} - \Delta\tilde{r}^\rho\Delta\tilde{r}^{\rho E}}_{A_{ij}}\right)\hat{\alpha}^{p,2} + \left(\underbrace{||\overline{w}^{\rho\mathbf{v}}\Delta\tilde{r}^{\rho\mathbf{v}}|| - \overline{w}^\rho\Delta\tilde{r}^{\rho E} - \overline{w}^{\rho E}\Delta\tilde{r}^\rho}_{B_{ij}}\right)\hat{\alpha}^p \leq \underbrace{\overline{w}^\rho\overline{w}^{\rho E} - \frac{||\overline{w}^{\rho\mathbf{v}}||^2}{2}}_{Q_{ij}}$$
(2.70)

To solve this quadratic inequality, Kuzmin [31] suggests reformulating $A_{ij}\hat{\alpha}^{p,2} + B_{ij}\hat{\alpha}^p \leq Q_{ij}$ as $P_{ij}\hat{\alpha}^p \leq Q_{ij}$, using the property that $\alpha^2 \leq \alpha$ for $\alpha \in [0,1]$, where P_{ij} is defined as

$$P_{ij} = \max\{0, A_{ij}\} + |B_{ij}| \tag{2.71}$$

the pressure blending coefficient can be computed with

$$\hat{\alpha}_{ij}^p = \begin{cases} \frac{Q_{ij}}{P_{ij}} & \text{if } P_{ij} > Q_{ij} \\ 1 & \text{otherwise} \end{cases} \tag{2.72}$$

Corrective residuals

After computing the pressure blending coefficient, the corrective residuals can be computed by multiplying the density-limited anti-diffusive residuals by the blending factor. To summarise this process, the corrective anti-diffusive residuals are computed by summing the contribution of each interface of the interpolation points

$$\mathbf{r}_i^{\text{corr}} = \alpha_i\Delta\mathbf{r}_i = \sum_{j\in N^*(i)}(1 - \hat{\alpha}_{ij}^p\hat{\alpha}_{ij}^\rho)\Delta\mathbf{r}_{ij} \tag{2.73}$$

Note that the final blending coefficient with the convention used by Rueda is given by $\hat{\alpha}_{ij} = \hat{\alpha}_{ij}^\rho\hat{\alpha}_{ij}^p$ and is transformed to $\alpha_{ij} = 1 - \hat{\alpha}_{ij}$ to retrieve the convention used in ForDGe.

Bounds

Two types of bounds have been described by Ramirez. The first is called MCL local bounds. Consider direct neighbours of a point to avoid creating new local extrema. Therefore, a minimum and maximum values for each point is computed, as made for APosteriori Subcell Sec. 2.5.3.1

$$\rho_i^{\min} = \min_{j\in N(i)}\overline{\rho}_{ij} \qquad\qquad \rho_i^{\max} = \max_{j\in N(i)}\overline{\rho}_{ij} \tag{2.74}$$

where $N(i)$ is the set of direct neighbours of i plus the interpolation point i, $\overline{\rho}_{ii} = \rho_i$ by definition. The density limiter is computed as previously described with Eq. 2.62.

The second type is called MCL global bounds which, on the other hand, only imposes a minimum value of zero to prevent the density to become negative.

$$\rho_i^{\min} \geq 0.0 \qquad\qquad \rho_i^{\max} = \max_{j\in N(i)}\overline{\rho}_{ij} \tag{2.75}$$

This choice of bounds simplifies the upper and lower bounds. As the two inequalities of Eq. 2.61 are simplified to one sided inequalities, Eq. 2.62 becomes

$$
\begin{aligned}
\Delta r_{ij}^{\rho;-} &= -\lambda_{ij}^{\max} \, \overline{\rho}_{ij} \\
\Delta r_{ij}^{\rho;+} &= \lambda_{ij}^{\max} \, \overline{\rho}_{ij}
\end{aligned}
\tag{2.76}
$$

the upper and lower are used to compute the limited anti-diffusive residuals of the density with Eq. 2.63

Chapter 3

Results

3.1 Methods to compare

The following chapter describes the accuracy, spatial, and temporal robustness of the different methods. The Tab. 3.1 summarises all the methods that will be used for different test cases. ESDGSEM is the principal method used here and the impact of the addition of several positivity-preserving methods, as previously described, is discussed. For positivity-preserving method, a blending coefficient of 0 means ESDGSEM is used, if this coefficient equals 1, the first-order finite volume is used, which ensures the monotonicity of the solution, helping to prevent non-physical oscillation, but this comes at the cost of reduced accuracy.

	ESDGSEM	APriori	APosteriori	APosteriori Subcell	MCL local	MCL global
line	———	•••••	·–·–·	———	———	———
sensor	None	Regularity	Lower bound	Lower bound	Regularity	Regularity

Table 3.1: Description of the different methods used for the test case

3.2 Time discretization

In order to conduct all simulations, the Strong Stability Preserving Runge-Kutta with five stages and fourth order accuracy, SSPRK(5,4), is employed for time discretization, as described by Spiteri and Ruuth in [45, 50]. This method offers a notable improvement in stability compared to other Runge-Kutta schemes. SSP methods are time integration schemes that preserve the nonlinear stability of forward Euler by expressing higher order steps as convex combinations of it, using a restricted time step based on the SSP coefficient, ideal for hyperbolic PDEs and problems with discontinuities.- The s-stage characterises the number of intermediate steps inside a single time-step. The Runge-Kutta scheme is defined as follows

$$\mathbf{u}^{(0)} = \mathbf{u}^n \qquad \mathbf{u}^{(l)} = \sum_{k=0}^{l-1}(\alpha_{lk}\mathbf{u}^{(k)} + \Delta t\beta_{lk}\mathbf{r}^{(k)}) \qquad \mathbf{u}^{n+1} = \mathbf{u}^{(s)} \qquad (3.1)$$

where $s = 5$ and the coefficient α_{lk} and β_{lk} are chosen to satisfy the Runge-Kutta fourth order conditions. $\mathbf{r}^{(k)}$ correspond to the residuals as shown in Eq. 2.38.

3.3   Advection Density wave

In order to test the convergence of MCL, Zhen-Hua Jiang [26] uses the advection of a density wave to assess the convergence of a hybrid DG/FV method. This two-dimensional Euler test case gives a smooth solution. The initial conditions are the following

$$\rho_0(x,y) = 1 + 0.2\sin(x+y) \qquad \vec{v}_0(x,y) = \begin{pmatrix} 1 \\ 1 \end{pmatrix} \qquad p_0(x,y) = 1 \qquad (3.2)$$

with a domain $\Omega = [0, 2\pi]^2$ using periodic boundaries. The exact solution is given by the following equations

$$\rho(x,y,t) = 1 + 0.2\sin(x+y-2t) \qquad \vec{v}(x,y,t) = \begin{pmatrix} 1 \\ 1 \end{pmatrix} \qquad p(x,y,t) = 1 \qquad (3.3)$$

Simulations are carried out over the time interval $t \in [0, 0.1]$ using a sufficiently small time step to ensure that temporal discretization errors are negligible. The convergence analysis is performed on five grid resolutions, $Ne = [4, 8, 16, 32, 64]$, where Ne denotes the number of cells per spatial direction. The L_2 error, using the density, is computed using the Eq. 3.4.

$$L_2 = \sqrt{\sum_i^N \frac{(\rho_i^{\text{compute}} - \rho_i^{\text{analytical}})^2}{N}} \qquad (3.4)$$
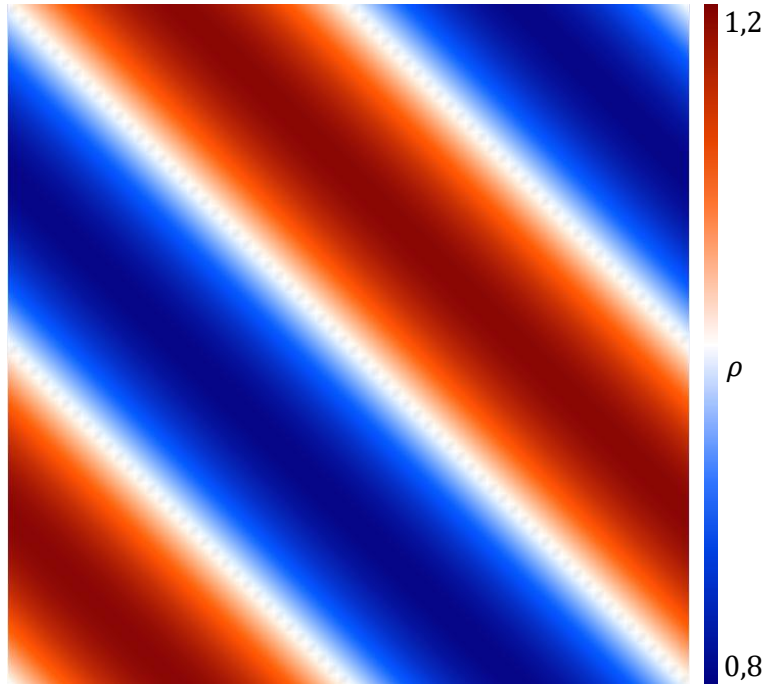

Figure 3.1: Initial density of the advection density wave Eq. 3.2 using MCL - local bounds, $o = 3$ and $Ne = 64$

Ne	$o = 1$		$o = 2$		$o = 3$		$o = 4$	
	L_2	Order	L_2	Order	L_2	Order	L_2	Order
4	4.66e-02	-	2.52e-02	-	5.59e-04	-	5.80e-05	-
8	2.34e-02	0.99	7.65e-04	5.04	3.47e-05	4.01	2.61e-06	4.48
16	2.00e-02	0.22	1.29e-04	2.57	3.19e-06	3.44	1.01e-07	4.69
32	1.05e-03	4.23	2.30e-05	2.48	3.01e-07	3.41	3.82e-09	4.72
64	2.73e-04	1.95	3.75e-06	2.62	6.04e-09	5.64	1.13e-09	1.75

Table 3.2: L_2 error and observed order of convergence for the MCL method with local bounds at various grid resolutions, $Ne = [4, 8, 16, 32, 64]$ and different polynomial order, $o = [1, 2, 3, 4]$ of a smooth density advection with initial conditions Eq. 3.2.

Ne	$o = 1$		$o = 2$		$o = 3$		$o = 4$	
	L_2	Order	L_2	Order	L_2	Order	L_2	Order
4	4.15e-02	-	4.38e-02	-	5.59e-04	-	5.80e-05	-
8	1.37e-02	1.60	7.65e-04	5.50	3.47e-05	4.01	2.61e-06	4.48
16	3.89e-03	1.81	1.29e-04	2.57	3.19e-06	3.44	1.01e-07	4.69
32	1.05e-03	1.88	2.30e-05	2.48	3.01e-07	3.41	3.82e-09	4.72
64	2.73e-04	1.95	3.75e-06	2.62	6.04e-09	5.64	1.13e-09	1.75

Table 3.3: L_2 error and observed order of convergence for the MCL method with global bounds at various grid resolutions, $Ne = [4, 8, 16, 32, 64]$ and different polynomial order, $o = [1, 2, 3, 4]$ of a smooth density advection with initial conditions Eq. 3.2.

Ne	$o = 1$		$o = 2$		$o = 3$		$o = 4$	
	L_2	Order	L_2	Order	L_2	Order	L_2	Order
4	2.51e-01	-	1.71e-01	-	1.24e-01	-	9.95e-02	-
8	1.82e-01	0.46	1.06e-01	0.69	7.75e-02	0.67	6.34e-02	0.64
16	1.16e-01	0.65	5.81e-02	0.86	4.55e-02	0.77	3.84e-02	0.73
32	6.38e-02	0.87	2.98e-02	0.96	2.41e-02	0.91	2.03e-02	0.92
64	3.22e-02	0.98	1.49e-02	0.99	1.21e-02	0.98	1.01e-02	0.99

Table 3.4: L_2 error and observed order of convergence of FV at various grid resolutions, $Ne = [4, 8, 16, 32, 64]$ and different polynomial order, $o = [1, 2, 3, 4]$ of a smooth density advection with initial conditions Eq. 3.2.

Tab. 3.2 and Tab. 3.3 present the L_2 error norms and the observed orders of convergence for MCL with both local and global bounds. The results demonstrate that, for polynomial orders $o = 1$ to $o = 4$, the MCL approach achieves convergence rates close to the theoretical order of $o + 1$ expected for DG schemes on smooth problems. The global bounds showed a slightly higher convergence rate for the first two polynomial orders compared to the local bounds, but

both methods exhibit similar convergence behaviour for higher orders. Notably, the method maintains high accuracy in all tested resolutions, with the L_2 error decreasing proportionally to mesh refinement. Tab. 3.4 shows the L_2 error and observed order of convergence for the FV method, the first order of convergence is observed for all polynomial orders, which is expected as the FV method.

The convergence rates observed in Tab. 3.2 and Tab. 3.3 are consistent with the theoretical expectations for high-order DG methods, confirming the effectiveness of the DG-FV hybrid approach in maintaining accuracy while ensuring the preservation of positivity, even though the problem remains smooth. This convergence behaviour is further illustrated in Fig. 3.2, which highlights the expected $o + 1$ convergence rate.
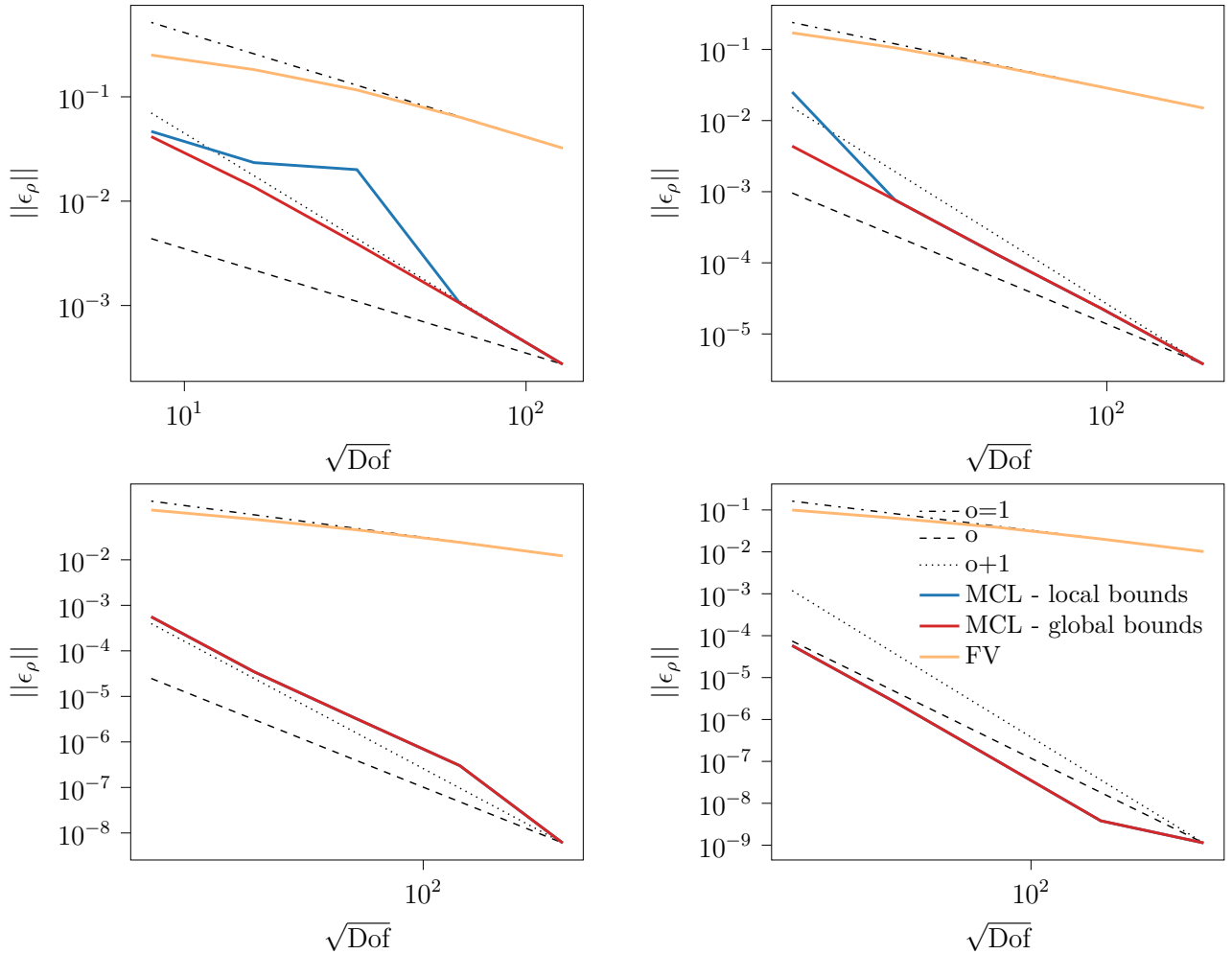
Figure 3.2: L_2 error convergence for the advection of a density wave Eq. 3.2 using MCL with local bounds (blue) and global bounds (red) and FV (orange) for polynomial orders $o = 1$ (top left), $o = 2$ (top right), $o = 3$ (bottom left), and $o = 4$ (bottom right). The dash-dot line corresponds to the first order convergence $o = 1$ while the dashed line represents the theoretical convergence rate of o and the dotted line is the convergence rate of $o + 1$.

3. Results

3.4 Kelvin-Helmholtz instability

The Kelvin-Helmholtz instability (KHI) is a common fluid instability that develops at the interface between fluids of different densities and velocities. Leading to an exponential growth of the perturbations and creation of vortical structures. This test case simulates a two-dimensional inviscid flow using the following initial conditions

$$\rho_0(x,y) = \frac{1}{2} + \frac{3}{4}B \qquad \vec{v}_0(x,y) = \begin{pmatrix} \frac{1}{2}(B-1) \\ \frac{1}{10}\sin(2\pi x) \end{pmatrix} \qquad p_0(x,y) = 1 \qquad (3.5)$$

where $B = \tanh(15y + 7.5) - \tanh(15y - 7.5)$, and the computational domain is $\Omega = [-1,1]^2$ with periodic boundary conditions.

This test case provides an initial comparison of the different methods. Although this instability does not involve shocks, stabilisation is necessary because of small-scale vortices that can lead to negative density or pressure values. As a result, ESDGSEM alone is not stable and fails when the vortices become under-resolved, around $t = 3.7$s. As illustrated in Fig. 3.3, the different layers interact and form small vortices, which are particularly visible in the simulations using APosteriori and APosteriori Subcell methods. In contrast, Apriori and MCL approaches, represented here with only global bounds as local and global bounds yields similar results, produce smoother results by damping these small vortices to maintain simulation stability and prevent numerical issues. Since no reference solution is available, the analysis is limited to a comparison between the different methods.
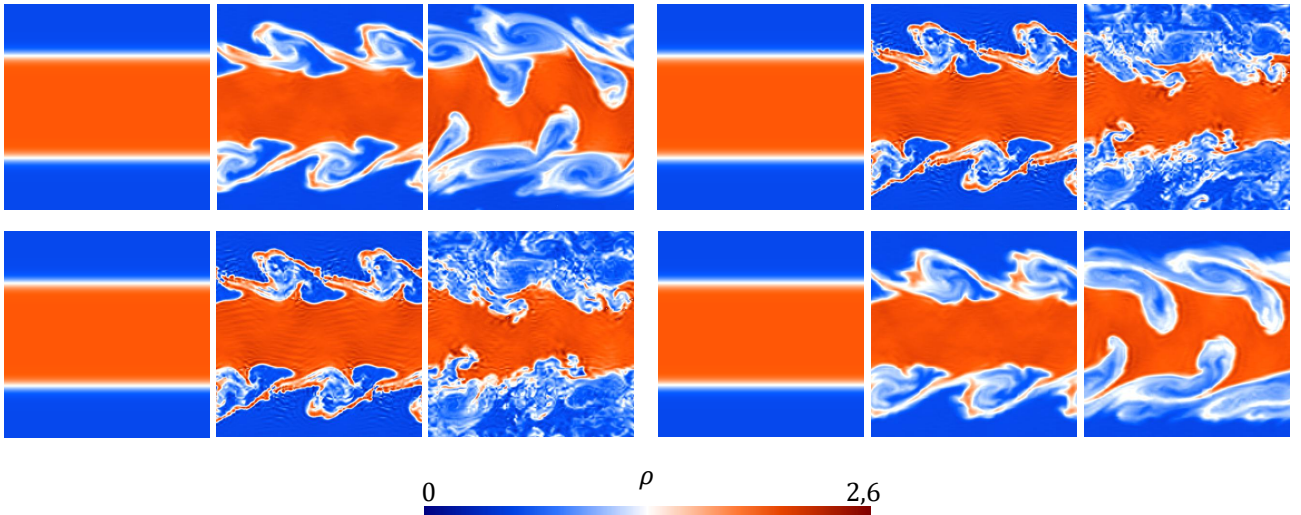

Figure 3.3: Temporal evolution of the density of Kelvin-Helmotz instability at $t = 0$ (left), $t = 4$ (centre), $t = 8$ (right) using APriori (top left), APosteriori (top right), APosteriori Subcell (bottom left) and MCL - global bounds (bottom right) with 21×21 cells, $o = 5$.

3.4.1 Results

Fig. 3.4 presents the evolution of enstrophy for various polynomial orders and mesh refinements while keeping a constant degree of freedom of 128×128. Enstrophy reflects the intensity of rotational motion and is directly linked with the presence of small vortices. Increasing the polynomial order results in higher enstrophy, enabling the capture of finer-scale structures.
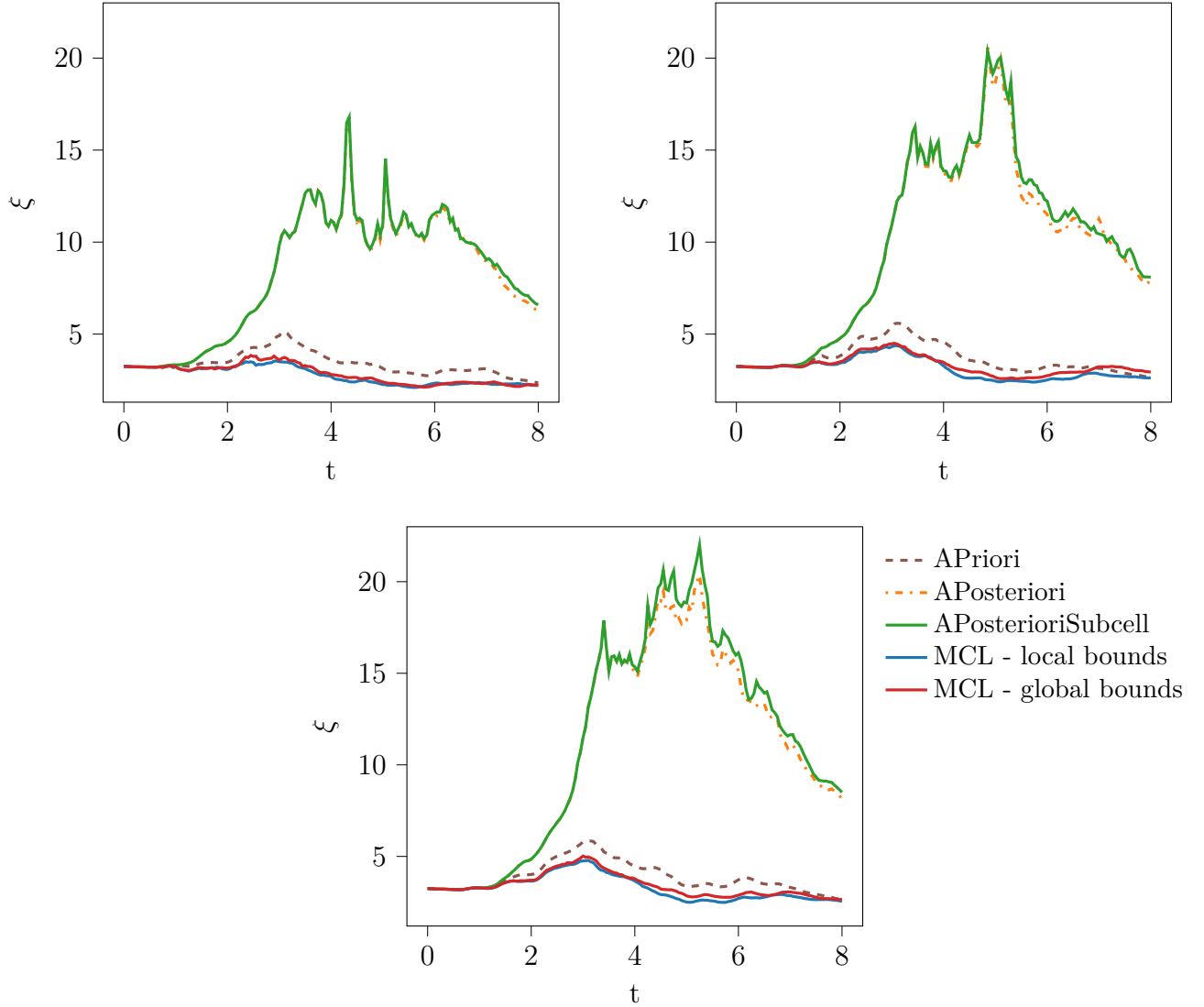

Figure 3.4: Integrals of the enstrophy on the domain during simulation. Comparison of methods using the Kelvin-Helmholtz instability simulation Eq. 3.5 for a 128×128 dof. Left: $o = 3$ and 32×32 grid, middle: $o = 4\text{-}26 \times 26$, right: $o = 5\text{-}21 \times 21$.

The MCL and APriori methods introduce more dissipation, which suppresses the formation of small vortices. The MCL with local bounds is slightly more dissipative than with global bounds, indicating that local bounds impose stricter control to prevent the creation of new extrema. In contrast, the APosteriori and APosteriori Subcell approaches apply minimal sta-

bilisation, allowing ESDGSEM to resolve these small-scale features and thus achieve higher enstrophy as observed. Furthermore, the difference between the two APosteriori methods is accentuated as the order increases.

Examining the proportion of troubled cells over time in Fig. 3.5, APriori is activated more frequently, up to 40% of cells, yet the enstrophy in Fig. 3.4 remains higher than for MCL. This suggests that APriori, despite being used more often, is less dissipative and permits more vortex formation. MCL, while triggered less frequently, yields lower enstrophy, indicating a stronger dissipation. As expected, both the APosteriori and APosteriori Subcell methods maintain a very low proportion of troubled cells, close to zero, which explains the higher.

Figure 3.5: Proportion of troubled cells on the domain along time. Comparison of methods using the Kelvin-Helmholtz instability simulation Eq. 3.5 for a 128×128 dof. Top left: $o = 3$ and 32×32 grid, Top right: $o = 4$ and 26×26 grid, bottom: $o = 5$ and 21×21 grid.

Let's now investigate the effect of increasing the number of elements while keeping the polynomial order fixed. The temporal evolution of the enstrophy is illustrated in Fig. 3.6, taking three different meshes: 16×16, 32×32, and 64×64 with a polynomial order of $o = 3$.
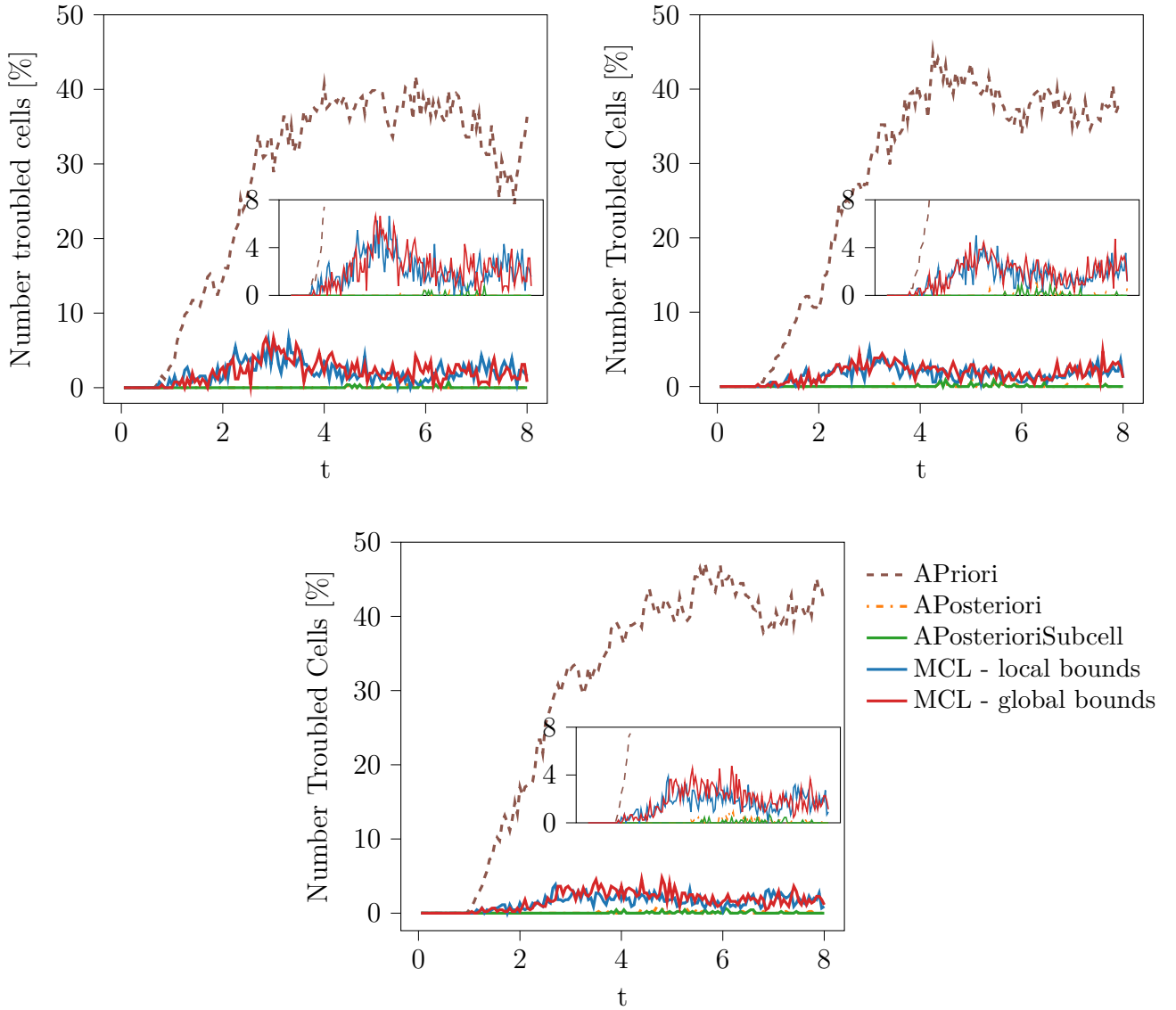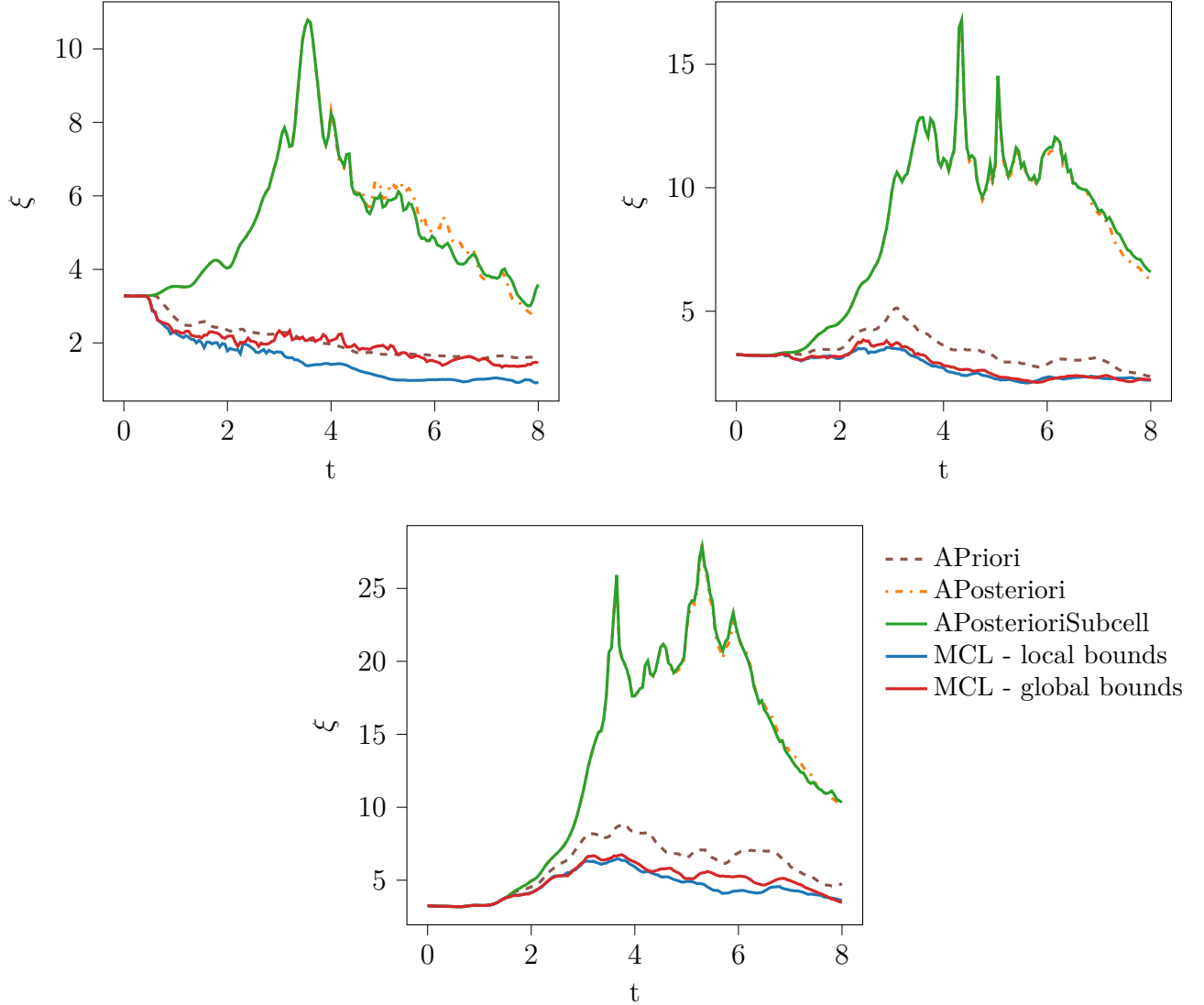

Figure 3.6: Proportion of troubled cells on the domain along time. Comparison of methods using the Kelvin-Helmholtz instability simulation Eq. 3.5, $o = 3$. Top left: 16×16 cells, top right: 32×32 cells, bottom: 64×64 cells.

As in the previous analysis, the APosteriori and APosteriori Subcell methods produce the highest levels of enstrophy throughout the simulation, while the APriori and MCL approaches tend to smooth the vortices, reducing enstrophy production.

On the coarsest mesh, the enstrophy drops sharply for APriori and MCL. With fewer elements, each cell covers a larger part of the domain, making stabilisation more impactful on the flow structure. When triggered, it significantly dampens the development of small-scale

vortices, marking the point where these features begin to emerge but are suppressed. As the mesh is refined, enstrophy generation improves and the influence of stabilisation diminishes, though it remains noticeable for APriori and MCL.

Fig. 3.7 shows the proportion of stabilisation during simulation, with APriori affecting up to 60% of the domain on the coarsest mesh. MCL also marks a large fraction, but its proportion drops quickly with refinement, despite still generating low enstrophy, suggesting a more aggressive stabilisation. In contrast, the APosteriori and APosteriori Subcell consistently maintain a troubled-cell fraction near zero, enabling ESDGSEM to resolve vortices with minimal interference.
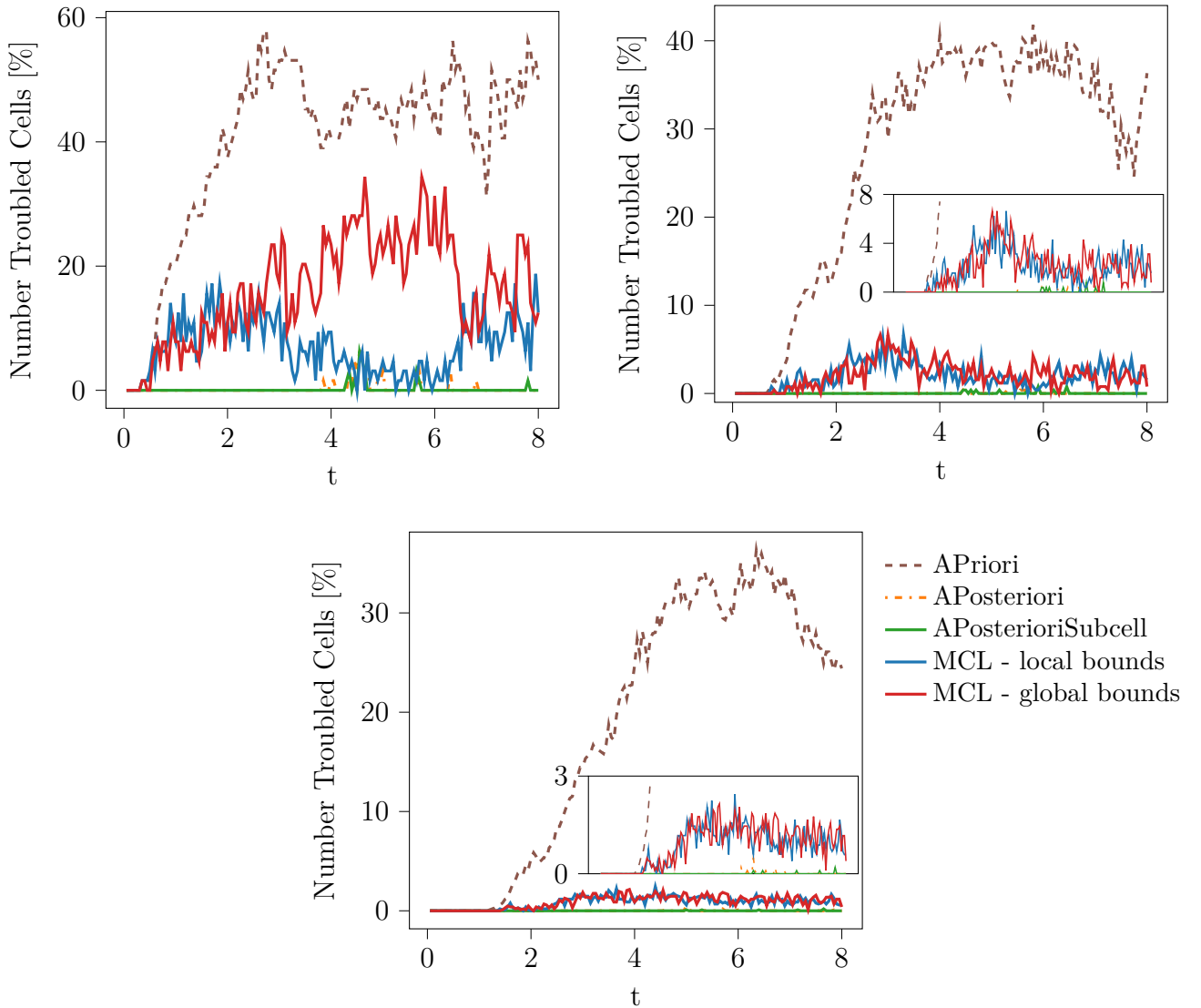

Figure 3.7: Proportion of troubled cells on the domain along time. Comparison of methods using the Kelvin-Helmholtz instability simulation Eq. 3.5, $o = 3$. Top left: 16×16 cells, top right: 32×32 cells, bottom: 64×64 cells.
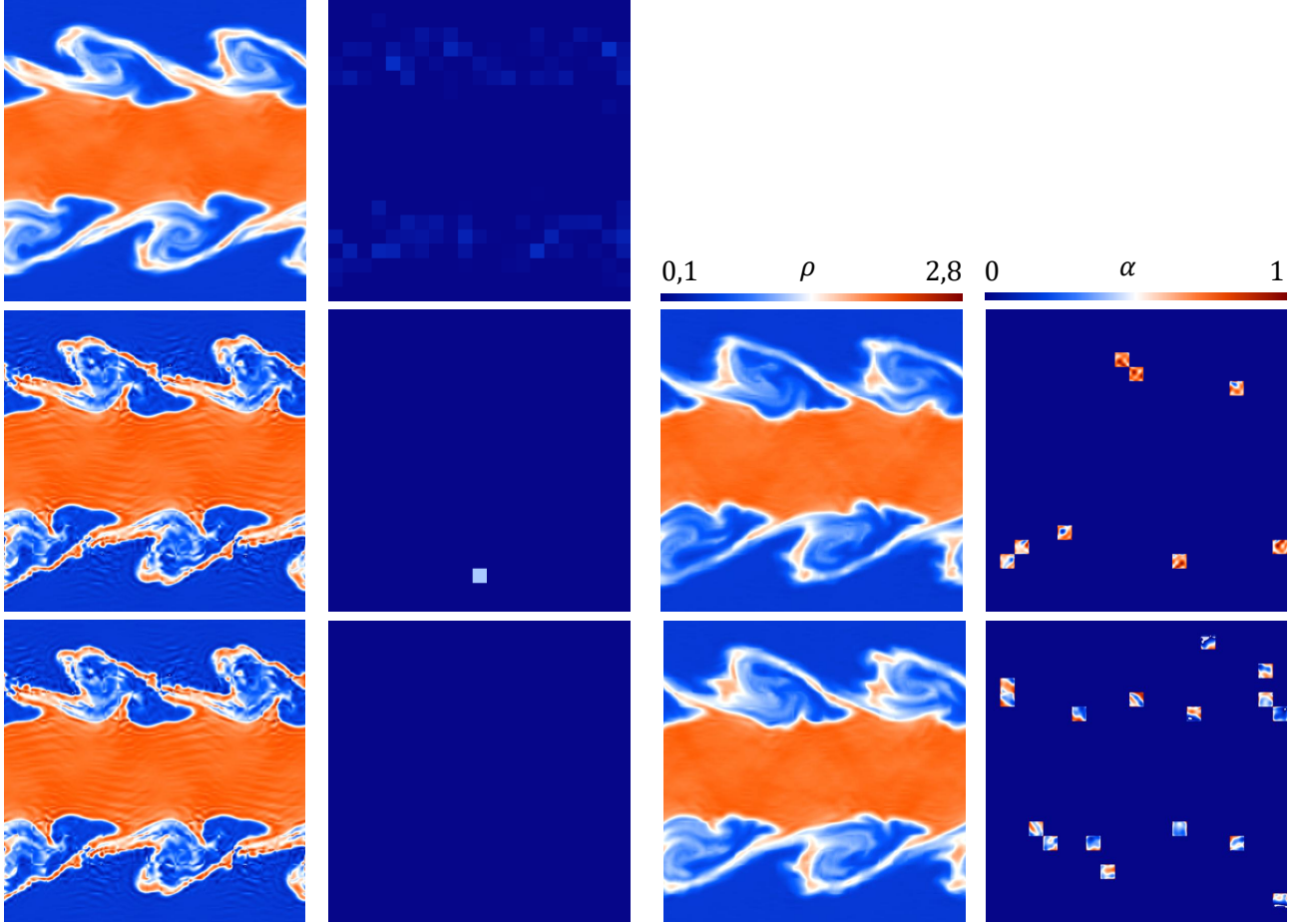
3.4.2 Blending coefficient

Figure 3.8: Density and blending coefficient at $t = 4$. Comparison of methods using the Kelvin-Helmholtz instability simulation Eq. 3.5 for a 21×21 grid and $o = 5$. Left: APriori, APosteriori, APosterioriSubcell and right: MCL - local bounds, MCL - global bounds (from top to bottom).

Fig. 3.8 shows the density and blending coefficient at $t = 4$ for each method. The density field highlights where the blending coefficient is applied, respectively, on the left and right of each column. APriori activates up to 40% of cells, but the blending coefficient remains low and aligns with the layer interfaces. Despite this low limiting factor, the high proportion suppresses the creation of small vortices and reduces enstrophy. The application of MCL is reduced by limiting factor and is higher than APriori. MCL local bounds is the more strict, avoiding the creation of new extrema. In contrast, MCL with global bounds is less restrictive but is applied to a larger portion of the domain. Both MCL variants have an impact by limiting the enstrophy growth and the formation of small-scale vortices, similarly to APriori. The APosteriori and APosteriori Subcell methods maintain a very low proportion of troubled cells, suggesting that these methods are rarely applied across the domain and have minimal influence on the ESDGSEM solution.

3.5 Strong vortex-shock interaction

This two-dimensional test case describes an unsteady inviscid flow featuring multiple shock discontinuities [28]. A strong vortex interacts with a stationary shock, leading to the observation of two key physical phenomena. First, the vortex is segmented into two parts due to compressible effects. Second, as the vortex passes through the shock, it generates several acoustic waves downstream. Some of these acoustic waves intersect with the stationary shock, resulting in alternating regions of expansion and compression. The initial conditions for the shock are

$$\rho_0(x,y) = \begin{cases} 1 & \text{if } x \leq x_0 \\ \frac{(\gamma+1)M_S^2}{2+(\gamma-1)M_S^2} \end{cases} \quad \vec{v}_0(x,y) = \begin{cases} [0,\ 0] \\ \left[\frac{2+(\gamma-1)M_S^2}{(\gamma+1)M_S^2},\ 0\right] \end{cases} \quad p_0(x) = \begin{cases} 1 \\ \frac{2\gamma M_S^2-(\gamma-1)}{\gamma+1} \end{cases}$$

$$(3.6)$$

with a shock wave Mach number of 1.5, $\Omega = [0,2] \times [0,1]$, and $\gamma = 1.4$. The vortex is placed in superposition with the previous initial conditions at $(0.25,\ 0.5)$ with the following values

$$\frac{v_\theta}{v_m} = \begin{cases} \frac{r}{a} & \text{if } r \leq a \\ \frac{a}{a^2-b^2}\left(r - \frac{b^2}{r}\right) & \text{if } a \leq r \leq b \\ 0.0 & \text{if } r \geq b \end{cases} \qquad (3.7)$$

with $a = 0.075$ and $b = 0.175$ being the vortex size parameters and $v_m = \sqrt{\gamma}M_v$ taking $M_v = 0.9$ as the vortex strength. The reference solution is obtained from a simulation using 24,300,000 cells, a finite volume solver with Roe flux, third-order TVD-RK for space and time discretization, respectively, and the MLP5 limiter for shock capture, as provided by Chongam Kim [28]. This simulation supplies several density profiles, enabling quantitative assessment of numerical methods. Lines 1 and 2, shown in Fig. 3.9, traverse the shock waves and pass through the centre of the separated vortex. These lines are taken at $y = 0.4+\epsilon$ and $x = 1.05+\epsilon$, respectively, with $\epsilon = 10^{-4}$ to avoid sampling at the cell interfaces. Fig. 3.9 presents the initial state at $t = 0$ and the solution, at $t = 0.7$, used for comparison with the reference.
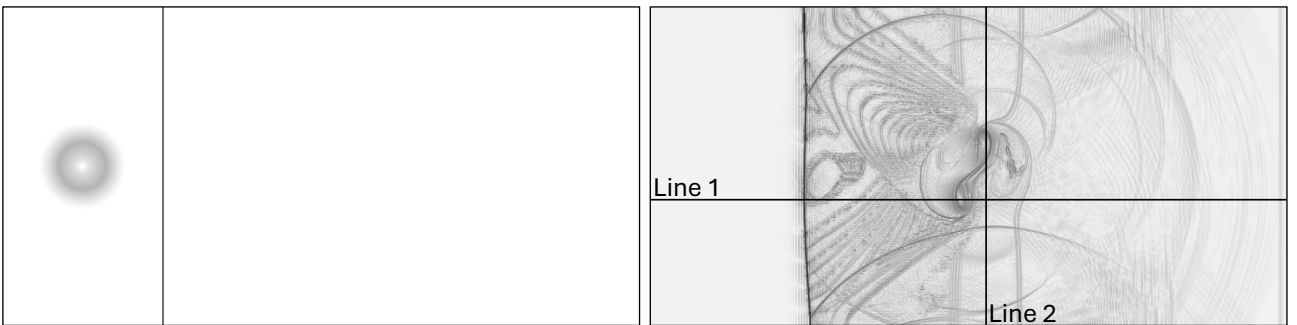
Figure 3.9: Numerical Schlieren of strong vortex-shock interaction at $t = 0$ (left) and $t = 0.7$ (right) using MCL - local bounds with 400×200 mesh, $o = 3$

3.5.1 Qualitative comparison
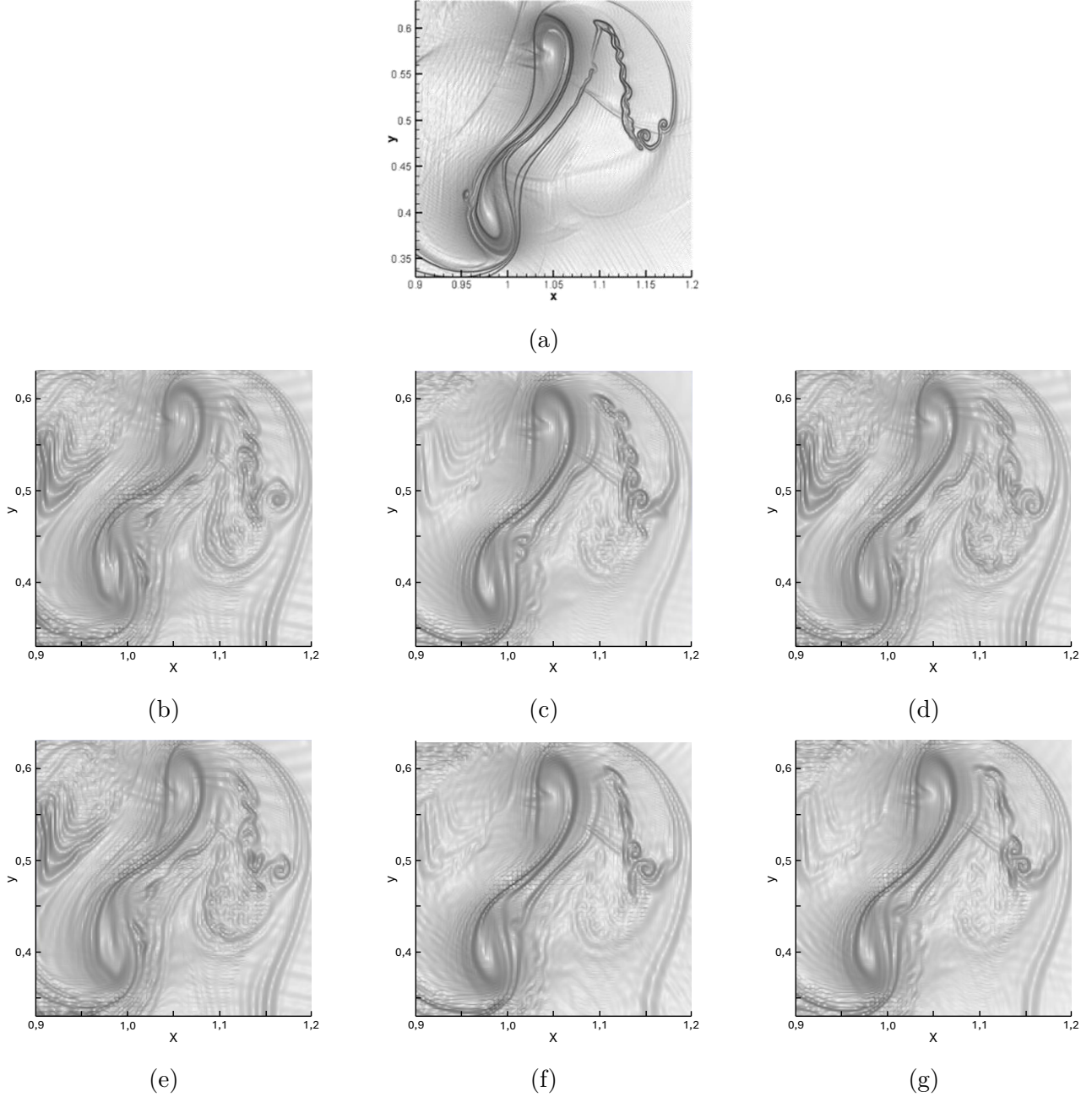
Figure 3.10: Schlieren to compare the vortex at $t = 0.7$ for different method of positivity preserving with 400×200 mesh and $o = 3$. (a) reference, (b) ESDGSEM, (c) APriori, (d) APosteriori, (e) APosteriori Subcell, (f) MCL - local, (g) MCL - global

A first qualitative assessment is provided in Fig. 3.10, which compares the numerical Schlieren images of the vortex. As expected, APosteriori and APosteriori Subcell produce results similar to ESDGSEM, exhibiting noticeable spurious features, whereas APriori and both MCL limiters yield smoother Schlieren fields. The Kelvin-Helmholtz instability on the right is not well pre-

served by ESDGSEM, while the other methods better maintain this feature. Compared to the reference solution, ESDGSEM, APriori, and APosteriori Subcell display more pronounced fluctuations. These fluctuations are evident in the density profile along the line passing through the shock, as shown later. Thus, the diffuse appearance of the KHI can be attributed to these oscillations, destabilising this region. Overall, the main structure of the vortex is reasonably well captured by all methods.

3.5.2 Stability and computational cost

Before proceeding to the quantitative comparison with the reference, a preliminary examination of the maximal time step required for simulation stability is conducted. Tab. 3.5 summarises this time step for each spatial discretization. APriori, APosteriori, and MCL maintain a nearly constant CFL number, as the maximal time step is halved when the grid resolution is doubled in both directions. In contrast, ESDGSEM and APosteriori Subcell require their maximal time step to be reduced by approximately a factor of four with each refinement.

Additionally, the computational cost, shown in Tab. 3.6, is reported relative to ESDGSEM. The subcell-wise methods, APosteriori Subcell and MCL, have a significantly higher computational cost compared to the element-wise methods, APriori and APosteriori.

Grid	ESDGSEM	APriori	APosteriori	APosteriori Subcell	MCL local	MCL global
100×50	1e-3	1.2e-3	1.2e-3	1e-3	1e-3	1e-3
200×100	5e-4	6e-4	6e-4	5e-4	5e-4	5e-4
400×200	1e-5	3e-4	3e-4	1e-4	2.5e-4	2.5e-4

Table 3.5: Maximal time step to ensure stability of different methods for strong vortex-shock interaction simulation Eq. 3.6 with $o = 3$.

Grid Time step	ESDGSEM	APriori	APosteriori	APosteriori Subcell	MCL local	MCL global
400×200 1e-5	1	1.38	1.45	2.01	1.97	2

Table 3.6: Computational cost of different methods for strong vortex-shock interaction simulation Eq. 3.6 with 400×200 grid, $\Delta t = 10^{-5}$ and $o = 3$ on 32 processors provided by Nic5 cluster

All simulations were performed using the minimal time step listed in Tab. 3.5, ensuring consistent grid refinement and temporal resolution between methods.

3.5.3 Quantitive comparison

The first comparison, shown in Fig. 3.11, examines a line passing through both the shock and the vortex. Here, spurious oscillations appear at and beyond the shock for ESDGSEM, APosteriori, and APosteriori Subcell. These two positivity-preserving approaches closely follow ESDGSEM, resulting in similar oscillatory behaviour. In contrast, APriori and MCL dampen these oscillations near the shock, but at the cost of increased dissipation of the vortex structure, APriori follows MCL with global bounds solution. As the mesh is refined, all methods converge toward the reference solution, though oscillations persist after the shock for ESDGSEM, APosteriori, and APosteriori Subcell.
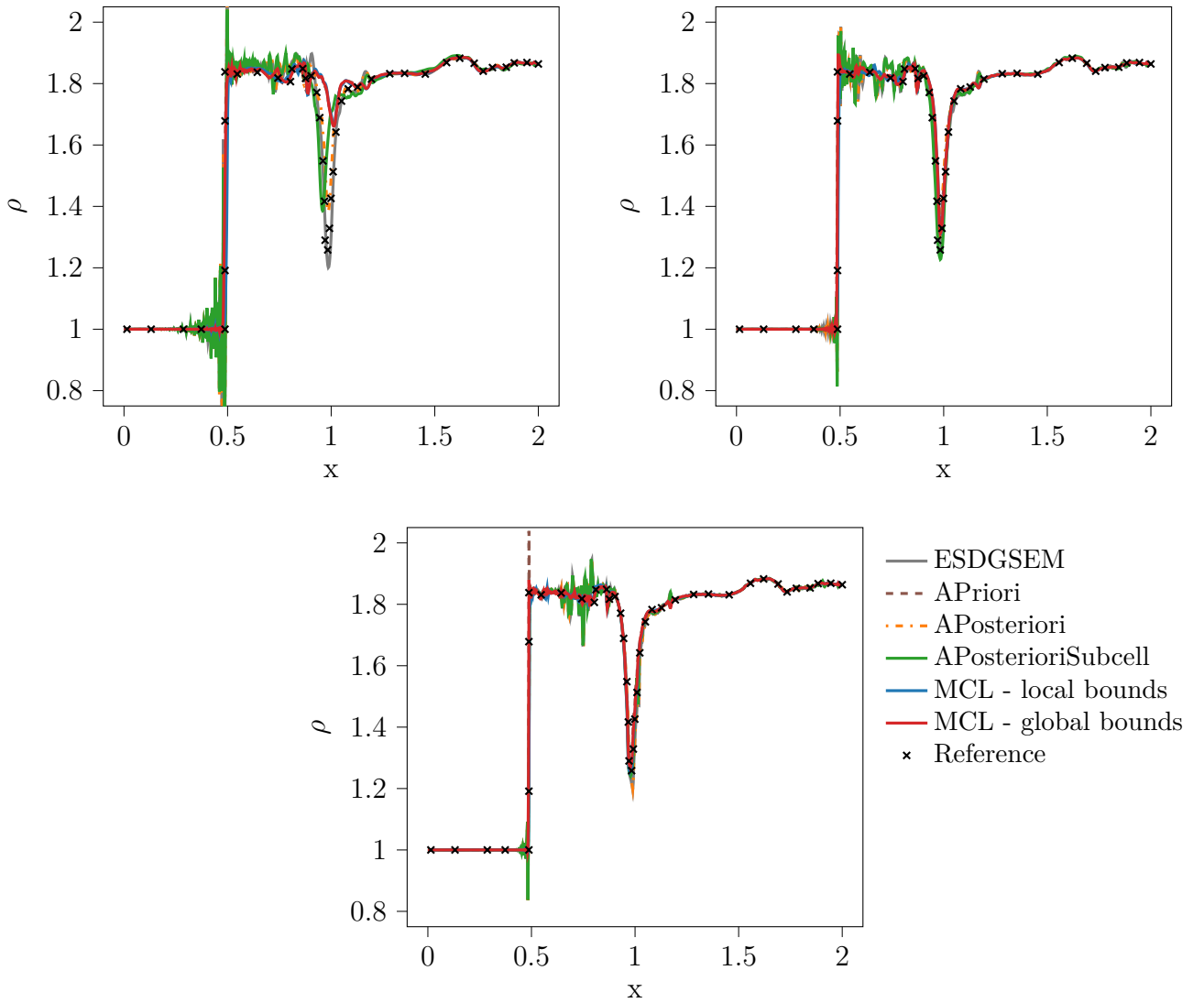

Figure 3.11: Density of line 1 at $y = 0.4 + \epsilon$ and $t = 0.7$. Comparison of methods using the strong vortex-shock interaction simulation, Eq. 3.6, $o = 3$. Top left: 100×50 cells, top right: 200×100 cells, bottom: 400×200 cells.

A closer examination of the shock region in Fig. 3.12 reveals the detailed behaviour of each method regarding spurious oscillations. Pronounced oscillations appear both upstream and downstream of the shock with ESDGSEM, and similar non physical oscillations are present for APosteriori and APosteriori Subcell, reflecting the behaviour of the DG scheme. As the mesh is refined, these oscillations are somewhat reduced, but persist as localised undershoots, particularly before the shock. In contrast, the APriori and MCL methods demonstrate a clear advantage in suppressing these oscillations. MCL with local bounds removes the extrema and nearly eliminates both overshoots and undershoots, while MCL with global bounds and APriori still allow minor residual oscillations, particularly at higher resolutions. Notably, APriori tends to follow the behaviour of MCL global bounds, producing an overshoot on the finest mesh.

Figure 3.12: Zoom on density line 1 at $y = 0.4 + \epsilon$ and $t = 0.7$ in shock region. Comparison of methods using the strong vortex-shock interaction simulation, Eq. 3.6, $o = 3$. Top left: 100×50 cells, top right: 200×100 cells, bottom: 400×200 cells.

Following the analysis of the shock region, the vortex portion of the line is considered in Fig. 3.13. In this region, APriori and MCL significantly under-resolve the vortex on the coarser mesh, while the other methods provide a more accurate representation at lower resolutions. On the finest mesh, ESDGSEM, APosteriori, and APosteriori Subcell exhibit some non-physical oscillations on the left. The increased numerical dissipation of APriori and MCL leads to a less accurate vortex representation, but this also results in smoother shock regions. An odd behaviour is also observed on the finest mesh for ESDGSEM and APosteriori methods, the vortex is not well captured, and oscillations can be observed inside the vortex, probably linked with the oscillations observed on the left.
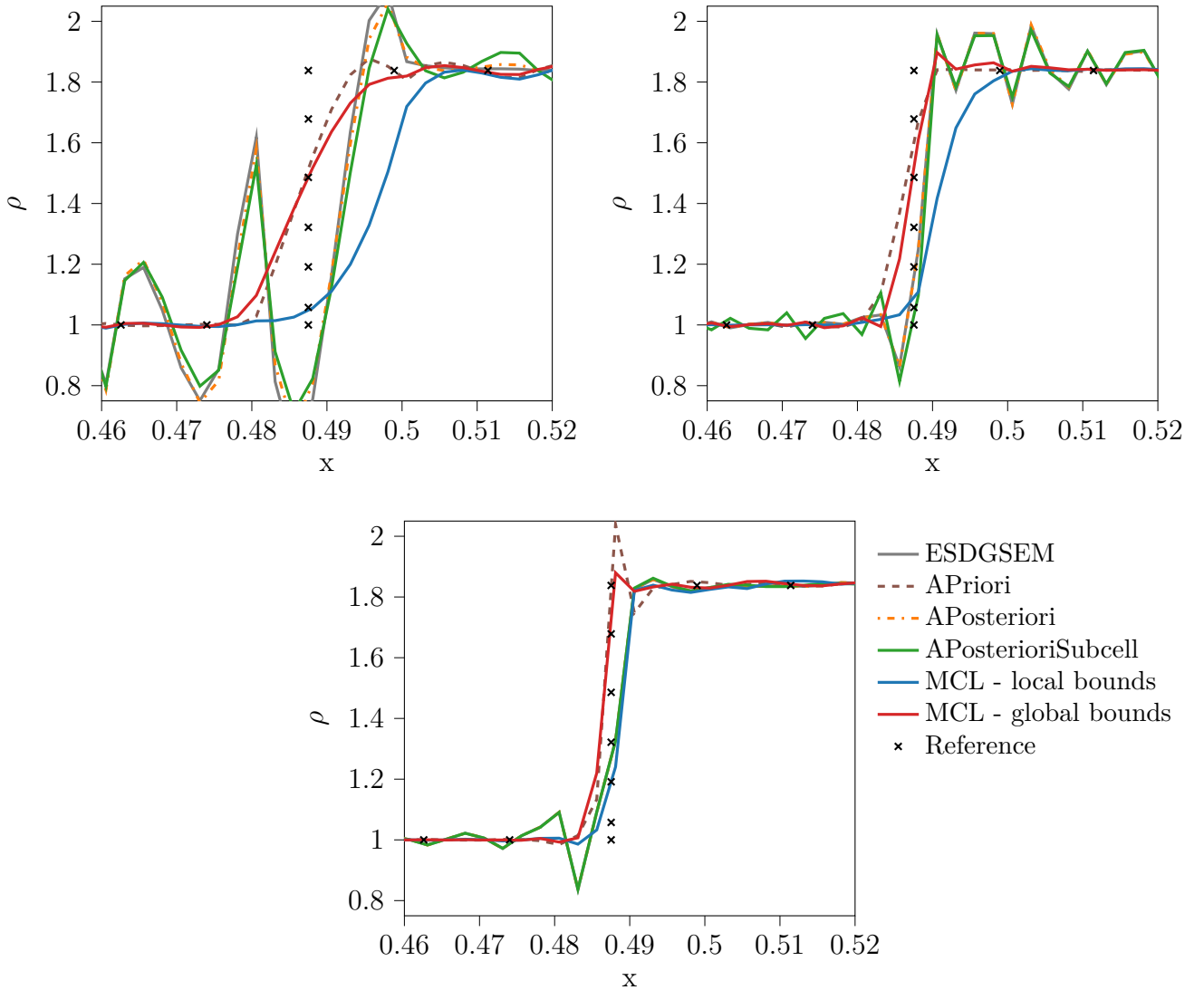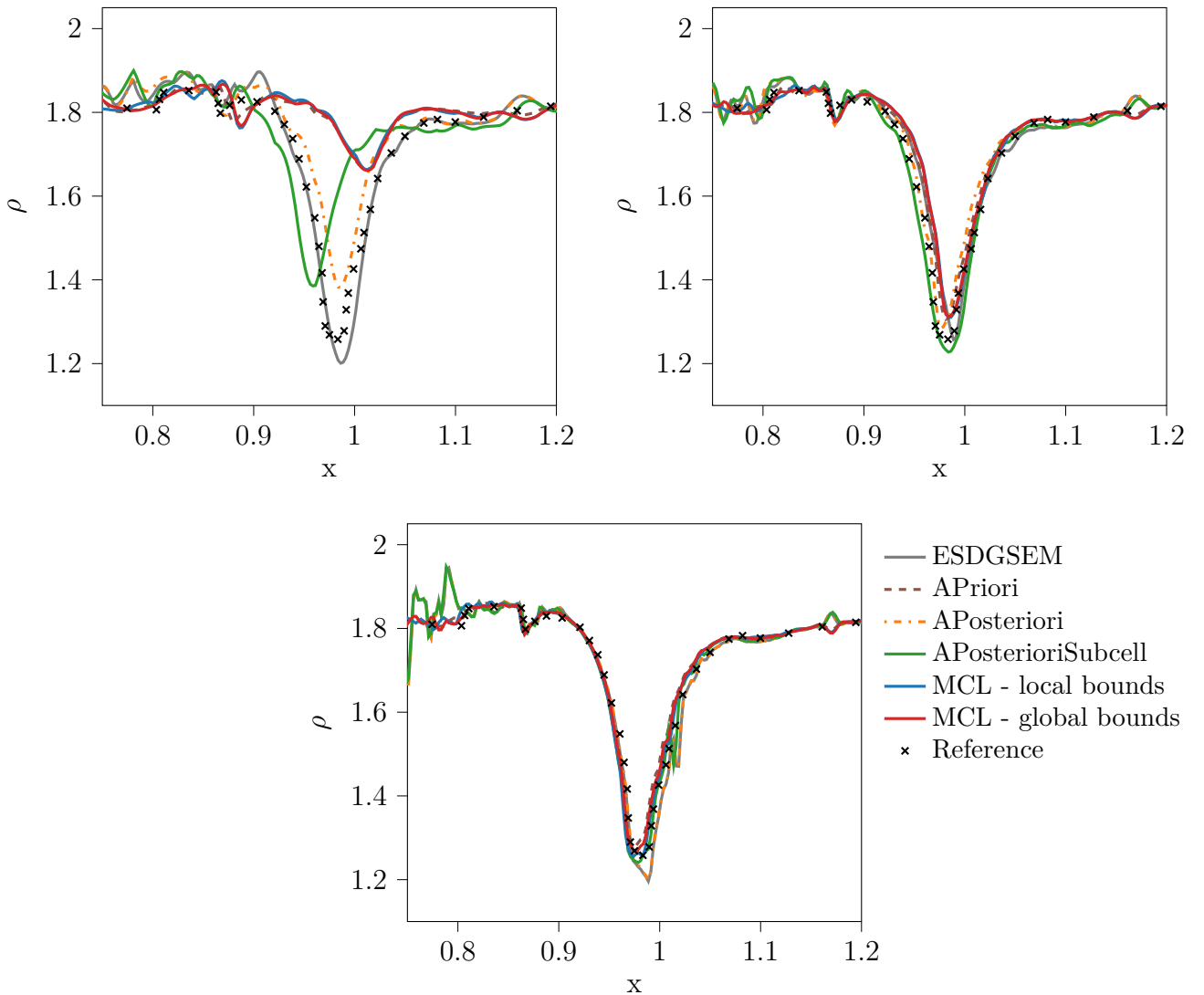

Figure 3.13: Zoom on density line 1 at $y = 0.4 + \epsilon$ and $t = 0.7$ in vortex region. Comparison of methods using the strong vortex-shock interaction simulation, Eq. 3.6, $o = 3$. Top left: 100×50 cells, top right: 200×100 cells, bottom: 400×200 cells.

The second line, which passes exclusively through the vortex, provides further quantitative

analysis to assess the performance of each method. As shown in Fig. 3.14, ESDGSEM and APosteriori methods capture the vortex structure more accurately on coarser meshes, closely following the reference solution in terms of amplitude and shape. However, as the mesh is refined, all the methods converge toward the reference.

Notably, on the finest mesh, ESDGSEM exhibits a slight loss of accuracy, similarly to APosteriori. The rest of the methods better capture the vortex structure on the finest mesh. In contrast, APriori and both MCL variants demonstrate increased dissipation on coarse grids, leading to an under-resolved vortex. Nevertheless, as the spatial resolution increases, these methods progressively recover the reference solution.
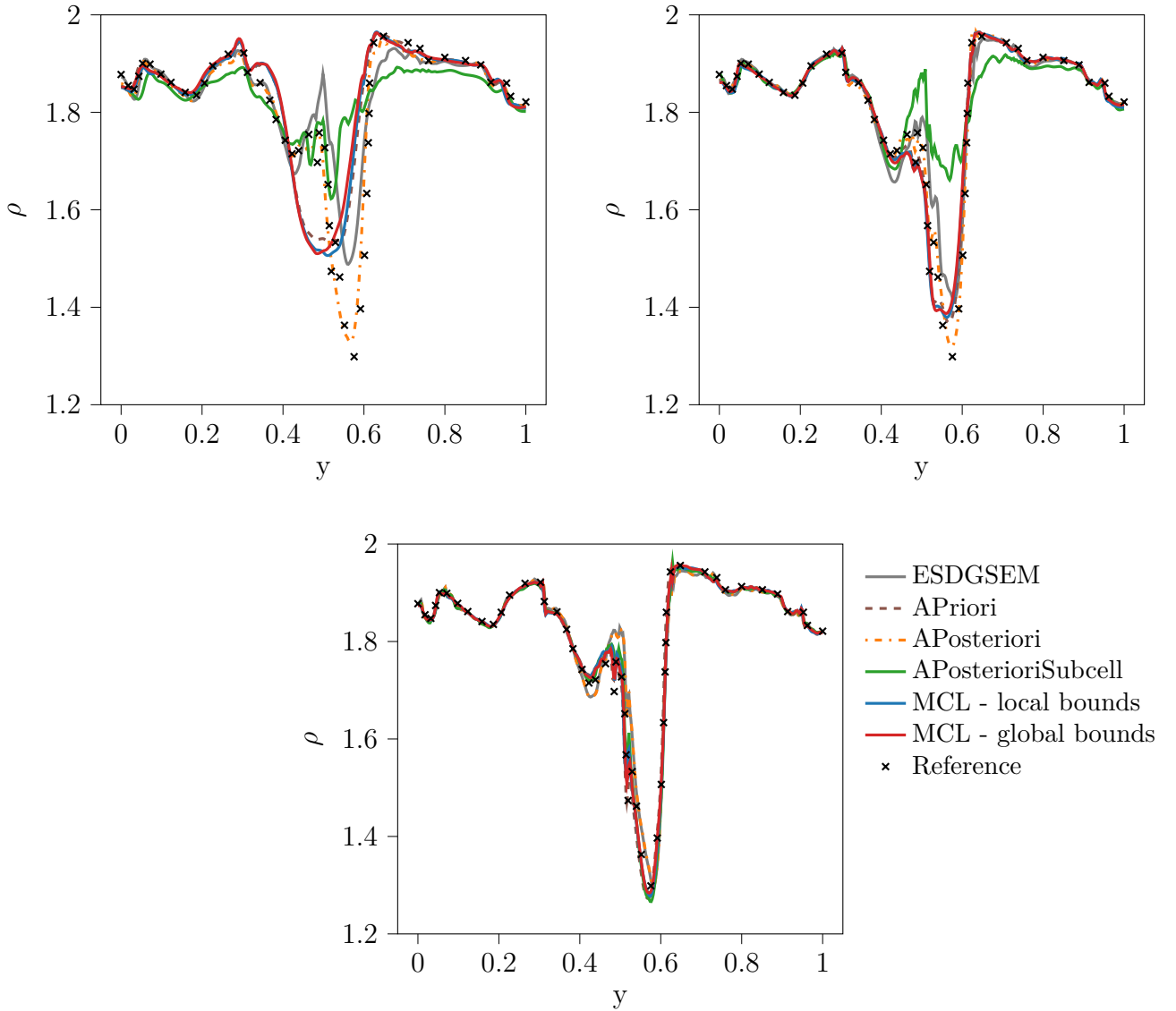

Figure 3.14: Density of line 2 at $x = 1.5 + \epsilon$ and $t = 0.7$. Comparison of methods using the strong vortex-shock interaction simulation, Eq. 3.6, $o = 3$. Top left: 100×50 cells, top right: 200×100 cells, bottom: 400×200 cells.

Overall, this comparison highlights a trade-off: ESDGSEM and APosteriori provide better vortex resolution on coarse meshes but provide spurious oscillations near shocks, while APriori and MCL offer reduced oscillations at the expense of increased dissipation, especially at lower resolutions. As the mesh is refined, all approaches converge and the impact of the chosen limiting strategy becomes less pronounced. However, the computational cost of the methods varies significantly, with APriori and APosteriori being more efficient than the subcell-wise methods, APosteriori Subcell and MCL.
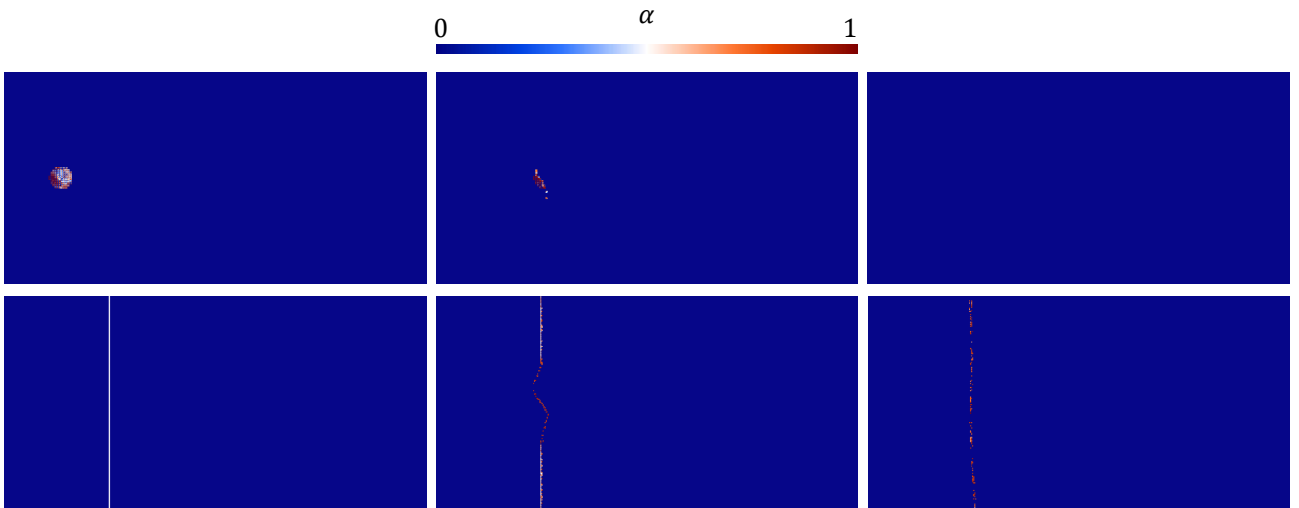
3.5.4 Blending coefficient

Figure 3.15: Blending coefficient for strong vortex-shock interaction at $t = 0$ (left), $t = 0.15$ (middle) and $t = 0.7$ (right) using APosteriori Subcell (top) and MCL - global bounds (bottom).

By analysing the blending coefficient one can observe that the Lower Bound criterion flags only the cells containing the vortex before it interacts with the shock. Since the threshold is set below the density of the shock, only the vortex region is detected and stabilised by APosteriori and APosteriori Subcell. Once the vortex passes through the shock, no further troubled cells are identified, and the scheme is reverted to ESDGSEM. This explains the close agreement among ESDGSEM, APosteriori, and APosteriori Subcell solutions, as the limiting is only active in the vortex region before the shock interaction, observed in Fig. 3.11 or Fig. 3.14.

Conversely, the Regularity criteria only detects the shock throughout the simulation, as evidenced by the persistent identification of troubled cells along the shock front. The passage of the vortex through the shock leads to a distortion of the shock structure, which is captured by the sensor. This results in less oscillation solutions observed with APriori and MCL. However, this approach also results in greater dissipation of the vortex, as these methods are applied

more extensively, leading to solutions that are less accurate in the vortex region compared to those based on ESDGSEM, especially for coarser mesh.

This behaviour is further illustrated by the evolution of the proportion of troubled cells during the simulation, as shown in Fig. 3.16. In contrast, APriori maintains the highest proportion of troubled cells, yet its results remain very similar to those of MCL, which achieves comparable accuracy with fewer troubled cells. This suggests that APriori is less dissipative per troubled cell compared to MCL.
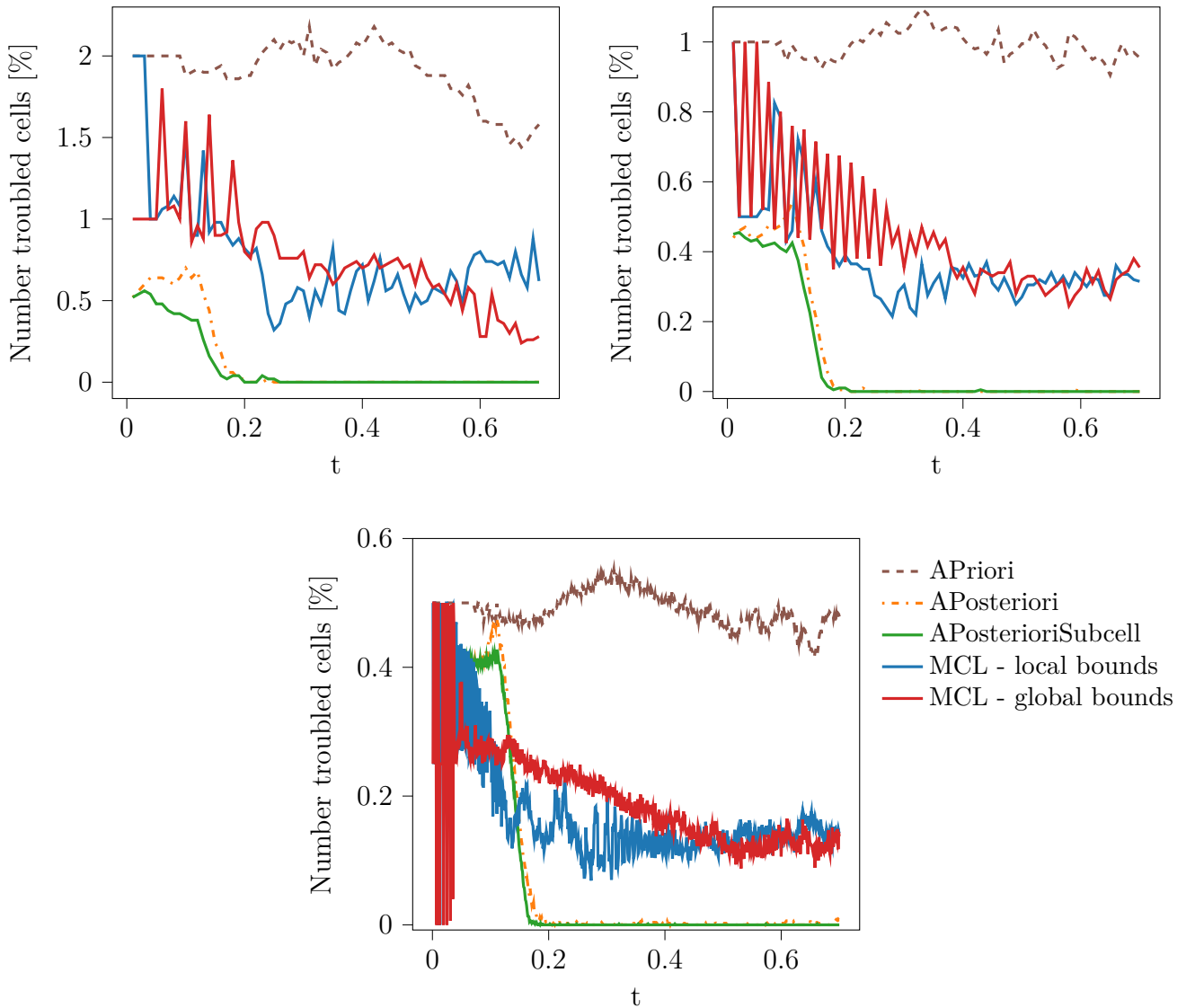

Figure 3.16: Proportion of troubled cells on the domain along time. Comparison of methods using the strong vortex-shock interaction simulation, Eq. 3.6, $o = 3$. Top left: 100×50 cells, top right: 200×100 cells, bottom: 400×200 cells.

3.6 Daru-Tenaud shock tube

The Daru-Tenaud shock tube [13] is a two-dimensional viscous flow test case that describes the evolution of a shock wave with several interactions, such as the shock-boundary layer. A diaphragm is located at $x_0 = 0.5$ at $t = 0$s, separating a high pressure and density from a low pressure section. The initial conditions are given by

$$\rho_0(x,y) = \begin{cases} 120 & \text{if } x \leq x_0 \\ 1.2 \end{cases} \qquad \vec{v}_0(x,y) = \begin{pmatrix} 0 \\ 0 \end{pmatrix} \qquad p_0(x,y) = \begin{cases} \rho_L/\gamma & \text{if } x \leq x_0 \\ \rho_R/\gamma \end{cases} \tag{3.8}$$

where $\gamma = 1.4$ and $\Omega = [0,1] \times [0,0.5]$, solid walls boundaries with no-slip conditions are applied on the domain. The Reynolds number is set to $Re = 1000$, which promotes the formation of small-scale vortices and increases the complexity of the simulation. Once the diaphragm is removed, a shock wave with Mach number 2.37 propagates into the low-pressure region, followed by a contact discontinuity. A rarefaction wave travels in the opposite direction. A boundary layer develops along the lower wall and interacts with the shock. When the shock reflects off the right wall, its interaction with the boundary layer produces the characteristic lambda-shaped shock seen in Fig. 3.17. A Kelvin-Helmholtz instability also appears above the main vortex, ending in a smaller vortex in the right corner. The reference solution uses the OSMP7 scheme on a 4000×2000 grid, provided by Virginie Daru and Christian Tenaud [13]. A density profile at $y = 0.05$, within the boundary layer and the bubble separating, is used to assess the error of the different methods. Similarly to KHI test cases, ESDGSEM alone is unstable, highlighting the necessity of stabilisation methods.
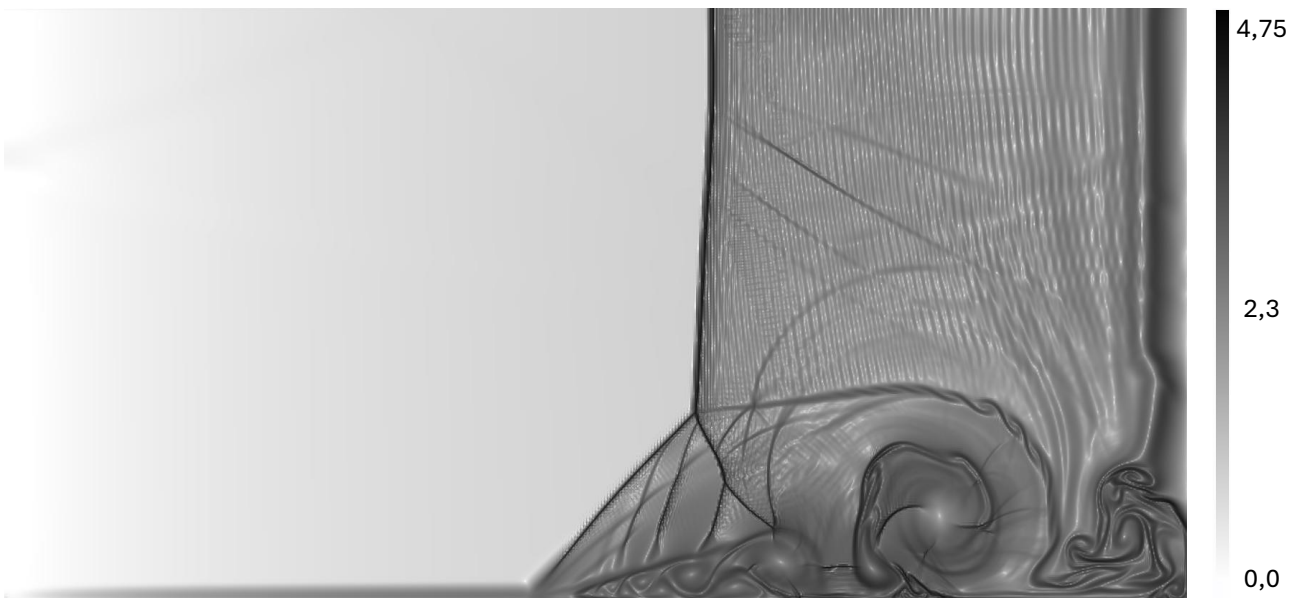

Figure 3.17: Numerical Schlieren of Daru-Tenaud, Eq. 3.8 at $t = 1$ for $Re = 1000$ using MCL - global bounds with 400×200 cells, $o = 3$

3.6.1 Qualitive comparison
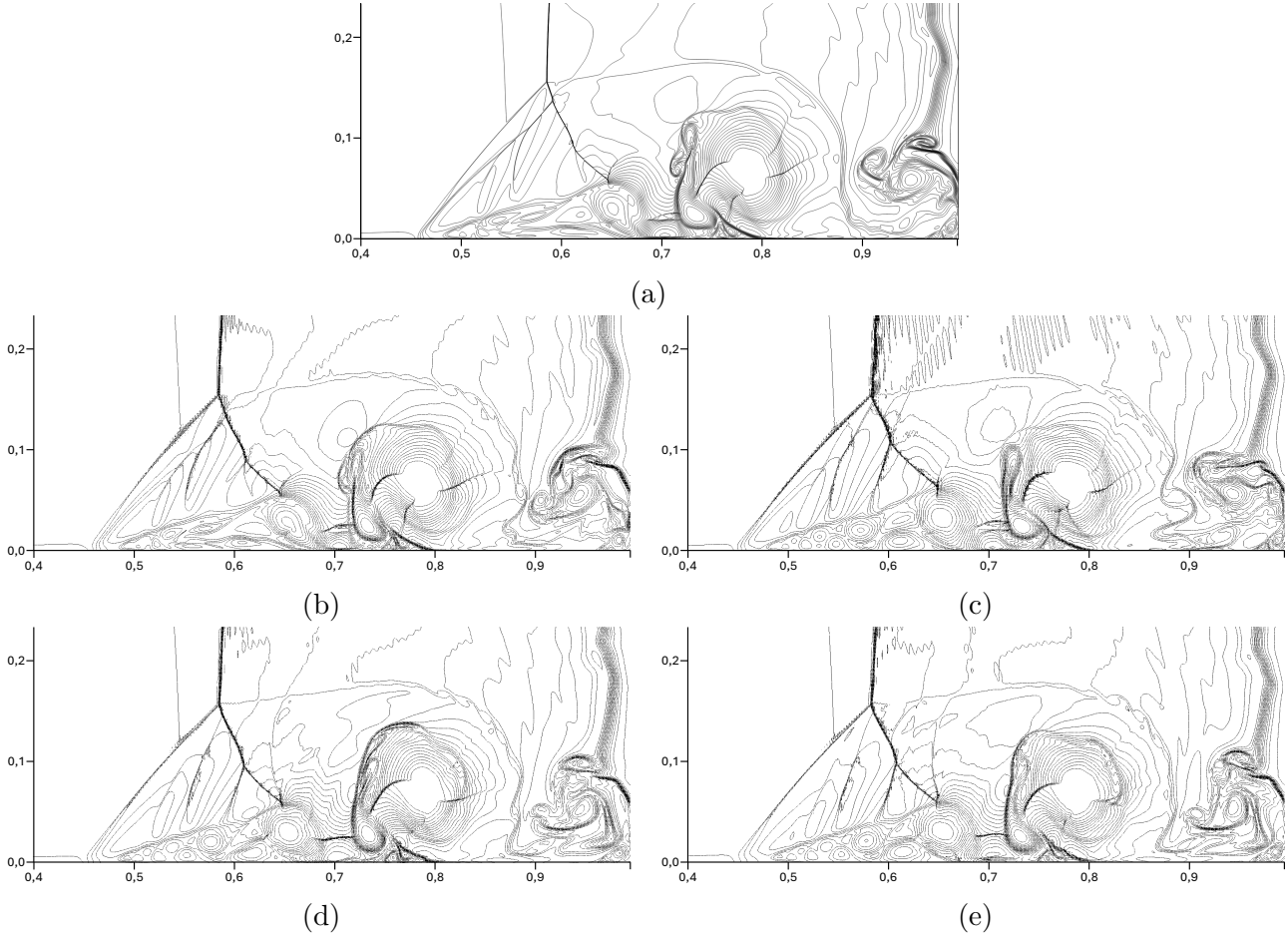
Figure 3.18: Density contours (21 levels between 20 and 120) at $t = 1$ for $Re = 1000$ using MCL local and global bounds with 400×200 mesh and $o = 3$. (a) reference (4000×2000), (b) APriori, (c) APosteriori Subcell, (d) MCL - local bounds, (e) MCL - global bounds

Similarly to the strong vortex shock interaction case, a qualitative assessment of the various methods is initially conducted by comparing their density contour plots with the reference solution in Fig. 3.18. APosteriori is omitted from this comparison due to instability, as the method remains very close to ESDGSEM, it could be an explication of its instability, as discussed later in Tab. 3.7. Among the methods, APriori appears to provide the most accurate results on the finer mesh, capturing more flow features and converging more rapidly to the reference solution. The large central vortex, composed of smaller vortices on the left, is well resolved by APriori, which accurately captures the various small shocks present within it. The Kelvin-Helmholtz instability above this vortex tends to vanish in the reference solution with a very fine mesh. In the right corner, the vortex generated by the contact discontinuity is not well captured by APriori and MCL, whereas APosteriori Subcell resolves this feature more effectively. In fact, this vortex does not require stabilisation, as a contact discontinuity is not a shock. As shown

later, the troubled cell detector is not activated in this region; however, the use of these methods introduces some dissipation, which in turn modifies the flow. On the left, the lambda-shaped shock is well defined by all methods, but the secondary oblique shock seen in the reference is only resolved by APriori. Additionally, the structure under the shock is well captured by APriori, whereas the other methods retain larger vortices that appear to merge in the reference solution. Once again, several oscillations are observed in the APosteriori Subcell solution.

3.6.2 Stability and computational cost

Grid	ESDGSEM	APriori	APosteriori	APosteriori Subcell	MCL local	MCL global
100×50	✗	2e-4	2e-4	2e-4	2e-4	2e-4
200×100	✗	5e-5	1.25e-5	5e-5	5e-5	5e-5
400×200	✗	1.25e-5	✗	1.25e-5	1.25e-5	1.25e-5

Table 3.7: Maximal time step to ensure stability of different methods for Daru-Tenaud simulation Eq. 3.8 $o = 3$ and $Re = 1000$. ✗ means no time step found to stabilize the simulation

Grid Time step	ESDGSEM	APriori	APosteriori	APosteriori Subcell	MCL local	MCL global
400×200 1.25e-5	✗	1	✗	1.3	1.28	1.29

Table 3.8: Computational cost (taking APriori as reference) of different methods for Daru-Tenaud simulation Eq. 3.8 $o = 3$ and $Re = 1000$. ✗ means no time step found to stabilize the simulation

The temporal stability of this test case is summarised in Tab. 3.7. ESDGSEM alone is unstable for all discretizations, which may also explain the instability of APosteriori, as it remains close to ESDGSEM with the Lower Bound criterion. All other methods yield the same maximal time step and show similar behaviour as the mesh is refined, offering no advantage in allowable time step. Furthermore, a parabolic constraint on the time step is observed, as it is divided by four between each meshes.

Regarding computational cost, APriori is used as the reference, since ESDGSEM is unstable. MCL and APosteriori Subcell are more expensive because of their subcell-wise approach, consistent with previous observations.

3.6.3   Quantitive comparison
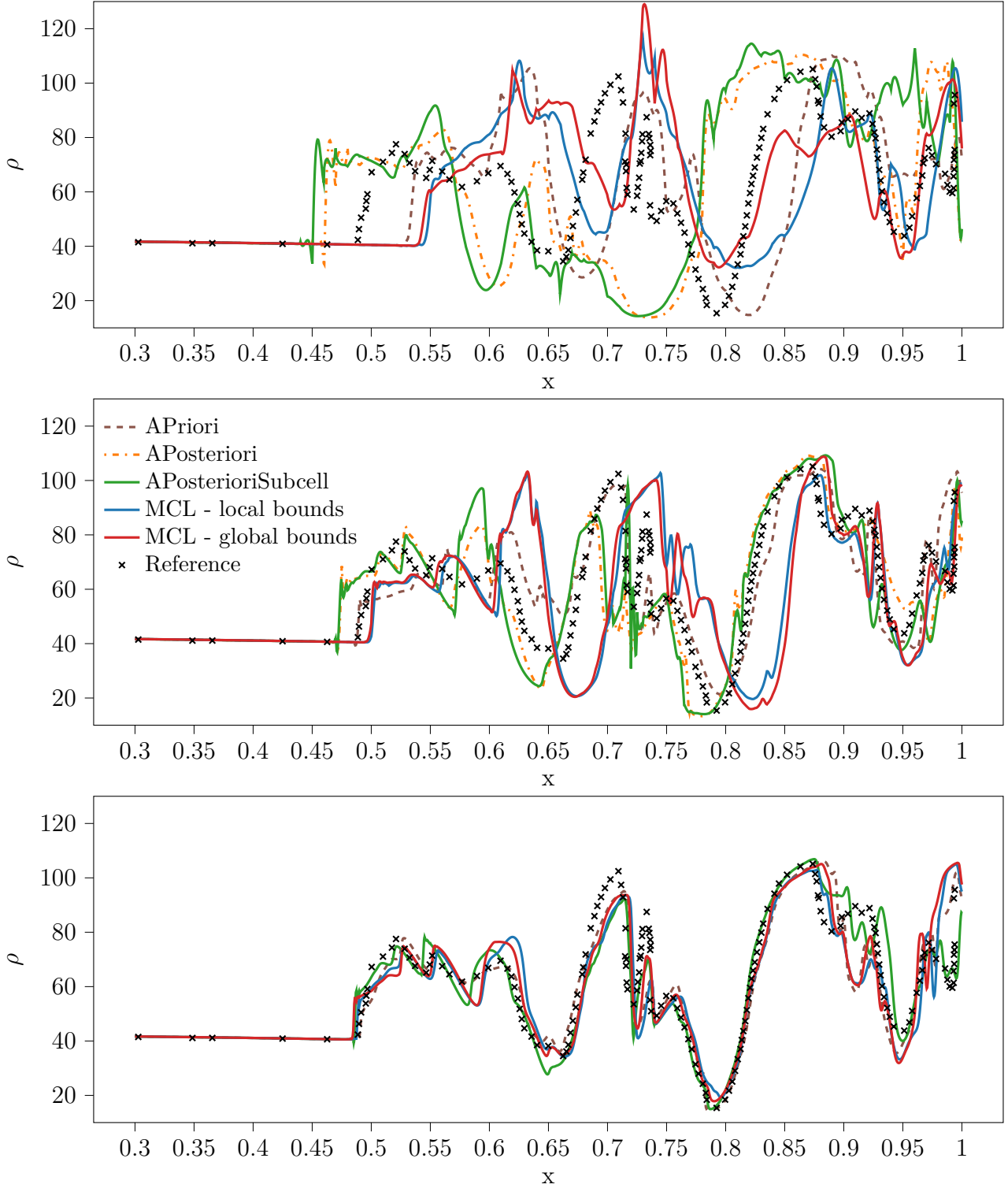
Figure 3.19: Density line at $y = 0.05$ along x at $t = 1$. Comparison of methods for Daru-Tenaud simulation Eq. 3.8 $o = 3$ and $Re = 1000$. . Top : 100×50 cells, middle: 200×100 cells, bottom: 400×200 cells.

A quantitative comparison is carried out using the reference density profile at $y = 0.05$ in Fig. 3.19. On the coarsest mesh, all methods produce highly irregular solutions far from the reference. As the mesh is refined, the results of each method approach the reference profile. In particular, APriori accurately captures the shock position even on the intermediate mesh and closely tracks the reference solution. Both APosteriori and APosteriori Subcell show some oscillations, especially near the first shock, but still align with the reference near the tube's end. MCL exhibits a slight shift in shock location on the intermediate grid, which is resolved as the mesh is refined. On the finest grid, APosteriori becomes unstable and, therefore, no solutions are computed. Minor spurious oscillations persist with APosteriori Subcell at the first shock, due to the close relation with ESDGSEM. Overall, these results highlight the importance of stabilisation techniques for accurate and stable solutions in this challenging test case

3.6.4 Blending coefficient
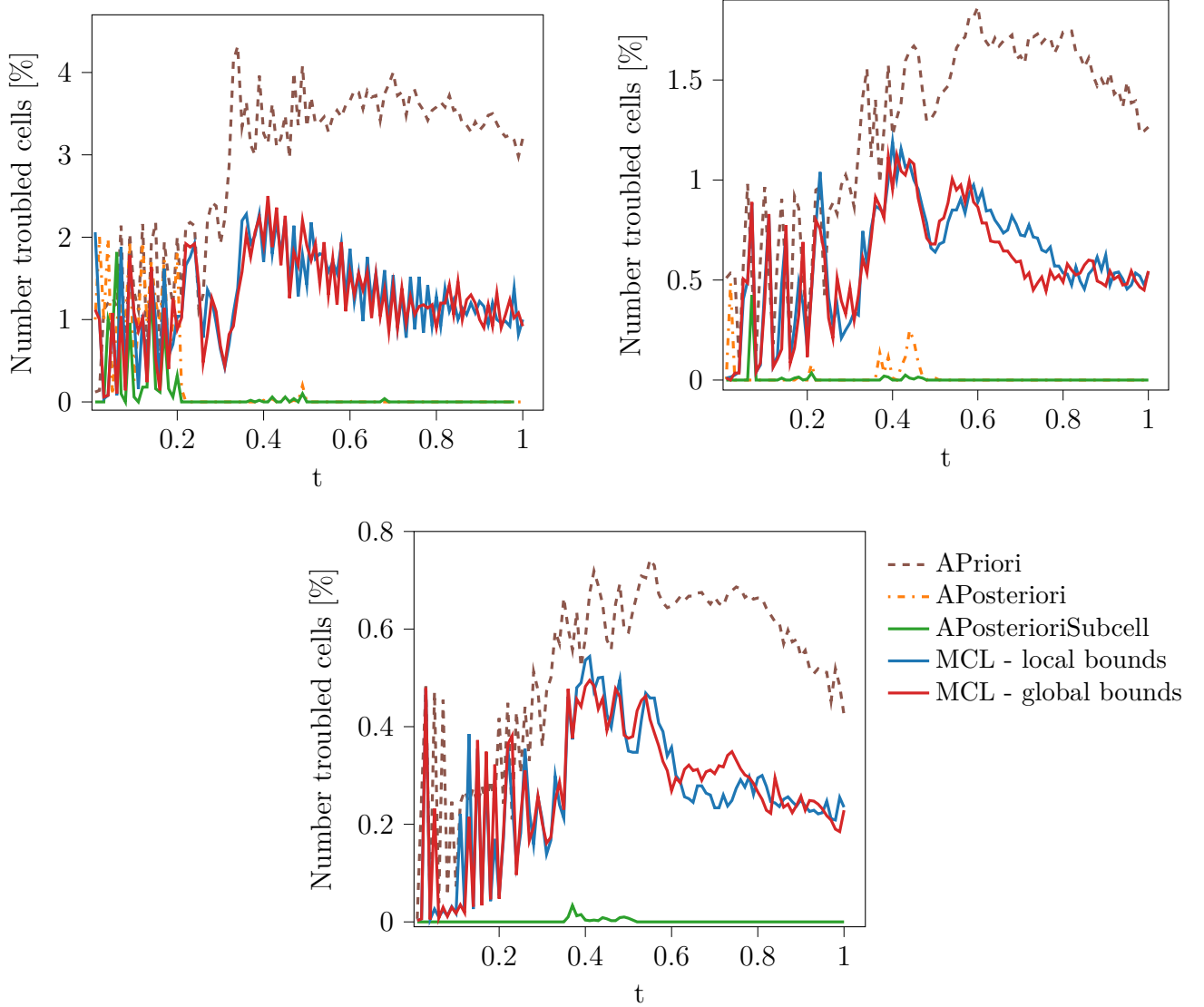
Figure 3.20: Proportion of troubled cells in the domain along the simulation. Comparison of methods for Daru-Tenaud simulation Eq. 3.8 $o = 3$ and $Re = 1000$. . Top : 100×50 cells, middle: 200×100 cells, bottom: 400×200 cells.

The proportion of troubled cells in the domain is shown in Fig. 3.20. The MCL methods occupy an intermediate position, with a moderate number of troubled cells compared to the APriori and APosterioriSubcell variants. This behaviour suggests that MCL introduces more dissipation, which helps to suppress the development of problematic structures before they can destabilise the simulation. As a result, MCL is more robust but may sacrifice some accuracy in capturing fine-scale features, as evidenced by the slightly smoother density profiles and contours.
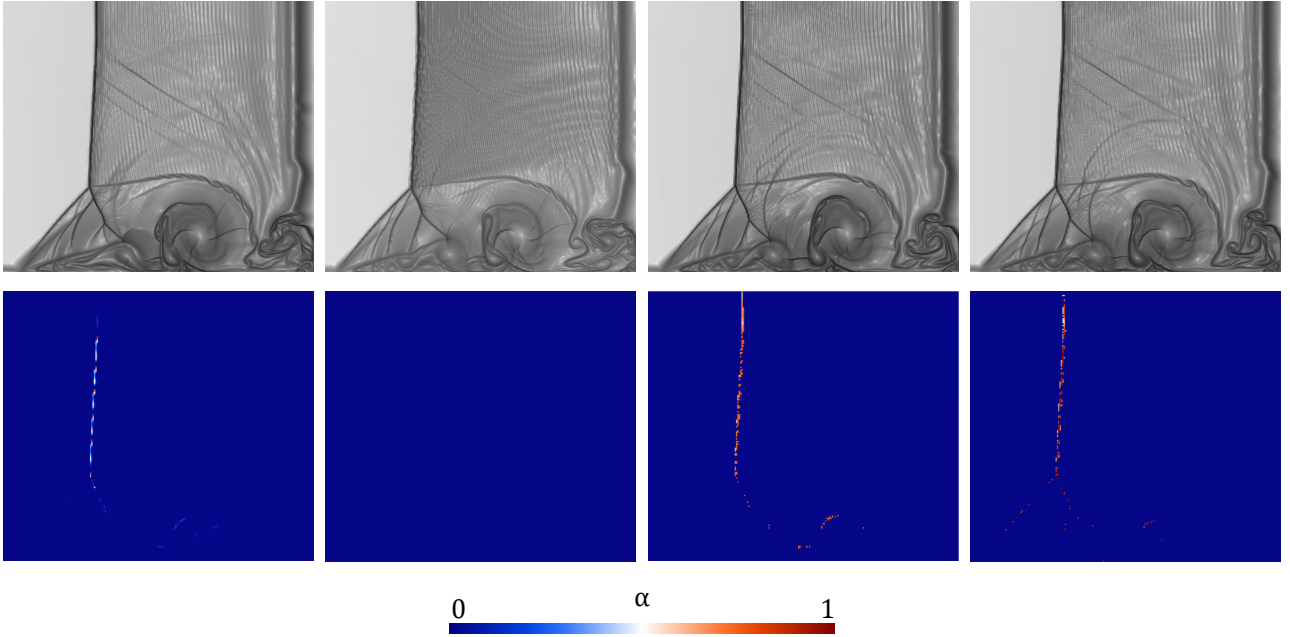
Figure 3.21: Schlieren and blending coefficient at $t = 1$. Comparison of methods using the Daru-Tenaud simulation Eq. 3.8 for 400×200 cells and $o = 3$. From left to right: APriori, APosterioriSubcell, MCL - local bounds and MCL - global bounds (APosteriori is unstable).

Fig. 3.21 show that methods based on regularity criteria (APriori and MCL) show blending coefficients concentrated around key flow features, such as shocks and vortices. As discussed earlier, stabilisation is not required in the right corner vortex, which corresponds to a contact discontinuity. APriori maintains a low limiting factor, resulting in less dissipation and enabling the solution to capture more flow features. At this stage of the simulation, APosteriori Subcell does not exhibit any blending coefficient. MCL with local bounds produces a higher blending coefficient, as expected, since it prevents the creation of new extrema and applies stricter stabilisation. MCL with global bounds behaves similarly to the local bounds approach in this case.

3.7 Taylor-Green vortex

Taylor-Green vortex (TGV) [9, 54] is a tree-dimensional viscous test case. The initial conditions are

$$\rho_0(x,y,z) = \frac{p}{RT} \qquad p_0(x,y,z) = p_0 + \frac{\rho_0 V_0^2}{16}\left(\cos\left(\frac{2x}{L}\right) + \cos\left(\frac{2y}{L}\right)\right)\left(\cos\left(\frac{2z}{L}\right) + 2\right) \qquad (3.9)$$

$$\vec{v}_0(x,y,z) = \begin{pmatrix} V_0 \sin\left(\frac{x}{L}\right)\cos\left(\frac{y}{L}\right)\cos\left(\frac{z}{L}\right) \\ V_0 \cos\left(\frac{x}{L}\right)\sin\left(\frac{y}{L}\right)\cos\left(\frac{z}{L}\right) \\ 0 \end{pmatrix}$$

where $\Omega = [-L\pi, L\pi]^3$ with periodic boundary conditions and $\gamma = 1.4$. The characteristic length scale is $L = 1$, and the velocity is given by $V_0 = a_0 M_0$, where $a_0 = \sqrt{\gamma R T_0}$ is the speed of sound and M_0 is the imposed Mach number. The initial temperature is $T_0 = \frac{p_0}{\rho_0 R}$, with the initial density $\rho_0 = 1$ and the initial pressure $p_0 = \frac{\rho_0 V_0^2}{\gamma M_0^2}$, ensuring $T_0(x,y,z) = T_0$. The Prandtl number is $Pr = 0.71$, and the Reynolds number is $Re = \frac{\rho_0 V_0 L}{\mu_0} = 1600$. The dynamic viscosity is described by Sutherland's law [51]

$$\mu(T) = \mu_0 \left(\frac{T}{T_0}\right)^{3/2} \frac{T_0 + S}{T + S} \text{ with } S = 0.4042 \qquad (3.10)$$

Chapelier [9] provides a reference solution using a sixth-order TENO scheme with 2048^3 degrees of freedom. This benchmark is widely used to evaluate the dissipation properties of CFD methods due to the presence of shocklets and significant compressive effects, which make simulation particularly challenging. The initial Mach number $M_0 = 1.25$ leads to Mach waves that reach $M = 2$ at $t/\tau = 6$. To assess the dissipation characteristics of the methods, both solenoidal and dilatational dissipation are compared with the reference solution. Additionally, the Mach line at $t/\tau = 2.5$, when dilatational dissipation peaks, is compared to the reference to evaluate shock-capturing capabilities. For these comparisons, time is non-dimensionalized using the convective time $\tau = L/V_0 = L/(a_0 M_0)$. All quantities are computed on three different meshes: 64^3, 128^3, and 256^3 degrees of freedom.

3.7.1 Stability and computational cost

First, let's take a look at the maximal times step of the different methods. As shown in Tab. 3.9, the maximal time step to ensure stability is the same for all methods.

Tab. 3.10 compares the computational cost of each method for a 64^3 grid and a time step of 1e-3. ESDGSEM is used as the reference with a normalised cost of 1. The APriori method is the least expensive, requiring 1.23 times the cost of ESDGSEM. APosteriori and APosteriori

Subcell methods are significantly more expensive, with costs of 2.56 and 3.04 times those of ESDGSEM, respectively. This increased cost is unexpected and may be due to the three-dimensional domain used in this test case. To detect the troubled cells, the Lower Bound criteria requires the computation of the density and pressure on each interpolation points, compared to the Regularity criteria who only compute a single value for the whole element. Using an order of $o = 3$, the number of interpolation points within a three-dimensional element is $(o + 1)^3 = 64$ compared to $(o + 1)^2 = 16$ in a two-dimensional element. This could be the reason for the cost increase. The MCL local and global methods have costs of 1.49 and 1.46 times that of ESDGSEM, respectively, which are close to the APriori method. Overall, subcell methods are the most expensive as they compute a blending coefficient at each interpolation point, whereas the other methods compute it only for the whole cell.

Grid	ESDGSEM	APriori	APosteriori	APosteriori Subcell	MCL local	MCL global
16^3	4e-3	4e-3	4e-3	4e-3	4e-3	4e-3
32^3	2e-3	2e-3	2e-3	2e-3	2e-3	2e-3
64^3	1e-3	1e-3	1e-3	1e-3	1e-3	1e-3

Table 3.9: Maximal time step to ensure stability of different methods for Taylor-Green vortex simulation Eq. 3.9 with $o = 3$.

Grid Time step	ESDGSEM	APriori	APosteriori	APosteriori Subcell	MCL local	MCL global
64^3 1e-3	1	1.23	2.56	3.04	1.49	1.46

Table 3.10: Computational cost of different methods for Taylor-Green vortex simulation Eq. 3.9 with 64^3 grid, $\Delta t = 10^{-3}$ and $o = 3$ on 32 processors provided by Nic5 cluster

3.7.2 Quantitive comparison

Examining the Mach line at $x = 0$ and $z = 0$ and focussing on the shock region in Fig. 3.22, the performance of the different methods can be compared. ESDGSEM exhibits spurious oscillations before and after the shock, with an undershoot appearing before the shock on the finest mesh. Both the APosteriori and APosteriori Subcell methods behave similarly, producing results that closely match ESDGSEM. Other methods significantly reduce these oscillations. APriori and MCL global bounds yield comparable results, although APriori shows an overshoot on the finest grid. In contrast, on the coarser mesh, MCL local bounds do not accurately capture the upstream flow compared to the other limiting techniques. However, the ability to suppress oscillations has some drawbacks, as seen in the solenoidal and dilatational dissipation results.
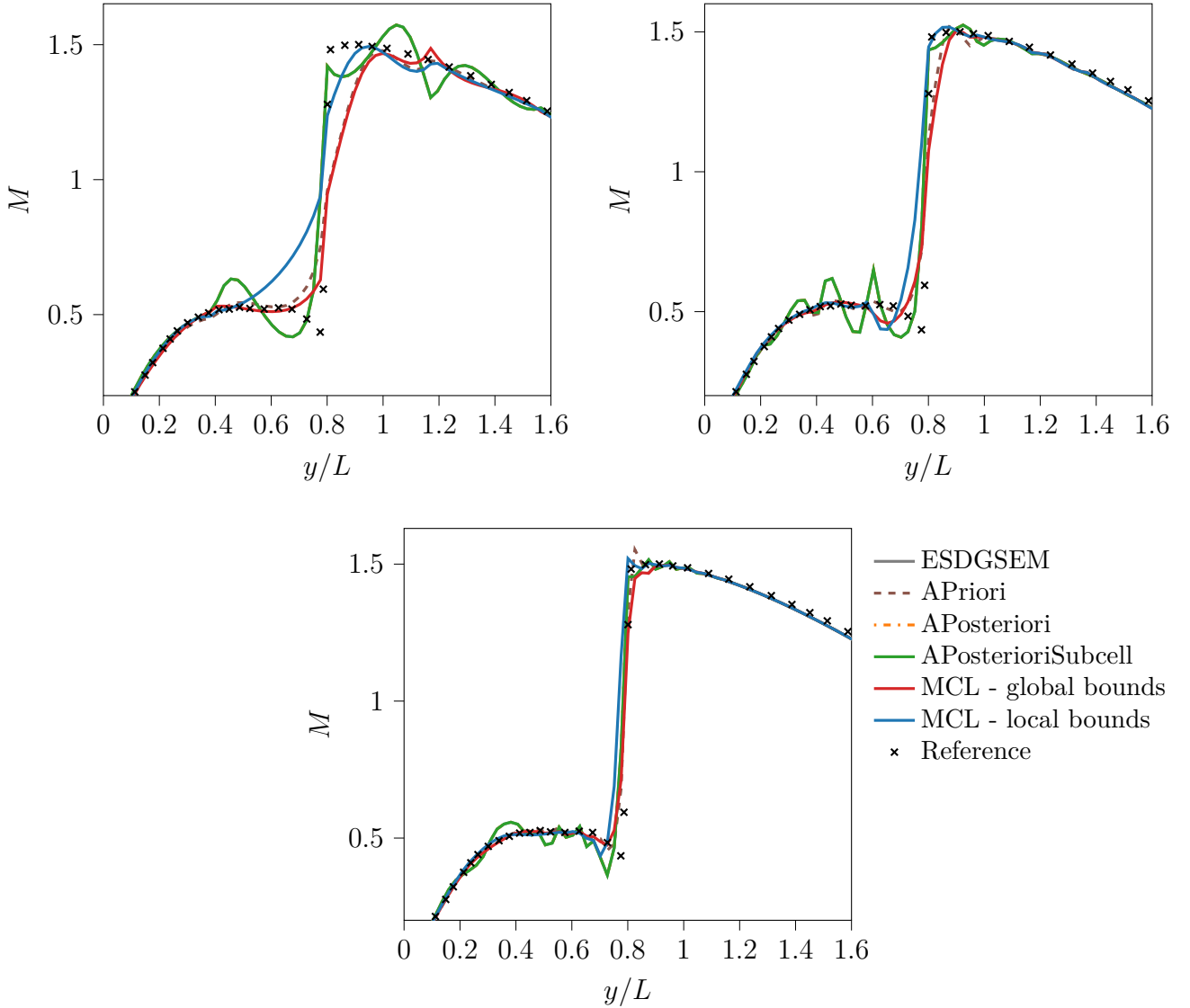
Figure 3.22: Mach line along y for $x = 0$ and $z = 0$ at $t/\tau = 2.5$. Comparison of methods using the Taylor-Green vortex simulation, $M = 1.25$ and $Re = 1600$ with $o = 3$ Eq. 3.9. Top left: 64^3 dof, top right: 128^3 dof, bottom: 256^3 dof.

Fig. 3.23 presents the solenoidal dissipation for each method compared to the reference. All methods show convergence toward the reference solution, with the exception of MCL, which remains further from the reference than APriori. Solenoidal dissipation is governed by small-scale vortices, as it is directly related to enstrophy, which measures the intensity of rotational motion; thus, accurately capturing these structures is important. ESDGSEM provides results closest to the reference, effectively resolving the small-scale features responsible for solenoidal dissipation. The APosteriori and APosteriori Subcell methods perform similarly, closely matching ESDGSEM. Using the Lower Bound sensor, a very low proportion of troubled cells are detected and therefore remain very close to it. APriori shows improved convergence and

closely follows ESDGSEM. finite volume methods tend to smooth the flow, which suppresses the formation of small-scale structures. MCL exhibits an even stronger damping effect on small vortices, which enhances simulation stability.

Figure 3.23: Solenoidal dissipation, ϵ_S along convective time t/τ. Comparison of methods using the Taylor-Green vortex simulation, $M = 1.25$ and $Re = 1600$ with $o = 3$ Eq. 3.9. Top left: 64^3 dof, top right: 128^3 dof, bottom: 256^3 dof.

In line with the solenoidal dissipation results, the dilatational dissipation shown in Fig. 3.24 is difficult to capture accurately. Only ESDGSEM, APosteriori, and APosteriori Subcell methods are able to reproduce it well, although a significant overshoot appears on the intermediate mesh at $t/\tau = 6$. Dilatational dissipation is associated with compressible effects that are par-

ticularly difficult to resolve. The use of positivity-preserving limiters tends to under-resolve these effects, which are important in high Mach number flows. While these limiting techniques effectively capture shocks, as seen in Fig. 3.22, they struggle to accurately represent the compressible features of the flow, despite providing a good resolution of solenoidal dissipation.
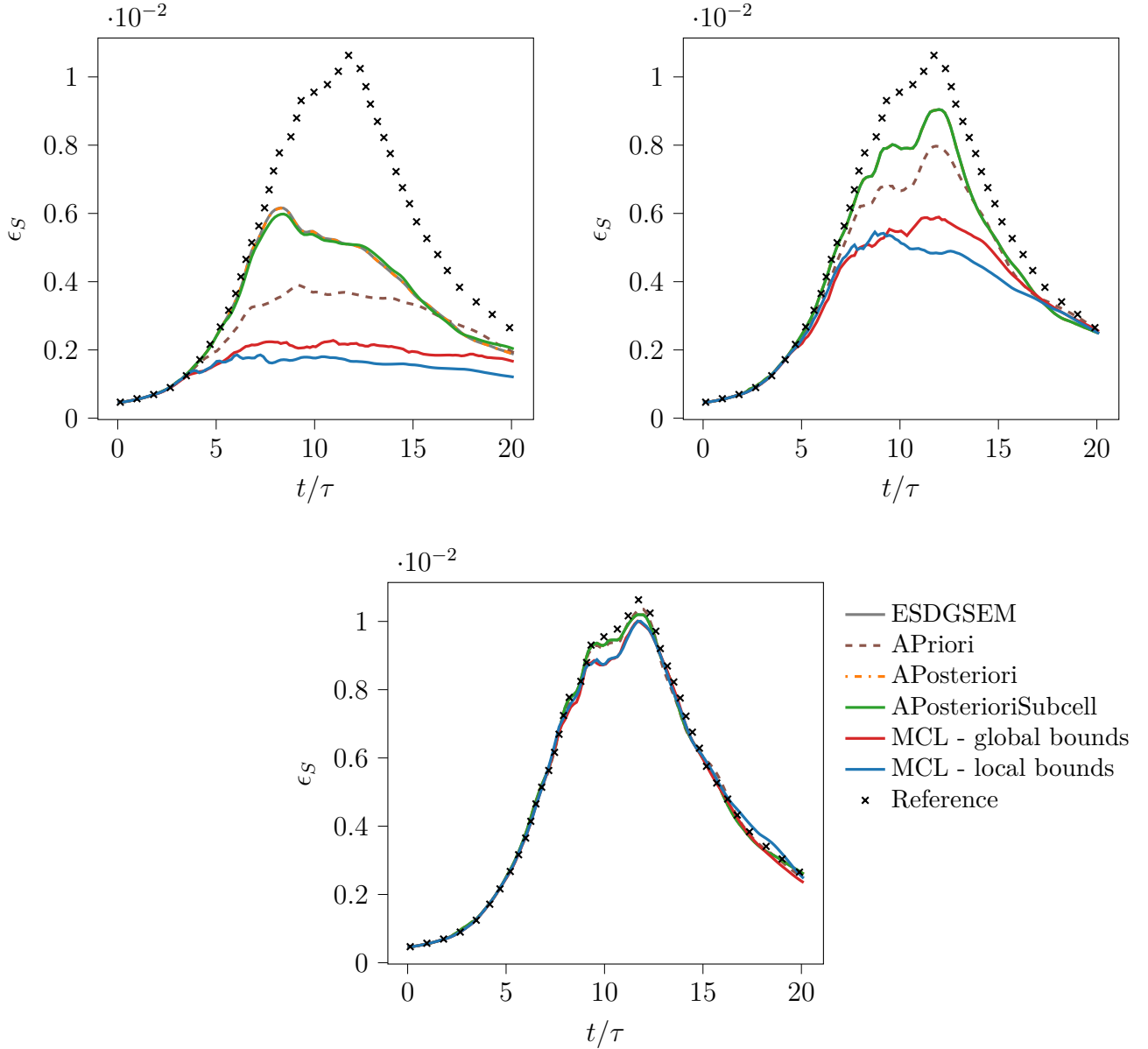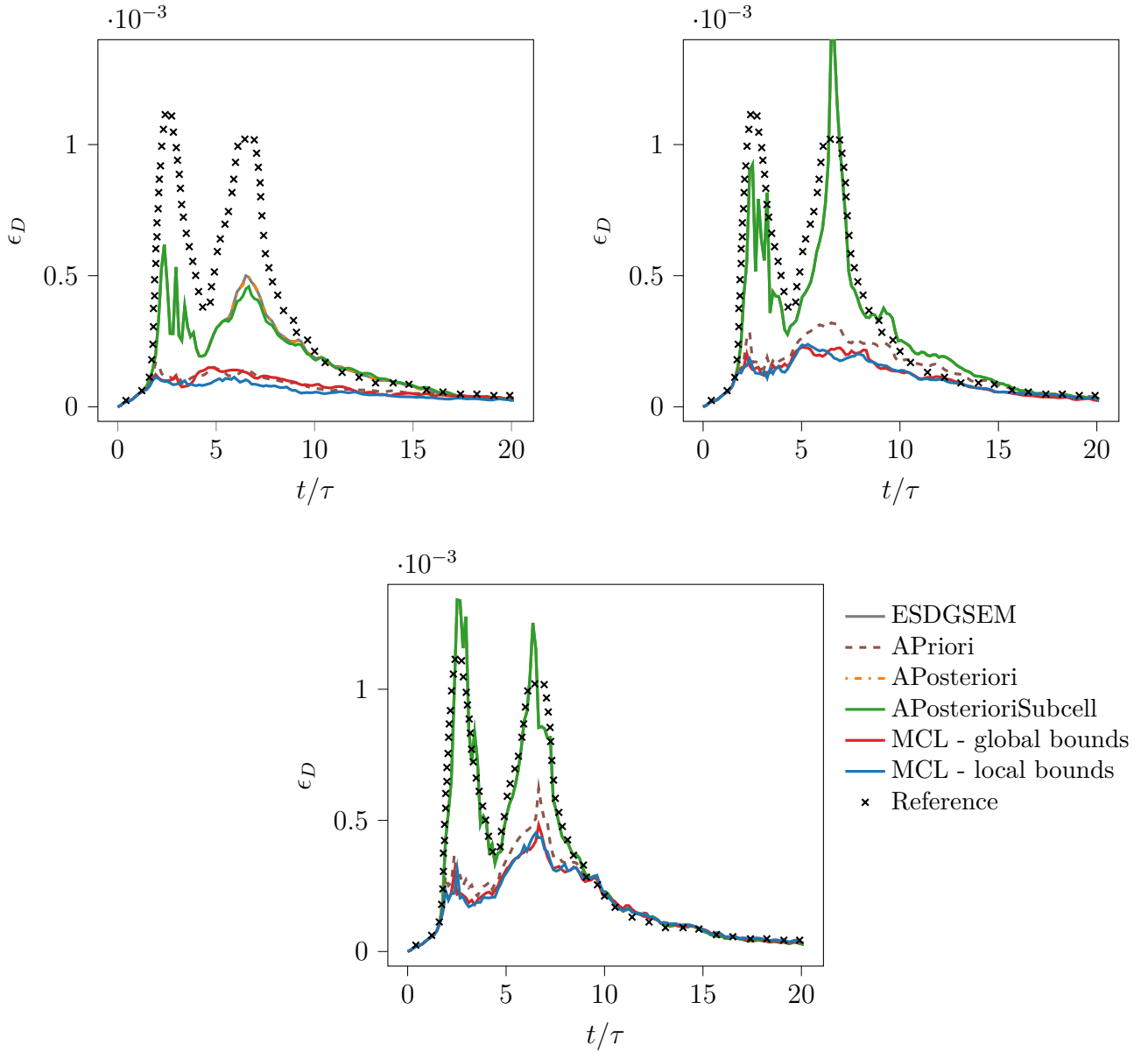

Figure 3.24: Dilatational dissipation, ϵ_D along convective time t/τ. Comparison of methods using the Taylor-Green vortex simulation, $M = 1.25$ and $Re = 1600$ with $o = 3$ Eq. 3.9. Top left: 64^3 dof, top right: 128^3 dof, bottom: 256^3 dof.

3.7.3   BlendingCoefficient

Fig. 3.25 illustrates the temporal evolution of the proportion of troubled cells. As the mesh is refined, there is a significant decrease in the number of troubled cells.
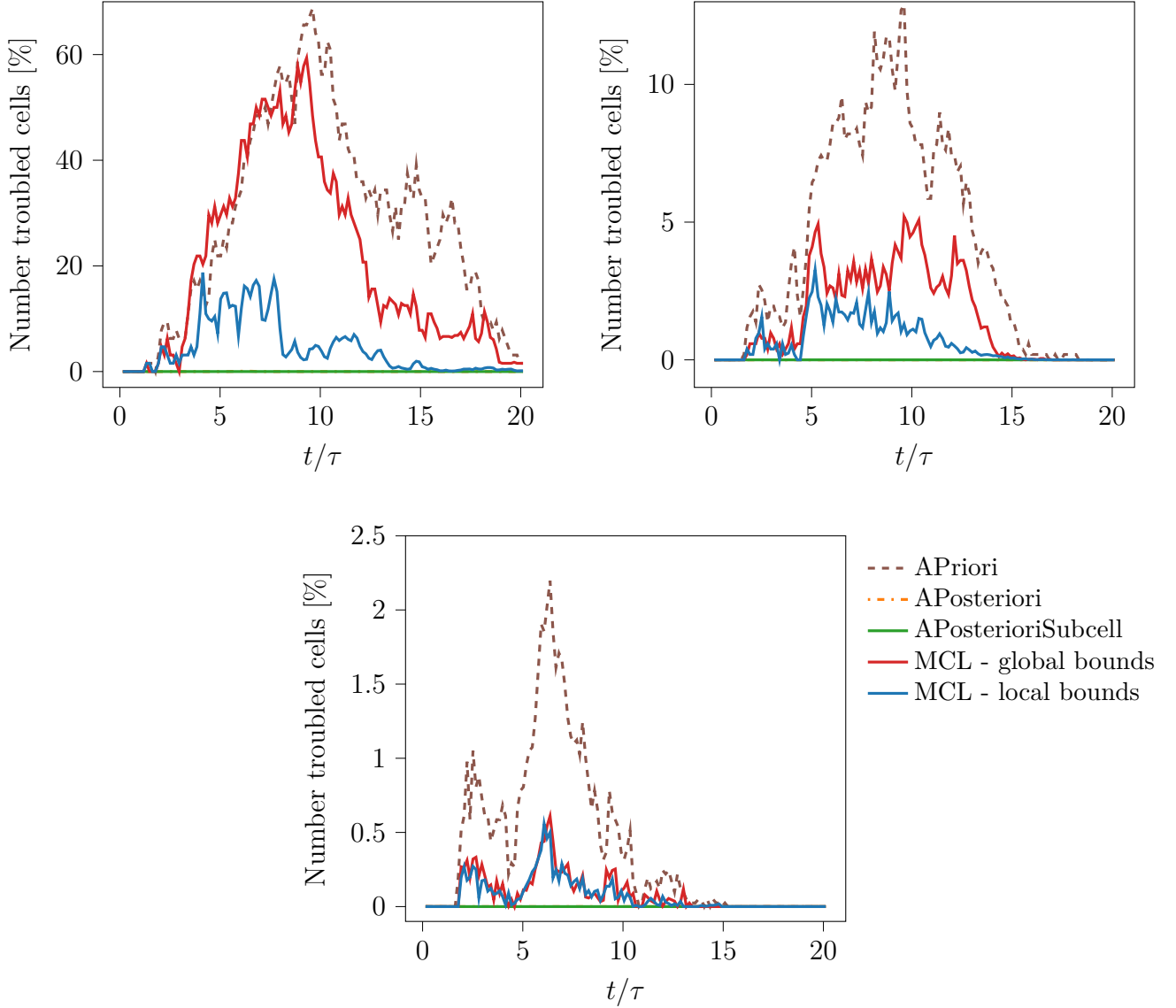
Figure 3.25: Proportion of troubled cells along convective time t/τ. Comparison of methods using the Taylor-Green vortex simulation, $M = 1.25$ and $Re = 1600$ with $o = 3$ Eq. 3.9. Top left: 64^3 dof, top right: 128^3 dof, bottom: 256^3 dof.

The APosteriori and APosteriori Subcell methods consistently show the lowest proportion of troubled cells. Similarly to other test cases, the number of troubled cells for these methods approaches zero, which explains their close agreement with ESDGSEM results. In contrast, the APriori method requires the highest proportion of troubled cells to maintain stability, as it allows for the development of smaller-scale structures and thus requires more frequent limiting.

The MCL method, being more dissipative, suppresses problematic structures and consequently requires fewer troubled cells than APriori. However, even though MCL is applied less frequently, it has a more pronounced effect on flow physics, as illustrated in Fig. 3.23 and Fig. 3.24.

Chapter 4

Conclusion

4.1 Conclusion

This work presented the implementation of a positivity-preserving method that combines the ESDGSEM and first-order finite volume schemes. Simulating compressible flows is challenging, particularly in terms of maintaining stability. The Discontinuous Galerkin method is well suited for capturing turbulence in the solution. Nevertheless, instabilities can still occur, especially near strong discontinuities or in under-resolved regions, emphasising the need for stabilisation techniques. Among the various approaches available, this study focused on positivity-preserving methods, using an FV-DG hybrid scheme.

The Monolithic Convex Limiting method is first described, focussing on the computation of the blending coefficient, which is obtained by multiplying density and pressure limiting factors. This coefficient is determined for each interface of the interpolation points, and the anti-diffusive residuals from each interface are recombined to obtain the contribution at each interpolation point. The density limiter uses two types of bounds: local bounds, which set minimum and maximum values based on immediate neighbours to prevent the creation of new extrema, and global bounds, which enforce a minimum value of zero to maintain stability. Local bounds are particularly effective near discontinuities, where ESDGSEM may produce spurious oscillations, whereas global bounds allow such oscillations as long as the density remains positive.

Other hybrid schemes already implemented in ForDGe, such as APriori, APosteriori, and APosterioriSubcell, are also discussed. The APriori method is an element-wise approach that computes the limiting factor using a regularity criterion, which is also used to identify elements near discontinuities that require stabilisation. The APosteriori method is also element-wise, using a precomputed next time-step solution to determine a limiting factor at each interpolation point and applying the maximum value to the entire element. The APosteriori Subcell method, like MCL, operates on a subcell level and uses a precomputed solution to find blending factors for both density and pressure. Additionally, it computes a coefficient for each interface of the interpolation points, recombining the anti-diffusive residuals to account for the contribution from each interface. Both the APosteriori and APosteriori Subcell methods utilise the Lower Bound criterion to identify elements that require stabilisation. This sensor enables these methods to remain close to the ESDGSEM scheme by flagging only a small number of elements. However, this approach may result in the method being applied too late, potentially leading to

instability in the simulation.

A comparison study has been performed using several test cases to assess the stability and ability to capture complex flows. Comparison of all these methods with the ESDGSEM solution on the Kelvin-Helmholtz instability, the strong vortex shock interaction, the Daru-Tenaud shock tube, and the three-dimensional Taylor Green vortex.

The Kelvin-Helmholtz instability is a classical test case that features the development of small-scale vortical structures due to velocity shear between two fluid layers. This test case is useful for evaluating the effectiveness of numerical schemes in capturing fine-scale features and maintaining stability. Enstrophy is used to quantitatively assess the presence and evolution of these small-scale structures. The results presented show that the ESDGSEM scheme alone is unstable for this problem, failing to develop the smallest vortices. In contrast, all positivity-preserving hybrid methods maintain stability throughout the simulation. Among them, the APosteriori and APosteriori Subcell methods best preserve enstrophy and capture the development of small-scale vortices. The APriori and MCL methods are more dissipative, resulting in a smoother solution and lower enstrophy, but still provide stable results.

The strong vortex-shock interaction test simulates a two-dimensional vortex traversing a stationary shock. By analysing two density profiles against a reference solution, it is observed that the ESDGSEM scheme produces spurious oscillations in the shock region. Both the APosteriori and APosteriori Subcell methods also exhibit similar oscillations, as they remain very close to the ESDGSEM scheme when using the Lower Bound criterion. In contrast, the APriori and MCL methods effectively dampen these oscillations, resulting in smoother gradients. However, APriori and MCL with global bounds still show minor oscillations, while MCL with local bounds completely suppresses them. This damping in the shock region is accompanied by under-resolved vortex regions on coarser meshes, which disappear as the mesh is refined. This test case highlights how the Lower Bound criterion stabilises only the vortex before the shock, where the density falls below the threshold, while allowing the ESDGSEM scheme, which remains stable, to be used elsewhere.

Daru-Tenaud shock tube is a challenging test case involving a viscous shock propagating through a two-dimensional channel with sudden expansion. This configuration leads to intricate interactions among the shock, boundary layers, and reflected waves, making it a rigorous benchmark for numerical schemes. A reference density profile near the wall is used for comparison in all methods. The results indicate that ESDGSEM alone is unstable, highlighting the need for positivity-preserving techniques for this test case. The APosteriori and APosteriori Subcell methods display a similar behaviour, although APosteriori appears unstable on the finest mesh. This instability may be attributed to its close solution to ESDGSEM, whereas APosteriori Subcell remains sufficiently robust to maintain simulation stability. APriori demon-

strates rapid convergence towards the reference solution and captures more flow features than the other approaches. Both MCL variants yield consistent results across all mesh resolutions, ensuring stable simulations for this test case.

The Taylor-Green vortex test evaluates the methods' ability to maintain stability in a complex three-dimensional simulation characterised by strong compressibility effects. A reference solution is used to assess the accuracy in capturing the shock along a Mach line, as well as the solenoidal and dilatational dissipation produced during the simulation. Similarly to previous cases, the ESDGSEM scheme displays spurious oscillations but achieves solenoidal and dilatational dissipation values closest to the reference throughout the simulation. The APosteriori and APosteriori Subcell methods yield results nearly identical to ESDGSEM, retaining these oscillations while preserving the generated dissipation. In contrast, the APriori and MCL methods effectively suppress the oscillations, though this comes at the expense of dissipation. However, APriori, manages to produce solenoidal dissipation values close to ESDGSEM. Despite this, both methods, APriori and MCL, struggle to reproduce the dilatational dissipation, which remains significantly lower than the reference.

Regarding the maximum allowable time step, all methods demonstrate similar behaviour, with comparable time-step sizes across test cases. The element-wise approaches generally permit larger or equivalent time steps compared to the subcell-wise methods, reflecting their less restrictive nature. In contrast, subcell-wise methods like APosteriori Subcell and MCL require smaller time steps due to the increased computational complexity at each interpolation point. In terms of computational cost, the positivity-preserving methods introduce additional overhead compared to the baseline ESDGSEM scheme. The element-wise approaches, such as APriori and APosteriori, are less computationally demanding since they compute a single limiting factor per element, even though APosteriori takes the maximum value among the interpolation points. In contrast, subcell-wise methods like APosteriori Subcell and MCL require the calculation of blending coefficients at each interpolation point in a more complex way than APosteriori within every element, leading to a higher computational expense. Despite the higher computational cost, MCL shows a more dissipative behaviour compared to the other methods. APosteriori and APosteriori Subcell remain very close to the ESDGSEM solution. Although, APosteriori Subcell is more stable than APosteriori as shown with the Daru-Tenaud test case. APriori is the less expensive method and remains stable in any case. Moreover, it shows a rapid convergence to the reference solutions, even though it seems to be quite dissipative, as shown in KHI and TGV test cases.

The selection of an optimal method for simulating compressible flows represents a compromise between computational cost, stability, and accuracy. While methods like APriori and MCL offer increased robustness, and APriori has a lower computational expense, however, they

tend to be more dissipative, smoothing out fine-scale features. Conversely, the APosteriori and APosteriori Subcell methods remain closer to the high-fidelity ESDGSEM solution, better preserving complex flow structures, but at a higher computational cost, especially for APosteriori Subcell, and occasional stability issues. In the end, the choice depends on the specific demands of the problem, balancing the need for stability with the resolution of fine-scale dynamics and available computational resources.

4.2 Future works and perspective

Several avenues for future work can be explored to further enhance the robustness and accuracy of positivity-preserving methods. One promising direction is the extension of the hybrid approach to second-order finite volume schemes, which would improve solution accuracy while maintaining stability near discontinuities. Additionally, employing more advanced quadrature rules, such as the Gauss-Legendre quadrature, could lead to better integration accuracy and improved solution quality, especially for higher-order methods.

Another potential improvement involves the adaptive application of different stabilisation techniques within the same computational domain. By dynamically selecting the most appropriate method based on local flow features, such as using more dissipative schemes near strong shocks and less dissipative ones in smooth regions, the overall stability and accuracy of the simulation could be optimised. A region-based hybridisation strategy would enable a customised approach, applying the strengths of each method in the areas where they are most effective.

Local refinement of the mesh [2, 36, 56] could also greatly improve the accuracy of the solution, allowing the capture of smaller-scale features in specific regions. For instance, octree-based mesh refinement can be employed, where elements are recursively subdivided into smaller elements, such as splitting a two-dimensional element into four child elements, enabling higher resolution in areas with complex flow phenomena or steep gradients. This adaptive mesh refinement (AMR) strategy ensures that computational resources are focused where they are most needed, improving both efficiency and solution quality. Integrating AMR with positivity-preserving methods would require careful handling of data transfer between coarse and fine grids, as well as consistent application of stabilisation techniques across varying mesh resolutions. Such an approach could further enhance the ability to resolve intricate flow structures while maintaining stability and computational efficiency.

Implementing these enhancements would require further research into efficient detection criteria for flow features and the development of robust algorithms to smoothly transition between methods. Such advancements would contribute to the development of more reliable numerical solvers for complex compressible flow simulations.

Bibliography

[1] Anderson, John David. *Modern Compressible Flow.* Fourth edition. McGraw Hill, 2021. ISBN: 978-1-260-47144-1.

[2] M.J. Berger and P. Colella. "Local adaptive mesh refinement for shock hydrodynamics". In: *Journal of Computational Physics* 82.1 (May 1989), pp. 64–84. ISSN: 00219991. DOI: 10.1016/0021-9991(89)90035-1.

[3] Maxime Borbouse et al. "Direct Numerical Simulations of the SPLEEN cascade: a study of the impact of compressibility on transition and separation in a low-pressure turbine passage". In: Hannover, Germany, Mar. 28, 2025. HDL: https://orbi.uliege.be/2268/330117.

[4] Mark H. Carpenter et al. "Entropy Stable Spectral Collocation Schemes for the Navier–Stokes Equations: Discontinuous Interfaces". In: *SIAM Journal on Scientific Computing* 36.5 (Jan. 2014). Publisher: Society for Industrial & Applied Mathematics (SIAM), B835–B867. ISSN: 1064-8275, 1095-7197. DOI: 10.1137/130932193.

[5] Jesse Chan. "On discretely entropy conservative and entropy stable discontinuous Galerkin methods". In: *Journal of Computational Physics* 362 (June 2018). Publisher: Elsevier BV, pp. 346–374. ISSN: 0021-9991. DOI: 10.1016/j.jcp.2018.02.033.

[6] Jesse Chan. "Skew-Symmetric Entropy Stable Modal Discontinuous Galerkin Formulations". In: *Journal of Scientific Computing* 81.1 (Oct. 1, 2019), pp. 459–485. ISSN: 1573-7691. DOI: 10.1007/s10915-019-01026-w.

[7] Jesse Chan et al. "High order entropy stable schemes for the quasi-one-dimensional shallow water and compressible Euler equations". In: *Journal of Computational Physics* 504 (May 2024), p. 112876. ISSN: 00219991. DOI: 10.1016/j.jcp.2024.112876.

[8] Praveen Chandrashekar and Christian Klingenberg. "Entropy Stable Finite Volume Scheme for Ideal Compressible MHD on 2-D Cartesian Meshes". In: *SIAM Journal on Numerical Analysis* 54.2 (Jan. 2016). Publisher: Society for Industrial and Applied Mathematics, pp. 1313–1340. ISSN: 0036-1429. DOI: 10.1137/15M1013626.

[9] Jean-Baptiste Chapelier et al. "Comparison of high-order numerical methodologies for the simulation of the supersonic Taylor–Green vortex flow". In: *Physics of Fluids* 36.5 (May 1, 2024), p. 055146. ISSN: 1070-6631, 1089-7666. DOI: 10.1063/5.0206359.

[10] Eric J. Ching et al. "Shock capturing for discontinuous Galerkin methods with application to predicting heat transfer in hypersonic flows". In: *Journal of Computational Physics* 376 (Jan. 2019), pp. 54–75. ISSN: 00219991. DOI: 10.1016/j.jcp.2018.09.016.

[11] S Scott Collis. "Discontinuous Galerkin methods for turbulence simulation". In: ().

[12] Richard Courant and K. O. Friedrichs. *Supersonic flow and shock waves*. Corr. 5th print. Applied mathematical sciences 21. New York: Springer, 1999. 464 pp. ISBN: 978-0-387-90232-6 978-3-540-90232-4.

[13] Virginie Daru and Christian Tenaud. "Numerical simulation of the viscous shock tube problem by using a high resolution monotonicity-preserving scheme". In: *Computers & Fluids* 38.3 (Mar. 2009), pp. 664–676. ISSN: 00457930. DOI: `10.1016/j.compfluid.2008.06.008`.

[14] Peter Davidson. *Turbulence: An Introduction for Scientists and Engineers*. Oxford University Press, June 2015. ISBN: 978-0-19-872258-8. DOI: `10.1093/acprof:oso/9780198722588.001.0001`.

[15] Gregor J. Gassner. "A Skew-Symmetric Discontinuous Galerkin Spectral Element Discretization and Its Relation to SBP-SAT Finite Difference Methods". In: *SIAM Journal on Scientific Computing* 35.3 (Jan. 2013). Publisher: Society for Industrial & Applied Mathematics (SIAM), A1233–A1253. ISSN: 1064-8275, 1095-7197. DOI: `10.1137/120890144`.

[16] Gregor J. Gassner, Andrew R. Winters, and David A. Kopriva. "Split form nodal discontinuous Galerkin schemes with summation-by-parts property for the compressible Euler equations". In: *Journal of Computational Physics* 327 (Dec. 2016), pp. 39–66. ISSN: 00219991. DOI: `10.1016/j.jcp.2016.09.013`.

[17] Jean-Luc Guermond, Bojan Popov, and Ignacio Tomas. "Invariant domain preserving discretization-independent schemes and convex limiting for hyperbolic systems". In: *Computer Methods in Applied Mechanics and Engineering* 347 (Apr. 2019), pp. 143–175. ISSN: 00457825. DOI: `10.1016/j.cma.2018.11.036`.

[18] Hennes Hajduk. "Monolithic convex limiting in discontinuous Galerkin discretizations of hyperbolic conservation laws". In: *Computers & Mathematics with Applications* 87 (Apr. 2021), pp. 120–138. ISSN: 08981221. DOI: `10.1016/j.camwa.2021.02.012`.

[19] Amiram Harten. "On the symmetric form of systems of conservation laws with entropy". In: *Journal of Computational Physics* 49.1 (Jan. 1983), pp. 151–164. ISSN: 00219991. DOI: `10.1016/0021-9991(83)90118-3`.

[20] Henneaux, David. "A high-order discontinuous Galerkin tool for the simulation of multiphase problems : application to space debris ablation by melting". PhD thesis. UCL - Université Catholique de Louvain, 2024.

[21] Sebastian Hennemann et al. "A provably entropy stable subcell shock capturing approach for high order split form DG for the compressible Euler equations". In: *Journal of Computational Physics* 426 (Feb. 2021), p. 109935. ISSN: 00219991. DOI: `10.1016/j.jcp.2020.109935`.

[22] Koen Hillewaert. "Development of the discontinuous Galerkin method for high-resolution, large scale CFD and acoustics in industrial geometries". PhD thesis. Université Catholique de Louvain, 2013.

[23] Koen Hillewaert, Cecile Goffaux, and Corentin Carton De Wiart. "Development Of A High-order Discontinuous Galerkin Method For The Dns And Les Of Natural Convection Flows In Buildings." In: 2017 Building Simulation Conference. Vol. 13. IBPSA, Aug. 28, 2013. ISBN: 978-2-7466-6294-0. DOI: `https://doi.org/10.26868/25222708.2013.1501`.

[24] Florian Hindenlang et al. "Explicit discontinuous Galerkin methods for unsteady problems". In: *Computers & Fluids* 61 (May 2012). Publisher: Elsevier BV, pp. 86–93. ISSN: 0045-7930. DOI: `10.1016/j.compfluid.2012.03.006`.

[25] T. J. R. Hughes, L. P. Franca, and M. Mallet. "A new finite element formulation for computational fluid dynamics: I. Symmetric forms of the compressible Euler and Navier-Stokes equations and the second law of thermodynamics". In: *Computer Methods in Applied Mechanics and Engineering* 54.2 (Feb. 1, 1986), pp. 223–234. ISSN: 0045-7825. DOI: `10.1016/0045-7825(86)90127-1`.

[26] Zhen-Hua Jiang et al. "Hybrid Discontinuous Galerkin/Finite Volume Method with Subcell Resolution for Shocked Flows". In: *AIAA Journal* 59.6 (June 2021), pp. 2027–2044. ISSN: 0001-1452, 1533-385X. DOI: `10.2514/1.J059763`.

[27] George Karniadakis et al. *Spectral/hp Element Methods for Computational Fluid Dynamics: Second Edition*. Second Edition, Second Edition. Numerical Mathematics and Scientific Computation. Oxford, New York: Oxford University Press, June 2, 2005. 676 pp. ISBN: 978-0-19-852869-2.

[28] Chongam Kim. "CI2 – Inviscid Strong Vortex-Shock Wave Interaction". In: (). URL: `https://how5.cenaero.be/content/ci2-%E2%80%93-inviscid-strong-vortex-shock-wave-interaction`.

[29] David A. Kopriva. "Spectral Element Methods". In: *Implementing Spectral Methods for Partial Differential Equations: Algorithms for Scientists and Engineers*. Ed. by David A. Kopriva. Dordrecht: Springer Netherlands, 2009, pp. 293–354. ISBN: 978-90-481-2261-5. DOI: `10.1007/978-90-481-2261-5_8`.

[30] David A. Kopriva and Gregor Gassner. "On the Quadrature and Weak Form Choices in Collocation Type Discontinuous Galerkin Spectral Element Methods". In: *Journal of Scientific Computing* 44.2 (Aug. 2010). Publisher: Springer Science and Business Media LLC, pp. 136–155. ISSN: 0885-7474, 1573-7691. DOI: `10.1007/s10915-010-9372-3`.

[31] Dmitri Kuzmin. "Monolithic convex limiting for continuous finite element discretizations of hyperbolic conservation laws". In: *Computer Methods in Applied Mechanics and Engineering* 361 (Apr. 2020), p. 112804. ISSN: 00457825. DOI: `10.1016/j.cma.2019.112804`.

[32] Yimin Lin, Jesse Chan, and Ignacio Tomas. "A positivity preserving strategy for entropy stable discontinuous Galerkin discretizations of the compressible Euler and Navier-Stokes equations". In: *Journal of Computational Physics* 475 (Feb. 2023), p. 111850. ISSN: 00219991. DOI: `10.1016/j.jcp.2022.111850`.

[33] Gustavo Lopes et al. "An Open Test Case for High-Speed Low-Pressure Turbines: The SPLEEN C1 Cascade". In: *International Journal of Turbomachinery, Propulsion and Power* 10.1 (Feb. 3, 2025), p. 2. ISSN: 2504-186X. DOI: `10.3390/ijtpp10010002`.

[34] Johannes Markert, Gregor Gassner, and Stefanie Walch. "A Sub-element Adaptive Shock Capturing Approach for Discontinuous Galerkin Methods". In: *Communications on Applied Mathematics and Computation* 5.2 (June 1, 2023), pp. 679–721. ISSN: 2661-8893. DOI: `10.1007/s42967-021-00120-x`.

[35] *Minimizing the impact of shock capturing method for scale resolved simulation of transonic turbulent flows.* URL: `https://www.designofturbomachines.uliege.be/cms/c_6339224/en/minimizing-the-impact-of-shock-capturing-method-for-scale-resolved-simulation-of-transonic-turbulent-flows` (visited on 05/23/2025).

[36] Pascal Mossier, Andrea Beck, and Claus-Dieter Munz. "A p-Adaptive Discontinuous Galerkin Method with hp-Shock Capturing". In: *Journal of Scientific Computing* 91.1 (Feb. 18, 2022), p. 4. ISSN: 1573-7691. DOI: `10.1007/s10915-022-01770-6`.

[37] Will Pazner. "Sparse invariant domain preserving discontinuous Galerkin methods with subcell convex limiting". In: *Computer Methods in Applied Mechanics and Engineering* 382 (Aug. 2021), p. 113876. ISSN: 00457825. DOI: `10.1016/j.cma.2021.113876`.

[38] Per-Olof Persson and Jaime Peraire. "Sub-Cell Shock Capturing for Discontinuous Galerkin Methods". In: *44th AIAA Aerospace Sciences Meeting and Exhibit.* 44th AIAA Aerospace Sciences Meeting and Exhibit. Reno, Nevada: American Institute of Aeronautics and Astronautics, Jan. 9, 2006. ISBN: 978-1-62410-039-0. DOI: `10.2514/6.2006-112`.

[39] Stephen B. Pope. *Turbulent flows.* 1. publ., 12. print. Cambridge: Cambridge Univ. Press, 2015. 771 pp. ISBN: 978-0-521-59886-6 978-0-521-59125-6.

[40]   James J. Quirk and S. Karni. "On the dynamics of a shock–bubble interaction". In: *Journal of Fluid Mechanics* 318 (July 10, 1996), pp. 129–163. ISSN: 0022-1120, 1469-7645. DOI: 10.1017/S0022112096007069.

[41]   Hendrik Ranocha et al. "Efficient Implementation of Modern Entropy Stable and Kinetic Energy Preserving Discontinuous Galerkin Methods for Conservation Laws". In: *ACM Transactions on Mathematical Software* 49.4 (Dec. 31, 2023). Publisher: Association for Computing Machinery (ACM), pp. 1–30. ISSN: 0098-3500, 1557-7295. DOI: 10.1145/3625559.

[42]   A. Rueda-Ramírez and G. Gassner. "A Subcell Finite Volume Positivity-Preserving Limiter for DGSEM Discretizations of the Euler Equations". In: *14th WCCM-ECCOMAS Congress*. 14th WCCM-ECCOMAS Congress. CIMNE, 2021. DOI: 10.48550/arXiv.2102.06017.

[43]   Andrés M. Rueda-Ramírez, Will Pazner, and Gregor J. Gassner. "Subcell limiting strategies for discontinuous Galerkin spectral element methods". In: *Computers & Fluids* 247 (Oct. 2022), p. 105627. ISSN: 00457930. DOI: 10.1016/j.compfluid.2022.105627.

[44]   Andrés M. Rueda-Ramírez et al. "Monolithic Convex Limiting for Legendre-Gauss-Lobatto Discontinuous Galerkin Spectral-Element Methods". In: *Communications on Applied Mathematics and Computation* 6.3 (Sept. 2024), pp. 1860–1898. ISSN: 2096-6385, 2661-8893. DOI: 10.1007/s42967-023-00321-6.

[45]   Steven J. Ruuth and Raymond J. Spiteri. "High-Order Strong-Stability-Preserving Runge-Kutta Methods with Downwind-Biased Spatial Discretizations". In: *SIAM Journal on Numerical Analysis* 42.3 (2005). Publisher: Society for Industrial and Applied Mathematics, pp. 974–996. ISSN: 00361429.

[46]   S. Sarkar et al. "The analysis and modelling of dilatational terms in compressible turbulence". In: *Journal of Fluid Mechanics* 227 (June 1991), pp. 473–493. ISSN: 1469-7645, 0022-1120. DOI: 10.1017/S0022112091000204.

[47]   Pierre Schrooyen et al. "Fully implicit Discontinuous Galerkin solver to study surface and volume ablation competition in atmospheric entry flows". In: *International Journal of Heat and Mass Transfer* 103 (Dec. 2016), pp. 108–124. ISSN: 00179310. DOI: 10.1016/j.ijheatmasstransfer.2016.07.022.

[48]   Schrooyen, Pierre et al. *Towards high-order discretization method for hypersonic flow*. 2022.

[49]   Loïc Sombaert et al. *Commissioning and characterization of semi-elliptical and conical supersonic nozzles in the VKI-Plasmatron*. June 20, 2022.

[50]   Raymond J. Spiteri and Steven J. Ruuth. "A New Class of Optimal High-Order Strong-Stability-Preserving Time Discretization Methods". In: *SIAM Journal on Numerical Analysis* 40.2 (2003). Publisher: Society for Industrial and Applied Mathematics, pp. 469–491. ISSN: 0036-1429.

[51]   William Sutherland. "LII. *The viscosity of gases and molecular force*". In: *The London, Edinburgh, and Dublin Philosophical Magazine and Journal of Science* 36.223 (Dec. 1893), pp. 507–531. ISSN: 1941-5982, 1941-5990. DOI: 10.1080/14786449308620508.

[52]   Eitan Tadmor. "Entropy stability theory for difference approximations of nonlinear conservation laws and related time-dependent problems". In: *Acta Numerica* 12 (May 2003), pp. 451–512. ISSN: 0962-4929, 1474-0508. DOI: 10.1017/S0962492902000156.

[53]   Patrick Tene Hedje et al. "Large Eddy Simulations of a High-Speed Low-Pressure Turbine Cascade at Subsonic and Transonic Mach Numbers". In: *Journal of Turbomachinery* 147.101010 (Apr. 8, 2025). ISSN: 0889-504X. DOI: 10.1115/1.4068124.

[54]   Zhenming Wang et al. "Assessment of high-order interpolation-based weighted essentially non-oscillatory schemes for compressible Taylor–Green vortex flows". In: *Physics of Fluids* 36.11 (Nov. 1, 2024), p. 116119. ISSN: 1070-6631, 1089-7666. DOI: 10.1063/5.0236997.

[55]   Xuesong Wu. "Nonlinear Theories for Shear Flow Instabilities: Physical Insights and Practical Implications". In: *Annual Review of Fluid Mechanics* 51 (Volume 51, 2019 Jan. 5, 2019). Publisher: Annual Reviews, pp. 451–485. ISSN: 0066-4189, 1545-4479. DOI: 10.1146/annurev-fluid-122316-045252.

[56]   Cheng-Hau Yang et al. "Octree-based adaptive mesh refinement and the shifted boundary method for efficient fluid dynamics simulations". In: *Advances in Computational Science and Engineering* 4.0 (2025), pp. 57–84. ISSN: 2837-1739. DOI: 10.3934/acse.2025012.

[57]   Steven T Zalesak. "Fully multidimensional flux-corrected transport algorithms for fluids". In: *Journal of Computational Physics* 31.3 (June 1979), pp. 335–362. ISSN: 00219991. DOI: 10.1016/0021-9991(79)90051-2.